Elucidation of Electrocatalytic Oxidation Reactions on Abundant Materials -Combination of Theory and Experiment-

André Philipp Wark

Faculty of Industrial Engineering, Mechanical Engineering and Computer Science
University of Iceland
2024

Elucidation of Electrocatalytic Oxidation Reactions on Abundant Materials -Combination of Theory and Experiment-

André Philipp Wark

Dissertation submitted in partial fulfilment of a
Philosophiae Doctor degree in Chemical Engineering

Advisor
Prof. Egill Skúlason

PhD Committee
Prof. Egill Skúlason
Prof. Hannes Jónsson
Prof. Andrew James Medford
Dr. Jun Maruyama

Opponents
Prof. Núria López
Prof. Jakob Kibsgaard

Faculty of Industrial Engineering, Mechanical Engineering
and Computer Sciences
University of Iceland
Reykjavik, June 2024

Dissertation submitted in partial fulfilment of a *Philosophiae Doctor* degree in Chemical Engineering.

Faculty of Industrial Engineering, Mechanical Engineering
and Computer Sciences
School of Engineering and Natural Sciences
University of Iceland
Tæknigarði, Dunhaga 5
107, Reykjavik
Iceland

Bibliographic information:
André Philipp Wark, 2024, *Elucidation of Electrocatalytic Oxidation Reactions on Abundant Materials -Combination of Theory and Experiment-*, PhD dissertation, Faculty of Industrial Engineering, Mechanical Engineering and Computer Sciences,
University of Iceland, XX pp.

Author ORCID: 0009-0004-6326-1563

Printing: XX
Reykjavik, Iceland, June 2024

Abstract

The global climate crisis poses one of the most pressing challenges of our time, affecting diverse sectors and demanding urgent attention from scientists, policymakers, and stakeholders. Addressing the multifaceted environmental, political, societal, and technical challenges accompanying this crisis has become paramount. Beyond merely capturing emitted carbon dioxide (CO_2) and other greenhouse gases to mitigate temperature rise, proactive measures are imperative. Central to this effort is the transition from fossil-based to sustainable energy systems. However, achieving this transition necessitates the advancement of novel energy storage devices, such as fuel cells and batteries, through fundamental research to enhance their efficiency.

The Oxygen Evolution Reaction (OER) stands as a critical prototype chemical reaction in this context, requiring low thermochemical and kinetic barriers for high efficiency in energy devices. Moreover, comprehensive understanding of the OER becomes essential when it competes with other desirable oxidation reactions.

One facet of this study delves into a computational exploration of the competition between the electrochemical OER and the Nitrogen Oxidation Reaction (NOR) on a rutile-typed TiO_2(110) electrode. Employing Grand-Canonical Density Functional Theory (GC-DFT) calculations, we investigate the occurrence of these reactions on the abundant electrode material under various conditions. Our findings reveal a close competition between these reactions, with the OER both promoting and suppressing the NOR. Furthermore, we propose potential pulsing and oxygen saturation of the electrode as strategies to enhance the nitrate yield. The outcomes of this investigation were published in the Journal of Physical Chemistry Letters in 2022.

The subsequent sections of this dissertation concentrate on exploring the OER on Earth-abundant materials. We examine the OER on Highly-Oriented Pyrolytic Graphite (HOPG), both with and without deposited manganese-oxide nanosheets (MnO_2NS). Employing diverse spectroscopic and electrochemical techniques, including noise electrochemical scanning tunnelling microscopy (n-EC-STM) and DFT calculations, we elucidate the enhanced OER activity of the hybrid material. Our microscopic measurements pinpoint the interface between the HOPG substrate and MnO_2NS as the source of increased OER performance. DFT calculations further corroborate this, attributing the enhancement to terminal oxygen moieties bound to manganese. The results were published in Advanced Energy Materials in 2023.

Expanding on these findings, we investigate hybrid materials composed of carbonized iron phthalocyanines on HOPG (CFePc/HOPG), with and without deposited MnO_2NS (MnO_2NS/CFePc/HOPG). Through synthesis, characterization, and electrochemical measurements, we unveil the enhanced OER activity of CFePc/HOPG compared to MnO_2NS on HOPG. Our n-EC-STM observations elucidate that the OER predominantly occurs at the iron centers, in alignment with our DFT calculations. Additionally, we

explore tricomponent materials MnO_2NS/CFePc/HOPG, revealing further improvements in OER performance. This finding, supported by our DFT calculations, underscores the absence of a thermodynamic barrier at this location. The results of this study were submitted in April 2024.

Útdráttur

Að koma böndum á hnattræna hlýnun er meðal brýnustu verkefna samtímans. Bregðast þarf við þeim umhverfislegu, pólitísku, samfélagslegu og tæknilegu áskorunum sem við stöndum frammi fyrir. Til að draga úr hækkun hitastigs dugar föngun koltvíoxíðs (CO_2) og annarra gróðurhúsalofttegunda ekki ein og sér, einnig er þörf á fyrirbyggjandi aðgerðum, svosem útfösun jarðefnaeldsneytis. Orkuskiptin nást þó aðeins með hjálp grunnrannsókna sem leitt geta til frekari þróunar rafhlaðna, efnarafala og annarrar tækni sem notuð er við geymslu orku.

Í þessu samhengi er súrefnismyndunarhvarfið (OER) sérlega mikilvægt, en leita þarf leiða til að lækka þá hreyfifræðilegu virkjunarhóla sem standa í vegi fyrir hárri nýtni þess. Auk þess er nákvæmur skilningur á OER nauðsynlegur þegar samkeppni þess við önnur oxunarhvörf er könnuð.

Í fyrsta hluta þessarar ritgerðar kynnum við niðurstöður rannóknar þar sem notast var við tölvureikninga á samkeppni OER og rafefnafræðilegrar oxunar niturs (NOR) á rutile TiO_2 (110) rafskauti. Með notkun þéttnifellafræðireikninga með breytilegum fjölda rafeinda (GC-DFT) könnum við fýsileika hvarfanna á þessu algenga efni við mismunandi hvarfaðstæður. Niðurstöður okkar sýna fram á jafna samkeppni hvarfanna tveggja, og virðist OER hvort sem er geta hindrað eða stuðlað að NOR, eftir því hverjar hvarfaðstæður eru. Að auki leggjum við til púlsun spennu og mettun rafskautsins með súrefni sem mögulegar leiðir til að auka framleiðslu nítrats. Rannsóknin var birt í Journal of Physical Chemstry Letters árið 2022.

Síðari hlutar ritgerðarinnar fjallar um rannsóknir á OER á efnum sem gnægð er af í náttúrunni. Við könnum OER á há-átttuðu hitahreinsuðu grafíti (HOPG), með og án útfelldra nanólaga mangan-oxíðs (MnO_2NS). Með notkun fjölbreyttra greiningar- og rafefnafræðilegra aðferða, s.s. rafefnafræðilegrar smugsjár (n-EC-STM) og DFT reikninga, vörpum við ljósi á aukna OER virkni blendingsefnisins. Samkvæmt mælingum okkar á þessi aukna virkni OER upptök sín á mótum HOPG undirlagsins og MnO_2NS. Þetta er í samræmi við niðurstöður DFT reikninga, sem eigna súrefnisatómum bundum mangani þessa auknu virkni. Niðurstöður rannsóknarinnar voru birtar í Advanced Energy Materials árið 2023.

Í framhaldi af þessu rannsökuðum við svipað blendingsefni sem samanstendur af kolsýrðu járnþalósýaníni á HOPG (CFePc/HOPG), án og með MnO_2NS setlags (MnO_2/ CFePc/HOPG). Með myndun, auðkenningu og rafefnafræðilegum mælingum sýnum við fram á aukna OER virkni CFePc/HOPG samanborið við MnO_2NS á HOPG. Samkvæmt n-EC-STM tilraunum okkar á OER sér að mestu stað á hvarfstöðum með járnbindingu, í góðu samræmi við niðurstöður DFT reikninga. Að auki könnum við OER virkni þríþátta efnisins MnO_2NS/CFePc/HOPG og finnum aukna virkni samanborið við önnur efni sem skoðuð voru. Niðurstöður rannsóknarinnar voru sendar inn til birtingar í apríl 2024.

For Elias.

Acknowledgements

I am sitting here now, about to finish one of my most important journeys in my academic career and of my life. If one had asked me several years ago whether I would end up pursuing my PhD in Iceland, I would have called this person crazy. However, life has other plans with you sometimes- and here I am. I am grateful for my supervisor, Prof. Egill Skúlason, who entrusted me with these projects and helped me to mature to the scientist and person I am now. We truly went through an eventful journey in which we learned much, and which is coming to an end. You are very knowledgeable scientist full of ideas who also gives his students time and space to develop in many regards. Apart from your academic guidance, you provided me with the opportunity to present our research to the community and to build up my network. Moreover, I would like to express my gratitude to my doctoral committee, Prof. Hannes Jónsson from the University of Iceland, Dr. Andrew J Medford from the Georgia Institute of Technology and Dr. Jun Maruyama from the Osaka Research Institute of Industrial Science and Technology. Hannes‘ way of approaching scientific problems is still fascinating to me since he finds questions and solutions which are actually obvious, but I do not think of. The same applies to AJ, who also knows well how to think outside the box. I feel delighted to have worked under your guidance.

Additionally, I am deeply grateful for my collaborators, Dr Jun Maruyama and Prof Aliaksandr Bandarenka, Thorsten O. Schmidt, Dr Regina M. Kluge and Dr Richard W. Haid from the Technical University of Munich. Their trust, faith and patience are appreciated, and I have learnt many interesting aspects about experimental electrochemistry from them. Jun’s deep insights and understanding in electrocatalysis and material science greatly impress me. Similarly, I have really benefitted from Alex’ inexhaustible expertise in the field of electrochemistry. Jun and Alex, I will be very happy to collaborate with you again! I really enjoyed the time with you. Furthermore, it has been fun to write and to work on the manuscripts with you, Thorsten. I am very sure that we would have never achieved what we did without your ideas and your creative sense of perfection for figures.

My heartfelt thanks also go to my opponents, Prof. Núria López and Prof. Jakob Kibsgaard, for examining my thesis. Besides being an outstanding scientist, Núria is a woman with her heart in the right place. It is definitely not something to be taken for granted to buy a birthday cake for a stranger's doctoral student. You made this evening in Leiden very special. I am also looking forward to seeing Jakob at DTU again and to introducing him to Ivano.

I can hardly find appropriate words for the most important person in my life, Elias, my beloved boyfriend, fiancé, best friend, and partner in crime in all these years. You have

truly taught what it means to be loved unconditionally and with endless loyalty. I am endlessly grateful that you have been on my side and have stood by me, although your partner was 2000 km away. Your biggest present was to allow me to pursue my dreams here, having unwavering trust and confidence in us. You have enriched my life with joy, happiness and tons of memes every single day we have been together. I have not always been easy to handle, but you have stayed for which I cannot find words to express my gratitude. Finally, we will start our life together in Copenhagen. Thank you for being a crucial part of this journey.

To Yorick, I am indebted with gratitude for you, being a rock in the surf during our time here. I will miss our gym sessions, our cooking sessions and our movie nights, in which you disassemble the logic of the movies, and your open ears. You are a friend on which you can count, and you made a difference for me. Your infinite and unconditioned support is highly appreciated. I would also like to thank my friend Nicolas Girolami who is an inexhaustive source of jokes and intelligent puns which have brightened up my day. To my other friends, Nasira, Annemarie, Marvin, Jonas, Dominic, Liam, Jasmin, Daniel, Christoph, Juan, Paula, Perry, Daniel, Vivian, Christian, Killian, and Jasmin and many others I might have forgotten to mention: This journey would not have been as enjoyable as without you. I would also like to express my gratitude to my family, my mom Gertraud, my brother Torben and his family, my aunt Rita and my cousin Caren and her family who has always supported me, even if it was difficult. You mean the world to me! I barely believe I would have achieved anything without your support. I would also like to thank the “TheoChem Group” (past and present members) for their friendship, unforgettable trips, journeys and nights and endless moral support. It does not happen often that you also call your colleagues friends. A similar statement can be made for many “kitchen mates” of the past and present, particularly Zaw (I will miss finding cakes and cookies in my fridge), Ville, Nina, Yerko, Brenda, Iris, Rébecca, Kushmin, Joni, Shisha and many more.

As I realize I should come to an end, my final words go to Prof Lucio Colombi Ciacchi, Dr Massimo Delle Piane and the HMI Group at the University of Bremen, who helped me finding back my love and commitment for science after a difficult time I had gone through. I think I would not have continued my academic journey with your support.

Thank you all once again!

André

Preface

This thesis is submitted in candidacy for a Ph.D. degree from the University of Iceland. The work has been conducted between October 2019 and June 2024 at Faculty of Industrial Engineering, Mechanical Engineering and Computer Sciences, supervised by Prof. Egill Skúlason.

The Icelandic Research Fund (Grant no. 196437-051) and the Doctoral Fund of the University of Iceland financially supported the work.

André Philipp Wark

June 2024

Table of Contents

List of Figures

List of Tables

List of Articles and Candidate's Contribution

Article I:

Ebrahim Tayyebi, Árni Björn Höskuldsson*, André Wark*, Narges Atrak, Benjamin M. Comer, Andrew James Medford, Egill Skúlason

"Perspectives on the Competition between the Electrochemical Water and N_2 Oxidation on a TiO_2(110) Electrode"

The Journal of Physical Chemistry Letters 13 no. 26 (2022): 6123-6129.

* Contributed equally

The PhD candidate performed and analyzed some of the DFT calculations, validated the methodology and co-conceptualized and co-wrote the manuscript. The candidate conceptualized and designed Figure 1 in this paper.

Article II:

Thorsten O. Schmidt*, André Wark*, Richard W. Haid, Regina M. Kluge, Shinya Suzuki, Kazuhide Kamiya, Aliaksandr S. Bandarenka, Jun Maruyama, Egill Skúlason

"Elucidating the Active Sites and Synergies in Water Splitting on Manganese Oxide Nanosheets on Graphite Support"

Advanced Energy Materials 13 no. 43 (2023): 2302039.

* Contributed equally

The PhD candidate conceptualized, tested, performed, and analysed all the DFT calculations in this work and conceptualized and co-wrote the first draft of the manuscript with TOS. Figure 3 was conceptualized and designed by the candidate as well as all figures related to the DFT calculations in the supporting information.

Article III:

André Wark*, Thorsten O. Schmidt*, Richard W. Haid, Regina M. Kluge, Shinya Suzuki, Zyun Siroma, Egill Skúlason, Aliaksandr S. Bandarenka, Jun Maruyama

"The Role of Manganese Oxide Nanosheets in Pyrolyzed Carbonaceous Supports for Water Oxidation"

submitted (April 2024)

* Contributed equally

The PhD candidate conceptualized, tested, performed, and analysed all the DFT calculations in this work and conceptualized and co-wrote the first draft of the manuscript with TOS. Figure 3 was conceptualized and designed by the candidate as well as all figures related to the DFT calculations in the supporting information.

Abbreviations

BEEF	Bayesian error estimation functional
CFePc	Carbonized iron phthalocyanine
CHE	Computational Hydrogen Electrode
CV	Cyclovoltammetry
DFT	Density functional theory
FFT	Fast Fourier Transform
GGA	Generalized Gradient Approximation
HER	Hydrogen Evolution Reaction
HF	Hartree Fock
HOPG	Highly-Oriented Pyrolytic Graphite
HSE	Heyd-Scuseria-Ernzernhof
KS	Kohn-Sham
LDA	Local Density Approximation
LSV	Linear Sweep Voltammetry
MBD	Many-Body Dispersion
MnO_2NS	Manganese Oxide Nanosheets
n-EC-STM	Noise ElectroChemical Scanning Tunnelling Microscopy
NOR	Nitrogen Oxidation Reaction
OER	Oxygen Evolution Reaction
PAW	Projector Augmented Wave
PBE	Perdew-Burke-Ernzerhof
PDS	Potential Determining Step
rVV	Revised Vydrov and van Voorhis

SCAN	Strongly Constrained and Appropriately Normed
U	Applied Potential
U_{Hub}	Hubbard Correction Parameter
vdW	Van der Waals

1 Introduction

1.1 The Climate Crisis

The pressing challenges of the climate crisis require novel strategies to reduce the production and accumulation of greenhouse gases such as carbon dioxide (CO_2) and methane (CH_4) in the atmosphere. Since the excessive amount of greenhouse gases has had dramatic impact on the climate and the environment, being evident in an increasing number of extraordinary instances such as draughts, floods and storms, the urgency of taking decisive actions has heightened.[1,2]

As Figure 1 shows, the trends with regard to average temperatures anomalies in the past 60 years have changed to higher values (red bars in Figure 1) than in the years before this period of time. Particularly, the past ten years have been the warmest in these recordings.[3–5]

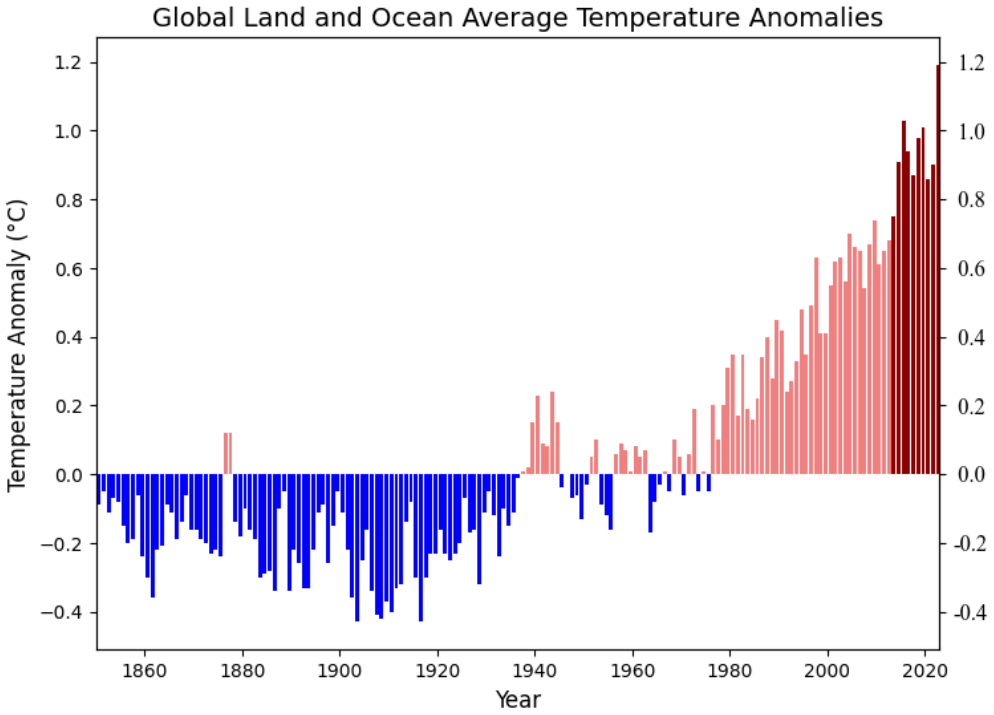

Figure 1: Anomalies of the global land and ocean temperatures between 1860 and 2023. Blue bars represent negative deviations, while red bars show deviations towards higher temperatures than the average. Note that the last ten years are highlighted by dark red. (Adopted from [5])

The connection between the extraordinary increase of the average global temperature and the emission of greenhouse gases has been proven in various studies and is explained by the greenhouse effect as demonstrated in Figure 2.[1,6]

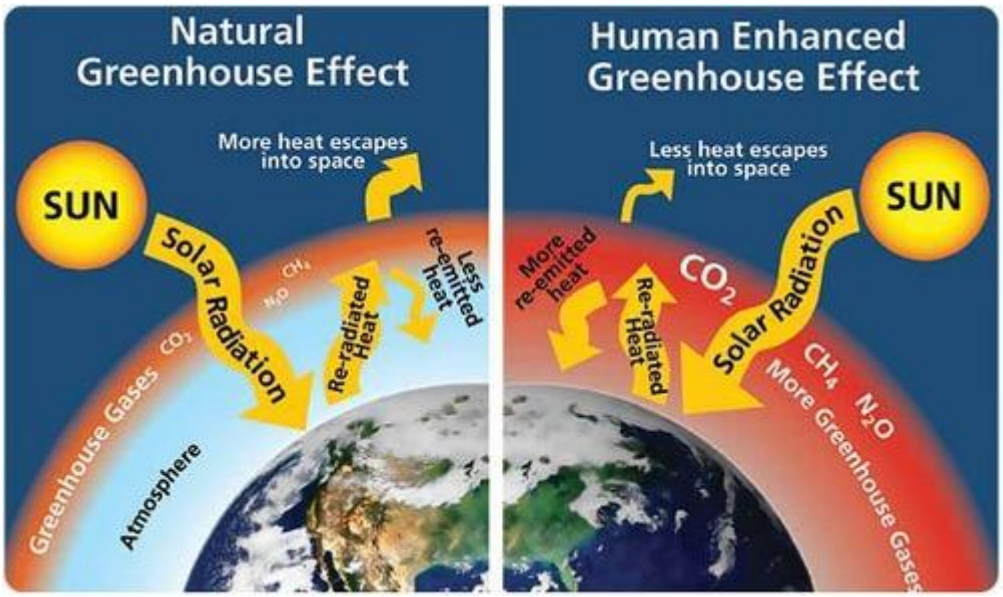

Figure 2: Explanation of the Greenhouse Effect. The left side shows the natural Greenhouse Effect and is contrasted by anthropogenic Greenhouse effect on the right side. (Taken from [7])

Solar radiation reaches earth and is re-radiated to space, while some of this radiation remains in earth's atmosphere since it gets re-emitted by greenhouse gases.[1,2] The latter effect is increasing as the concentration of greenhouse gases is increasing. Consequently, the global temperature has risen and the number of disastrous events has also raised.[1,8] As a result, the life on earth as we used to know is endangered.

One consequence of the climate crisis is the rise of the global sea levels with immediate impact for the environment, wildlife and humans living at coastal lines. One third of the EU's population lives within the endangered costal area with a distance of 50 km to the sea, generating 30% of EU's GDP and locating assets with values between 500 and 1,000 billion Euro.[9] In worst-case scenarios, assuming the population in low-elevations zones, about 1.4 billion people are in danger to become climate refugees by 2060.[10–13] Because of the displacement of this tremendous number of people, countries which are located in less endangered zones will face economic and societal challenges to integrate these refugees. Beside future challenges and economic losses, the costs to compensate damages caused by natural disasters have already grown.[8] The German reinsurer Munich Re reported economic losses for companies of 95 billion Dollar at total costs of 250 billion Dollar as a consequence of natural disasters in 2023 which is above the average of ten years.[14] The National Oceanic and Atmospheric Administration (NOAA) evaluated the number of disastrous events such as floods and droughts in the US in the past 44 years and the costs they generated. The chart in Figure 3 summarizes the number of these disastrous events and their costs. It is evident here that not only the number of disastrous events is continuously growing, but also the costs to cover them.[8]

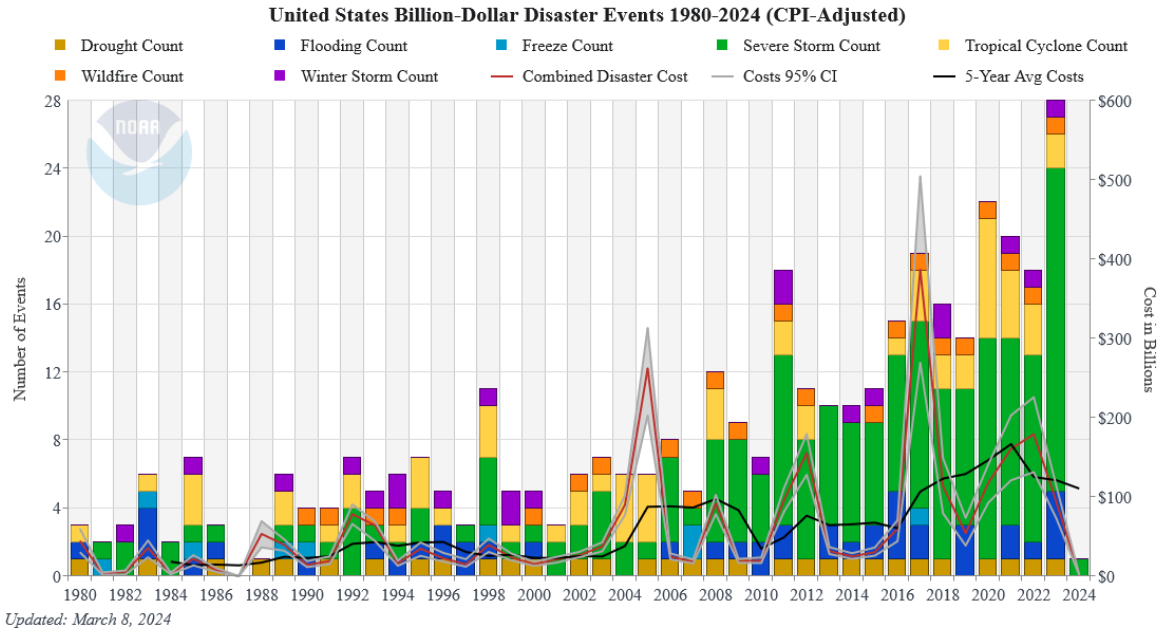

Figure 3: Adjusted costs of the disaster events and count of these events in the United States between 1980 and 2024. (Taken from [8])

All in all, it is evident that the climate crisis is a global crisis with environmental, societal, political, and economic impact, emphasising the urgent need to transform towards a sustainable society. However, this transformation requires dramatic changes with regard to our economic and social foundation. Therefore, different strategies to address the excessive amount of greenhouse gas emissions into the atmosphere must be discussed and be implemented.

1.2 Strategies to reduce greenhouse gas emissions- The Electrochemical Cell

The emission of these gases into the atmosphere is the result of a society in which the production of energy and most goods is yet based on fossil resources. Beside capturing and transforming the greenhouse gases into valuable chemicals to reduce their concentration in the atmosphere,[15] preventive measures are also necessary to decrease their production. A cornerstone to address this problem is the usage of renewable energy resources such as solar or wind.[16,17] These resources are not only less harmful to the climate but also feature a higher availability and larger deposits around the globe than fossil resources. In order to use these resources, their energy has to be converted or to be stored in energy devices. Such devices are electrochemical cells as exemplified in the following.[16]

Figure 4 shows a schematic overview of a Galvanic (a) and Electrolytic (b) cell which are conceptually similar.[18] This cell consists of two electrodes which are embedded in a solvent which is either an aqueous electrolyte or a molten salt. The electrodes are connected to an electrical circuit via a Voltmeter which measures the potential difference between the half cells in case of the Galvanic cell or a power source which can apply an electrical potential in the Electrolytic cell.[16,19]

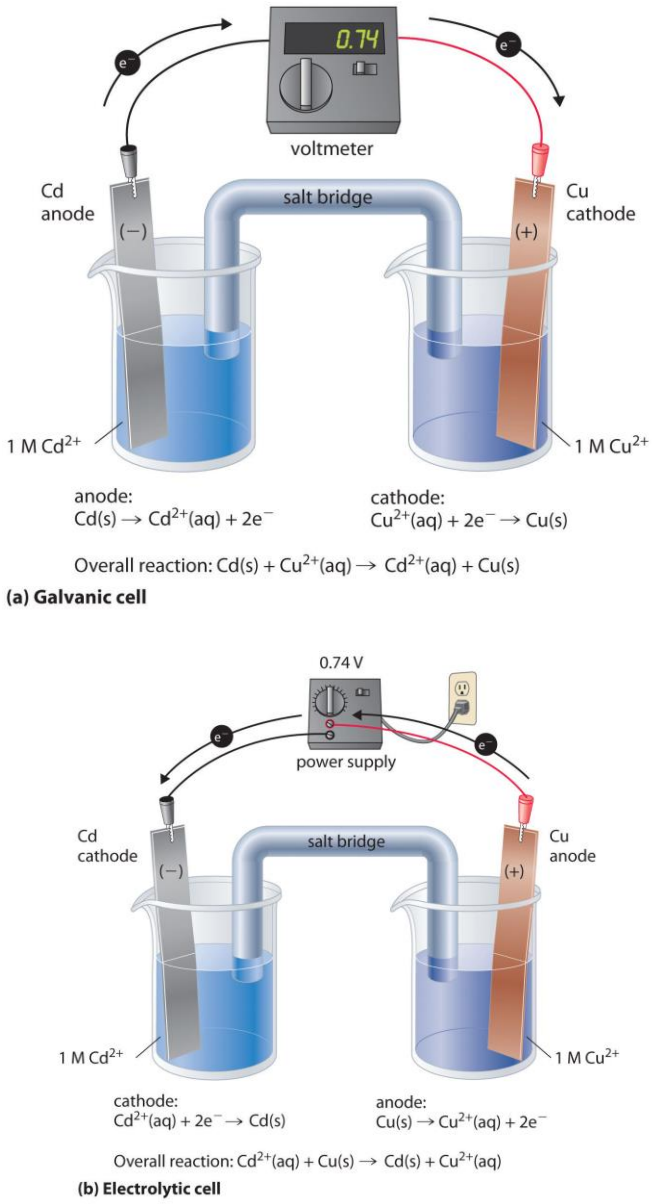

Figure 4: Structure of a a) Galvanic and b) Electrolytic cell, showing the two half cells, the electrodes and the salt bridge. (Taken from [18])

This potential is capable of separating charge and charging the system. However, the Galvanic and Electrolytic cell are different to the processes which happen at each electrode. The charging process happens spontaneously at the Galvanic cell.[19] The oxidation takes place that the anode and electrons accumulate there which then flow to the other electrode. At this cathode, ions in the electrolyte are reduced by these electrons. This process is inverted at the electrolytic cell.[19] While electrons accumulate into the cathode which is negatively charged, charge is depleted from the anode which is getting positively charged by the applied potential.[19] Consequently, oxidative processes happen on the anode surface and reductive reactions occur on the cathode surface. By definition, the oxidation of the reactant A occurs at the anode, following equation (1), while the reduction of the reactant C takes place at the cathode as given by (2), yielding the overall redox reaction (3).[19]

$$A \rightarrow A^{z+} + ze^- \quad (1)$$

$$C^{z+} + ze^- \rightarrow C \quad (2)$$

$$A + C^{z+} \rightarrow A^{z+} + C \quad (3)$$

To avoid "overcharging" of each half cell which would supress each half-cell reaction, a salt bridge connects them so that ions can be exchanged.[19] This ion exchange counteracts to the excess charge in each half cell which might occur due to the constant reduction and oxidation reactions. As a result of these reactions, an electrical current is produced which flows from the anode to the cathode. The standard free energy for the cell is given by (4).[19–21]

$$\Delta G^{\ominus} = -zFE^{\ominus}_{cell} \quad (4)$$

$E^{\ominus}_{cell}$ is the standard cell potential. Starting from this thermodynamic relation, the half-cell reduction potential E_{red} is derived and calculated by the Nernst formula (5):[19–21]

$$E_{red} = E^{\ominus}_{red} - \frac{RT}{zF} \ln \frac{a_{red}}{a_{ox}} \quad (5)$$

$E^{\ominus}_{red}$ is the half-cell standard reduction potential, R is the ideal gas constant, T is the temperature, z is the number of transferred electrons, F is the Faraday constant and a_{red} and a_{ox} are the activity of reduced and oxidized moiety, respectively. The difference between the half-cell potentials gives then the cell potential E_{total}.

$$E_{total} = E_{anode} - E_{cathode} \quad (6)$$

The Nernst equation can be approximated in two steps. Since the activity of each electrolyte and ion is seldom known, the activity coefficient is separated from the concentration of the electrolyte c and the coefficient is included in the half-cell standard potential. Further assuming room temperature (T = 298K), the Nernst equation simplifies to (7):[19–21]

$$E_{red} = E^{\ominus'}_{red} - \frac{0.059\ V}{z} \log \frac{c_{red}}{c_{ox}} \quad (7)$$

$E^{\ominus'}_{red}$ is the formal standard reduction potential, including the activity coefficient. The constant factor 0.059 V is obtained by combining the constants and converting the logarithms.

To be able to measure the (half) cell potentials, a reference is required which is the Standard Hydrogen Electrode. The hydrogen evolution reaction (HER, (8) and (10)) takes place at the cathode, while the oxygen evolution reaction (OER, (9) and (11)) happens at the anode. Note that reactions (8) and (9) are shown at acidic conditions and (10) and (11) show the reactions at alkaline conditions.[16,21–26]

$$2H^+ + 2e^- \rightleftharpoons H_2; \qquad E^e_{red}=0.00V \qquad (8)$$

$$2\,H_2O \rightleftharpoons O_2+4\,(H^+ + e^-) \qquad E^e_{red}=1.23V \qquad (9)$$

$$2\,H_2O + 2e^- \rightleftharpoons H_2 + 2OH^- \qquad E^e_{red}=-0.83V \qquad (10)$$

$$4\,OH^- \rightleftharpoons O_2 + 2\,H_2O + 4e^- \qquad E^e_{red}=0.40V \qquad (11)$$

The potential difference between HER and OER is always 1.23 V regardless of the pH as Figure 5 illustrates which plots the Nernst equations of the HER and OER with respect to the pH, i.e. the Pourbaix plot.[22]

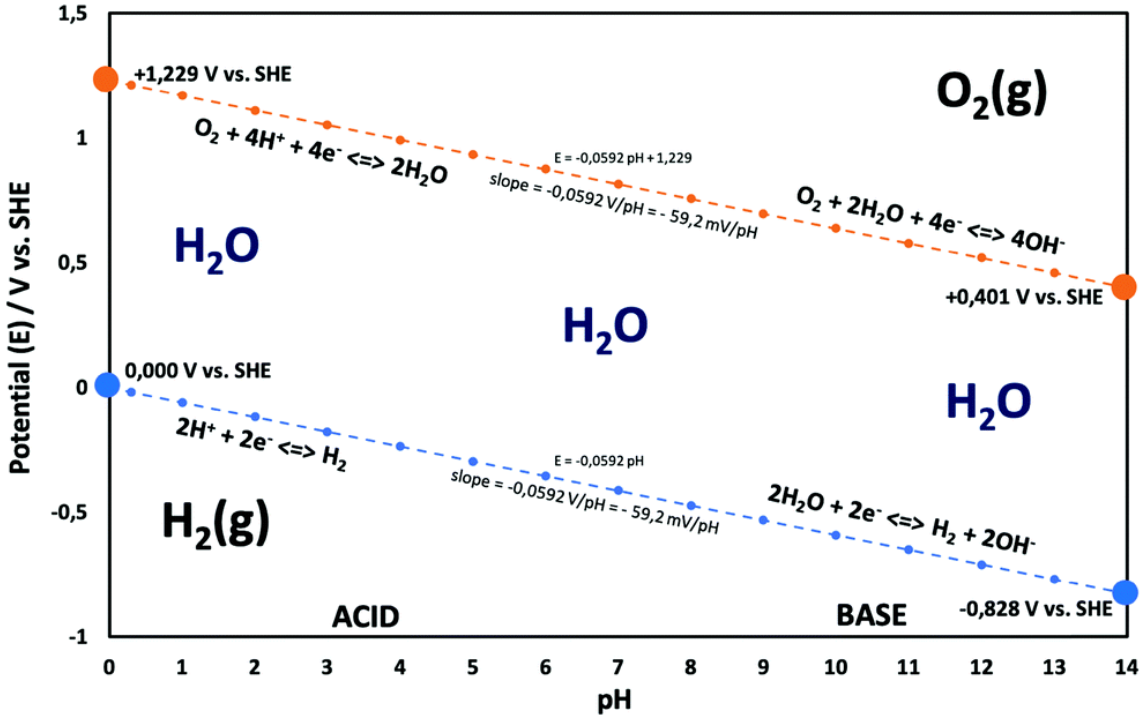

Figure 5: Pourbaix diagram of hydrogen and oxygen, constructed by the Nernst equations of Reactions (8) to (11). (Taken from [22])

The HER has been subject of many studies and research efforts.[22,27–31] Even though it is facile on many materials such as platinum,[27,30] its mechanism is yet not fully understood. However, the OER features an even higher complexity than the HER. Despite the seemingly simple chemistry of this anodic reaction compared to other electrochemical oxidation reactions such as the Nitrogen Oxidation Reaction (NOR) or the oxidation of hydrocarbons,[32] its mechanism and chemistry is still part of many experimental and theoretical endeavours. This thesis will deal with deciphering anodic oxidation reaction with emphasis on the OER whose state-of-the-art will be reviewed in the following.

2 Thesis Outline

As it is clear from the introduction, electrochemical cells are important tools to address the challenges of the climate crisis. The anodic reaction which plays a crucial role in these devices is the Oxygen Evolution Reaction (OER). Therefore, understanding the OER in electrochemical systems from a energetic, kinetic and electronic point of view is essential to decipher trends and to predict whether an electrocatalyst will be a poor or efficient electrocatalyst.

Firstly, we detail the chemistry of the OER and explain different possible mechanisms. Herein, despite the seeming simplicity of the OER, the mechanistic complexity is revealed due to a variety of possible different pathways which can be explored. We then give a brief introduction to experimental parameters and techniques such as Tafel plots and the overpotential. In this context, we focus on illustrating the noise ElectroChemical Scanning Tunnelling Microscopy (n-EC-STM) techniques which is utilized to elucidate the active sites inside the electrocatalysts being investigated in this thesis. After this part, we inform the reader about common OER descriptors which are used to rationalize and to predict the performance of electrocatalysts. These descriptors are categorized in thermochemical and electronic descriptors.

The previous section of this thesis is followed by a discussion on various typical OER electrocatalysts. Typically, most efficient electrocatalysts are expensive and scarce noble-metal oxides such as iridium oxide or ruthenium oxide. In the introduction of this thesis, it has been elucidated that the climate crisis intertwines with economic challenges. Particularly, countries with limited financial resources face difficulties in developing and affording energy devices, especially when constructed solely from expensive materials. Consequently, to consider and to address this aspect of the climate crisis, we investigated OER electrocatalysts based on Earth-abundant materials. To provide background to the work presented in the research articles, we review in this section of the thesis the progress in using carbonaceous and manganese-oxide-based materials for electrochemical OER catalysis.

Following this general presentation of the OER as one of the simplest anodic reactions, we unveil other electrochemical oxidation reactions which might also compete with the OER when taking place in an aqueous electrolyte. This chapter focuses on the anodic Nitrogen Oxidation Reaction (NOR). After a brief introduction to the conventional way of nitrate production and short summary of the history of direct nitrogen oxidation, challenges, and strategies with regard to the electrochemical NOR are being explained.

As implied, experimental techniques can already provide comprehensive insights into the nature of electrochemical reactions and catalysts. Nevertheless, computational methods such as Density Functional Theory are valuable tools to further elucidate open questions. For instance, reaction pathways can be probed on an atomistic scale and reaction sites are clearly identified inside a multicomponent material. The comprehension gained from computational modelling can be combined with experimental information to obtain a holistic picture of the electrocatalyst and the reaction in question. In this section, we inform

the reader about the fundamental aspects of theoretical modelling such as the Schrödinger equation, Density Functional Theory and corrections. Additionally, we briefly explain how to calculate electrochemical pathways utilizing the Computational Hydrogen Electrode (CHE).

In the end, the research articles included in this thesis are presented. A brief summary of the respective articles is provided and then the articles and their supplementary information is attached to this thesis.

We aim to tackle the following research objective, leading to appropriate research questions which will be answered in course of this thesis.

Research Objectives:

1. Explain the reason for the enhanced OER activity of Highly Oriented Pyrolytic Graphite (HOPG) with manganese oxide nanosheets (MnO_2NS) compared to pristine HOPG.

2. Find and identify the most active site in these electrocatalysts (HOPG, MnO_2NS/HOPG, CFePc/HOPG and MnO_2NS/CFePc/HOPG) which align with and can explain the experimental results.

3. Explain how the OER competes with other electrochemical oxidation reaction such as the NOR.

Research Questions:

1. Why are manganese oxide nanosheets on HOPG (MnO_2NS/HOPG) more active than pristine HOPG?

2. Why is HOPG functionalized with carbonized iron phthalocyanine (CFePc) even more active than MnO_2NS/HOPG?

3. What is the role of MnO_2NS in this class of materials? How do they contribute to the enhanced activity as seen in the experiments?

4. What are the reasonable mechanisms which can explain and map the energetic landscape and therefore the activity?

5. Which factors determine whether the OER outperforms other electrochemical oxidations reactions such as the NOR?

3 Electrochemical Oxidation Reactions

We are discussing the state-of-the-art of the OER in the next chapters to provide the foundation in understanding oxidation reactions and the challenges in deciphering them. Our emphasis will be on OER at MnO_x-based and carbonaceous materials. At the end of this chapter, we will briefly summarize the efforts on other electrochemical oxidations such as the NOR.

3.1 The Oxygen Evolution Reaction

As stated above, the OER is conceptually one of the simplest reactions which can be imagined as outlined in reactions (9) and (11). However, despite this fact and its early discovery in the 19th century by Paets van Troostwijk/Deiman and Nicholson/Carlisle,[24] it is still an enigmatic to scientists. For instance, the mechanism and ideal catalyst which catalyses this reaction at low thermodynamic and kinetic barriers are yet unknown and have been formulated as research questions multiple times.[16,23,24,33] As outlined in the introduction, efficient and abundant materials are needed to transform from a fossil-fuel-based to a sustainable society. Nevertheless, the manifold nature of possible OER pathways is the reason why identifying the most efficient catalyst is challenging and formidable.

3.1.1 Possible OER mechanisms

This chapter deals with the OER paths which are recognised the most in literature. It is crucial to distinguish between mechanisms which occur at acidic and alkaline conditions. The following mechanisms are known and presented in (12) to (27) in Table 1.[22–24]

Table 1: Overview of the different OER mechanisms.[23,24,34]

Acidic Conditions	**Alkaline Conditions**	
Electrochemical path		
$* + H_2O \rightleftharpoons *OH + H^+ + e^-$	$* + HO^- \rightleftharpoons *OH + e^-$	(12)
$*OH \rightleftharpoons *O + H^+ + e^-$	$*OH + HO^- \rightleftharpoons *O + H_2O + e^-$	(13)
$*O + H_2O \rightleftharpoons *OOH + H^+ + e^-$	$*O + HO^- \rightleftharpoons *OOH + e^-$	(14)
$*OOH \rightleftharpoons * + O_{2(g)} + H^+ + e^-$	$*OOH + HO^- \rightleftharpoons * + O_{2(g)} + H_2O + e^-$	(15)
Electrochemical Oxide path		
$* + H_2O \rightleftharpoons *OH + H^+ + e^-$	$* + HO^- \rightleftharpoons *OH + e^-$	(12)

Table 1: Overview of the different OER mechanisms (continued).[23,24]

Acidic Conditions	Alkaline Conditions	
Electrochemical Oxide path		
$*OH \rightleftharpoons *O + H^+ + e^-$	$*OH + HO^- \rightleftharpoons *O + H_2O + e^-$	(13)
$2*O \rightleftharpoons 2* + O_{2(g)}$		(16)
Oxide path		
$* + H_2O \rightleftharpoons *OH + H^+ + e^-$	$* + HO^- \rightleftharpoons *OH + e^-$	(12)
$2*OH \rightleftharpoons *O + * + H_2O$	$2*OH \rightleftharpoons *O + * + H_2O$	(17)
$2*O \rightleftharpoons 2* + O_{2(g)}$		(16)
Krasil'shchkov path		
$* + H_2O \rightleftharpoons *OH + H^+ + e^-$	$* + HO^- \rightleftharpoons *OH + e^-$	(12)
$*OH \rightleftharpoons *O^- + H^+$	$*OH + HO^- \rightleftharpoons *O^- + H_2O$	(18)
$*O^- \rightleftharpoons *O + e^-$		(19)
$2*O \rightleftharpoons 2* + O_{2(g)}$		(16)

Wade and Hankerman's path		*Yeager's path*	
$2(* + H_2O) \rightleftharpoons *O + *OH_2 + 2(H^+ + e^-)$	(20)	$*^z + HO^- \rightleftharpoons *^zOH + e^-$	(22)
$*O + 2*HO^- \rightleftharpoons 2(* + e^-) + *OH_2 + O_{2(g)}$	(21)	$*^zOH + \rightleftharpoons *^{z+1}OH + e^-$	(23)
		$2(*^{z+1}OH + HO^-) \rightleftharpoons 2(* + H_2O) + O_{2(g)}$	(24)
		Bockris path	
		$* + HO^- \rightleftharpoons *OH + e^-$	(12)
		$*OH + HO^- \rightleftharpoons *H_2O_2 + e^-$	(25)
		$*H_2O_2 + HO^- \rightleftharpoons *OOH^- + H_2O$	(26)
		$*H_2O_2 + *OOH^- \rightleftharpoons 2* + H_2O + HO^- + O_{2(g)}$	(27)

As it is evident from Table 1, many possibilities exist how the OER can proceed and consequently many degrees of freedom must be taken into account. In fact, many other factors such as the electrode material, the electrolyte and the interactions at the solid-liquid interface determine the thermodynamic and kinetic properties of the OER in a given system. The Eley-Rideal-type electrochemical path only considers reactants which originate from the electrolyte.[23] It is similar to the Langmuir-Hinshelwood electrochemical oxide path, but two *O combine to dioxygen.[23] Different from the electrochemical oxide path, the oxide path features only one electrochemical proton-electron transfer step in the beginning, while the other steps are purely thermodynamic steps. Water is formed in the second step. Krasil'shchkov path is rather complex, however, when considering the electronic nature of step (18) and (19). Herein, the proton-electron transfer is decoupled which is challenging to model by standardized electronic-structure methods.[23]

The previous mechanisms can happen both in acidic and alkaline conditions. Nevertheless, Wade and Hankerman's path exclusively occurs in acidic conditions in which one water molecule is oxidized to *O. *O is then oxidized to dioxygen and, notably, an *OH adsorbate is reduced to adsorbed water $*OH_2$ at the same time.[23] Two other mechanisms take place exclusively in alkaline conditions. Yeager's path involves the adsorption site which gets oxidizes after adsorption of *OH. Two *OH adsorbates combine then to dioxygen and water, which shows again a concerted redox mechanism. Different from all other paths, Bockris path contains the formation of hydrogen peroxide which disproportionate into dioxygen, water and *OH.[23]

Besides obtaining oxygen from the reactants in the electrolyte, oxygen moieties in the lattice of the catalyst can be involved, for instance, in the (electrochemical) oxide paths. However, it has been demonstrated that the OER could also take place in the electrolyte as shown in Figure 6.[24]

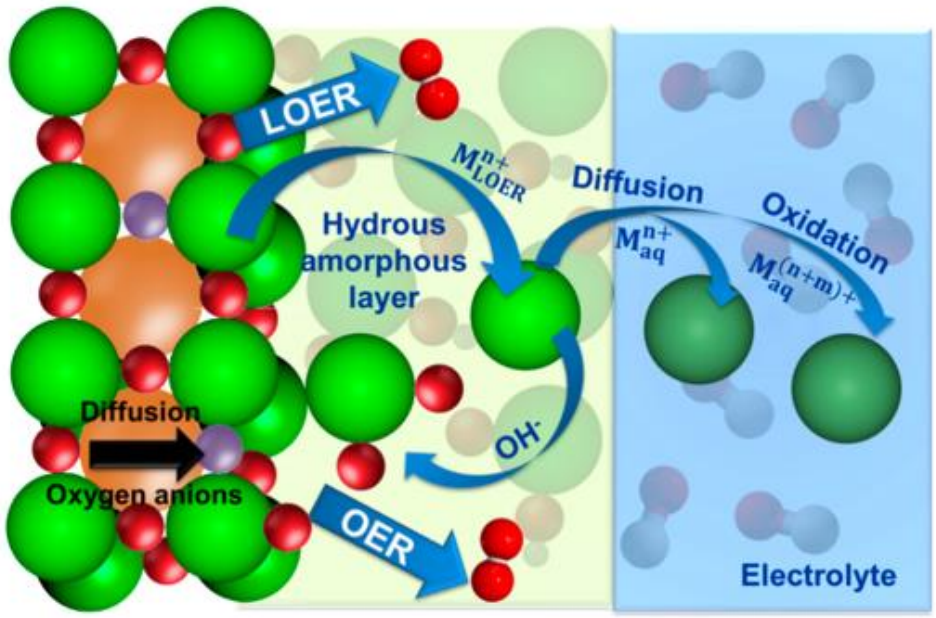

Figure 6: Overview of the Solid-Liquid Interface under OER conditions and its effect. On top, different locations of where the OER can take place are shown. (Taken from [24])

Because of the oxidatively operating OER conditions, the structure of the catalyst is affected, and an amorphous top layer can be formed which can be catalytically more active than the pristine material.[24] This phenomenon has been shown for IrO_2 which changes its surface structure during the OER. However, metal cations might leach into the electrolyte and into the electrochemical double layer. There, they can also be catalytically active and drive the OER.[20,35]

Considering all these different possibilities in how oxygen is formed during the OER, researchers have defined various techniques and descriptors in order to measure and predict the trends with regard to the performance of the catalyst. In the following, we are reviewing the most accepted experimental techniques and descriptors found in literature.

3.1.2 Experimental Techniques

3.1.2.1 The Three-Electrode Setup

In order to control and investigate electrochemical systems experimentally, a third electrode is added to the setup which is outlined in Figure 4. The reason to utilize extend the given experimental setup is to obtain reproducible results. The setup consists of a working electrode, a reference electrode and a counter electrode as shown in Figure 7.[19,36]

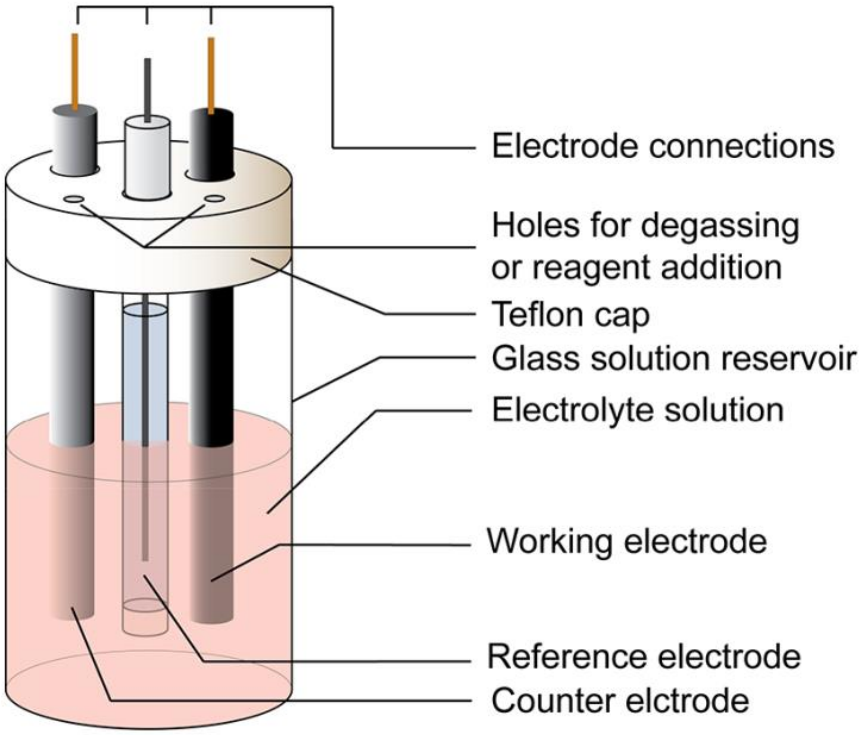

Figure 7: Three-electrode setup. The working electrode at which the electrochemical is monitored is connected to the reference electrode via a voltameter. The potentiostat ensures a constant potential difference between the working and counter electrode. (Taken from [36])

Since electrochemical reactions occur at both the working and counter electrode at different rates, a potential difference between them builds up.[36] The reference electrode

measures the potential built up at the working electrode. Typical reference electrodes are the Standard Hydrogen Electrode (SHE) whose potential is by definition 0V, the Reversible Hydrogen Electrode (RHE) which changes its zero as a function of electrolyte pH and the mercury/mercury oxide (Hg/HgO) electrode.[19,36] All of them feature stable and known reduction potential, high resistance and negligible current. This experiment set up can be used to obtain Linear Sweep Voltammograms (LSV) and Cycle Voltammograms (CV).

3.1.2.2 Linear Sweep Voltammetry (LSV)

To evaluate the performance of an electrocatalyst, linear sweep voltammetry can be performed. Herein, the potential at the working electrode is gradually increased as presented in Figure 8.

a)

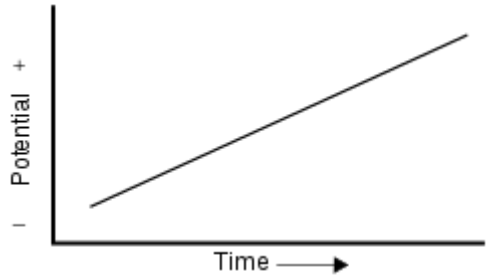

b)

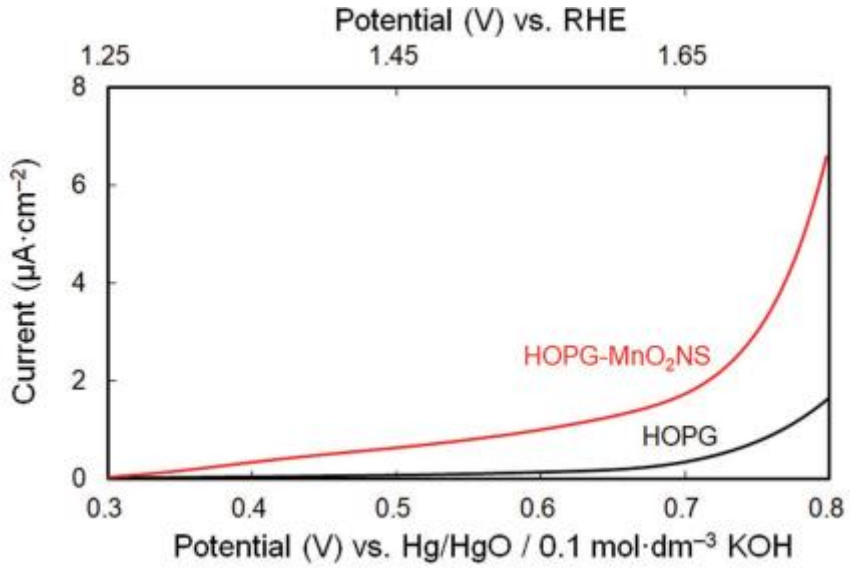

Figure 8: Scheme of a LSV experiment. a) The graph shows how the applied potential at the working electrode is increased as function of time. (Taken from [37]). b) Example of a LSV plot. (Taken from [38])

When performing such an experiment, the scan rate determines how much the potential increases over time. After reaching the reduction (or oxidation) potential of the adsorbates on the surface, the current density grows since the exchange rate of electrons between electrode and electrolyte is enhanced.[19] LSV is used to determine the electrocatalytic activity of a catalyst, the concentration of adsorbates or their characterization. Instead of ramping the potential over time, it is also possible to switch at a point in time.[36]

3.1.2.3 Cyclic Voltammetry (CV)

In case of reversible redox processes, cyclic voltammetry is performed. Here, the applied potential is ramped to a target potential at a point in time and decreased to the starting potential. The procedure is sketched in Figure 9. It also shows an example of CV for ferrocene (Fc) and the concentration of the reduced and oxidized species in the electrolyte.[36]

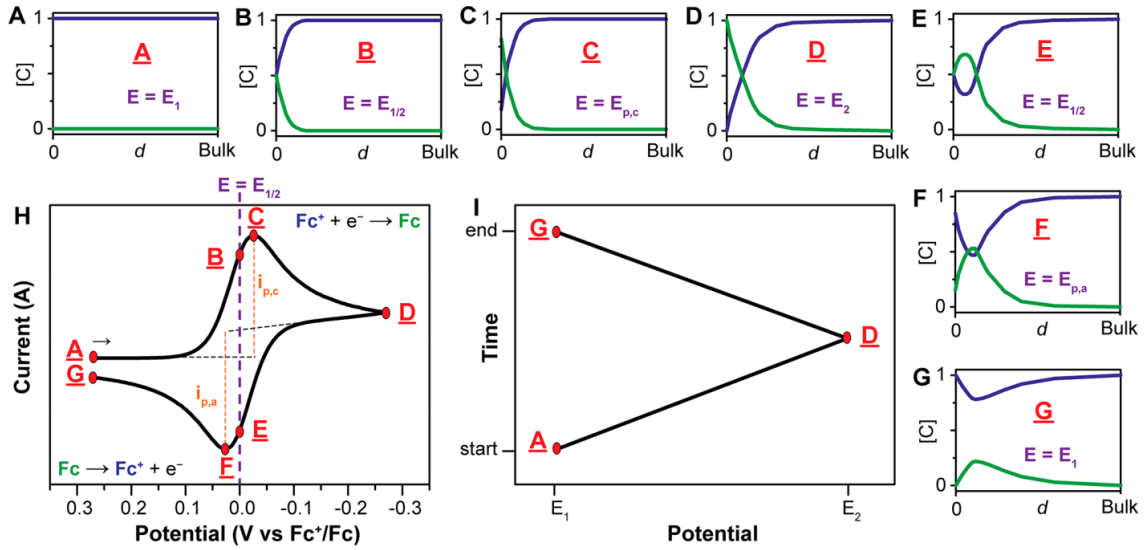

Figure 9: Scheme of a CV experiment. A to G shows the concentration profiles of the oxidized Fc^+ (blue) and reduced Fc (green) at different potentials E as shown in H. I exemplifies a triangular function how a CV experiment is performed. (Taken from [36])

Note that the exemplified CV in Figure 8 H is presented in the US standard in which the oxidation is shown on the left side of the CV, while the reduction is shown on the right.[36] The measurement starts at a positive potential at which a reaction is not expected and only oxidized Fc^+ are present in the electrolyte (Figure 8 A).[36] The potential is then changed to a reducing potential. Consequently, the concentration of reduced moieties Fc increases, particularly at the electrode. A maximum cathodic current density of $i_{p,c}$ is observed at a certain potential $E_{c,max}$ since the diffusion of Fc^+ from the bulk electrolyte to the electrode and the depletion of Fc from the electrode to the electrolyte are in equilibrium.[36] When higher potentials than $E_{c,max}$ are applied, the mass transport is limited by the depletion of Fc into the electrolyte and therefore the current yield is reduced. When the target potential is reached, the applied potential is changed back towards the starting potential. Due to the presence of reduced Fc and the diffusion barriers, the concentration profiles in Figures 8 E to G are different from the profiles in A to D. The anodic peak appears at $E_{a,max}$, yielding a maximum current density of $i_{p,a}$.[36]

If a single-electron transfer process is (electro-)chemically reversible, the separation of each peak is approximately 2.22RT/F or 57mV at 298.15K, with R the universal gas constant and F Faraday's constant.[36] On top, the height of each peak is identical their ratio is therefore one. Such a process is also called Nernstian process. This feature enables to draw conclusions about the kinetics of (coupled) electrochemical and chemical processes.[36] If two electrochemical processes are coupled and the second reaction is thermodynamically more favored than the first electron transfer, two peaks still appear in the CV.[36] However,

their separation halves to 28.5mV at 298.15K, corresponding to a Nernstian two-electron-transfer process. Contrary, if the first process is more favored than the second reaction, the peak-to-peak separation increases up to 140mV and four peaks in total appear.[36] If the second reaction is an irreversible chemical transformation at a slow kinetic rate, the CV of these reactions is identical to a single-electron transfer reaction. When its rate increases, however, the CV obtains non-Nernstian features such as different ratios for the anodic and cathodic peaks and peak-to-peak distances different from 57mV at room temperature.[36] Systematic variations of the scan rate can provide further insights into the underlying processes. In case of a reversible chemical reaction which occurs prior to an electrochemical step, the nature of the first reaction determines the shape of the CV. If the first reaction is fast, the CV appears to describe a Nernstian single-electron transfer.[36] In case of a slow rate of the first reaction, it dictates the reaction network, and the shape of the CV obtains the shape of non-Nernstian processes.

3.1.2.4 Noise Electrochemical Scanning Tunnelling Microscopy (n-EC-STM)

Noise Electrochemical Scanning Tunnelling Microscopy (n-EC-STM) is a combination of electrochemical techniques explained above and STM which is being explained briefly in the following.

The setup consists of a tip which is only a few atoms thick and is embedded into an experimental machinery as shown in Figure 10. A voltage between the sample surface and the tip is applied.[39,40] As a consequence, electrons at exposed quantum states tunnel from the orbitals of the surface atoms to the tip which generates a current. This tunnelling current is a function of the distance between the surface and the tip.[40]

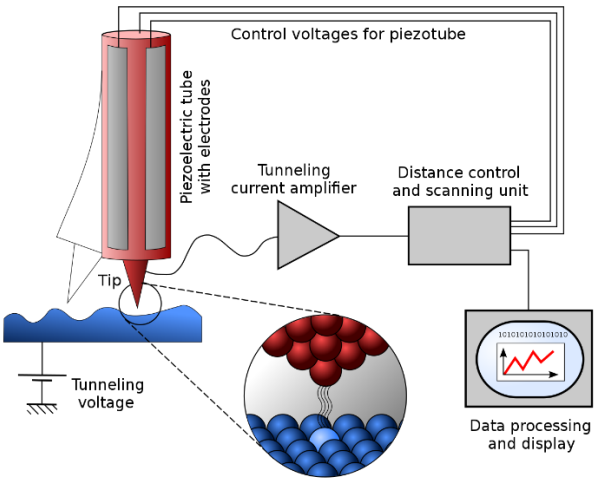

Figure 10: Scheme of a STM setup. The tip with an apex diameter of maximum various atoms moves over the surface, controlled by a piezoelectric scanner at small distances. A voltage is applied between the surface and the tip which results in a current of nanoamperes. This current is amplified, and a surface profile is obtained. (Taken from [41])

Typical distances between tip and sample are between 0.4 and 0.7nm.[40] Basically, two modes to measure the x-y plane of the sample are possible. The constant-current mode ensures that the distance between the tip and the surface is constant by keeping the current constant.[40,42] When the tip encounters a change in the surface morphology like a step or a

valley, the height of the tip is adjusted. These measurements are very slow as the z position of the tip is adjusted, following the feedback of the tunnelling current to keep it constant. Another mode, being also demonstrated in Figure 11, is the constant-height mode in which the distance between tip and surface is constant and tunnelling current can fluctuate.[40]

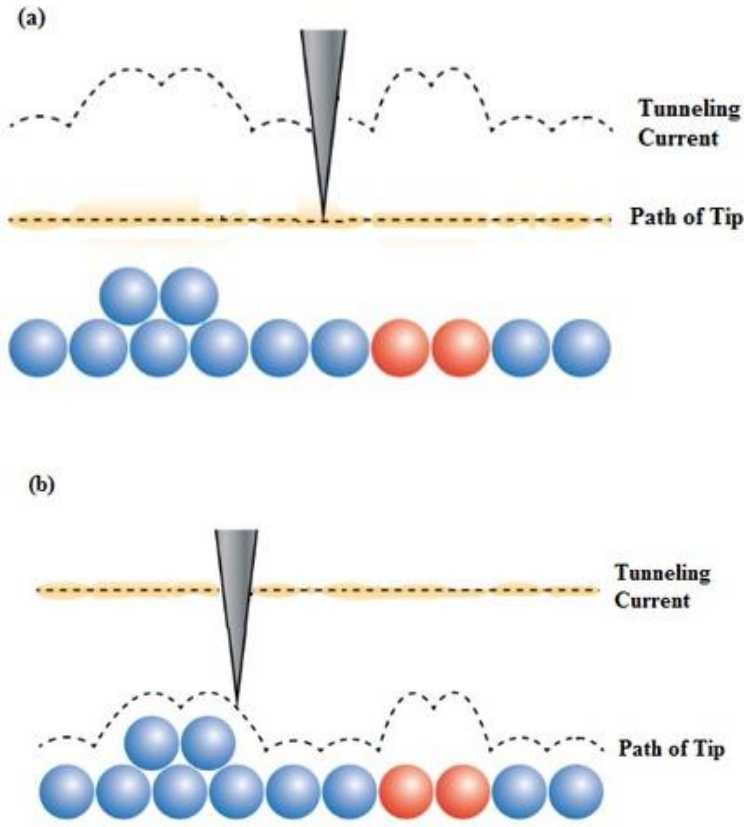

Figure 11: Different STM modes. a) shows the constant-height mode in which the distance between tip and surface is constant, while the tunnelling current fluctuates as a function of the tip height. b), however, shows the constant-current mode in which the tip changes its z position upon response due to changes of the surface morphology. (Taken from [41])

The measurements in constant-height mode are faster than in constant-current mode and enable to obtain STM images in high resolution.

While STM experiments can also be performed in vacuum or air, EC-STM are carried in the (liquid) electrolyte.[43,44] Apart from this difference of most conventional STM experiments, the sample is the working electrode of a three-electrode setup.[45] The other two electrodes are added to control the applied potential at the sample. Note that most of the tip but the apex must be insulated.[45–47] EC-STM usually investigate the electrode morphology before and after the electrochemical experiment. However, the n-EC-STM technique is capable of monitoring the electrochemical processes at the electrode *in operando*.[38,45] The incoming reactants and outgoing products perturbate the tunneling current which becomes visible in the STM image. In the constant-current mode, the flow of reactant to and products from the electrode results in disrupting the current and, as a consequence of maintaining the current, in retracting the tip.[45,48] These events become

visible in the STM image as spikes or noise which correspond to reaction activities at the designated spot in the material. This principle is outlined in Figures 12a and b.[48]

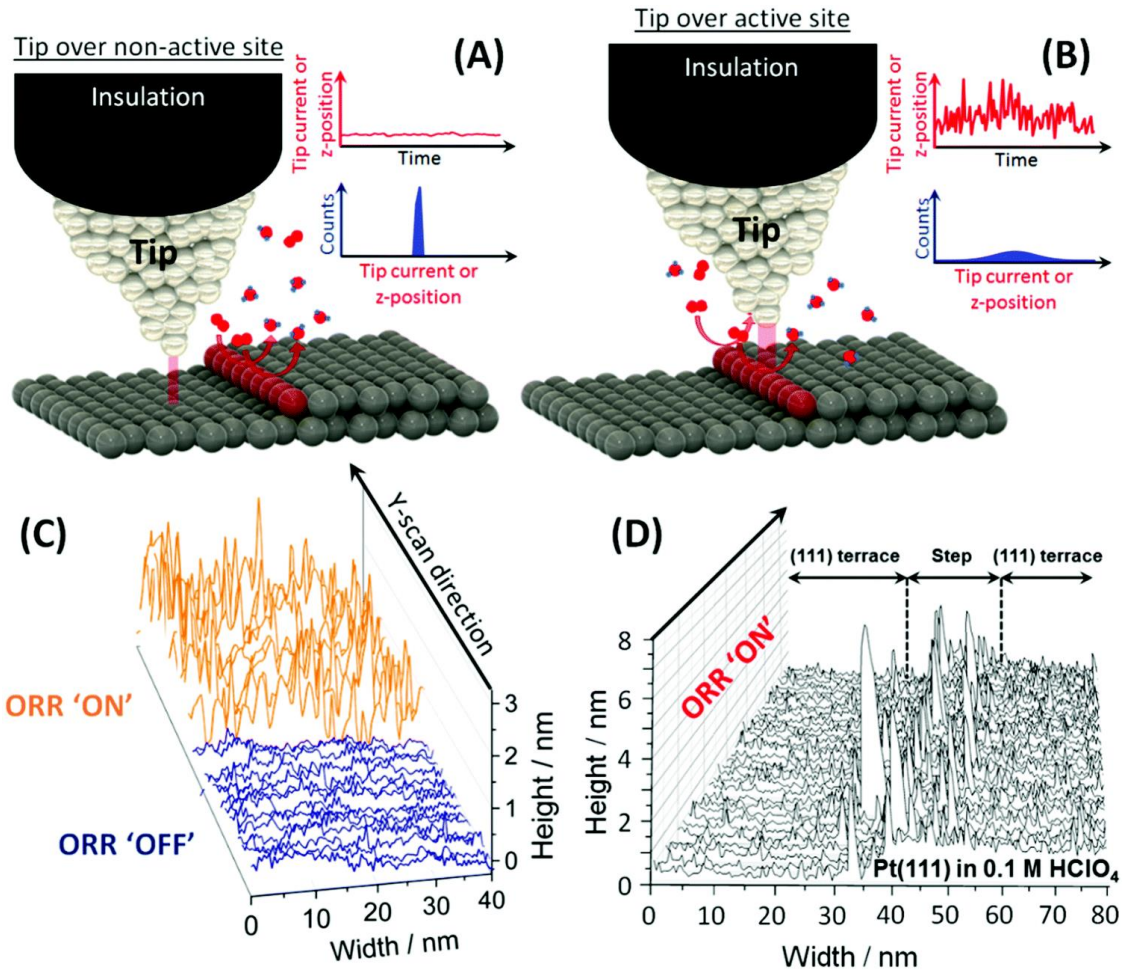

Figure 12: Principles and images of an n-EC-STM experiment. a) and b) show the n-EC-STM measurement of the Oxygen Reduction Reaction (ORR) on a platinum surface with step sites. a) exemplifies a scenario in which the tip is located at an inactive spot, while b) presents a situation in which the tunneling current is perturbated by reactants and products. The z position of the tip or current is almost constant and its distribution is narrow in a). In contrast, these parameters fluctuate and are broadly distributed in the scenario in b). c) depicts a typical n-EC-STM image in which the line scans at reaction conditions ('ON') and without applied potential ('OFF') are contrasted. The reaction is represented as noise in the image. d) shows that the ORR takes place at the steps of platinum surface, being indicated by the larger noise at this location than at the flat terraces. (Taken from [48])

Due to the flow of molecules in the gap between tip and sample, the line scans look different whether or not a potential applied.[45,48] Since the tunneling current is disrupted and the tip is retracted, the line scans feature much more noise when potential is applied than without applied potential. Such a comparison is shown in Figure 12c. Note that the noise behavior is a function of the selected electrolyte, the material and the applied potential.[48] The atomic resolution of STM allows to distinct the origin of electrocatalytic activity to certain locations in the material. As depicted in Figure 12d, the noise at a step between two flat platinum terraces exhibits higher activity for the Oxygen Reduction Reaction (ORR)

than the terraces.[48] The noise behavior can be analyzed further. When Ramping Noise Measurements are performed, a CV measurement is conducted in parallel to the n-EC-STM experiment.[48] Such an analysis helps to reveal a potential dependence of the noise. If the noise exhibit symmetry with regard to the applied potential, the experiment is independent of the applied potential. To quantify and to compare the activity at different locations, the deviation of slopes between measured data points has been proposed as a parameter.[38] Here, the derivative of this slope is taken and quantified. An active area features a broader distribution of this quantity than inactive areas, and therefore this parameter allows to compare the activity between different spots in the material. The n-EC-STM technique has been used and has become a useful tool to elucidate the nature of various electrocatalysts.[38,45,48–51] Besides the quantities which are specifically useful for n-EC-STM, other parameters are used in electrochemistry to examine catalyst.

3.1.3 Experimental Parameters

3.1.3.1 Overpotential η_{OER}

The experimental overpotential η_{OER} is defined as the difference between the equilibrium potential (U_{eq}=1.23V) and potential E which needs to be applied to reach a certain current density.[16,20]

$$\eta_{OER} = E - 1.23V \tag{28}$$

The threshold for the current density is conventionally set to 10mA·cm^{-2}.[20]

3.1.3.2 Tafel slope and exchange current density

While the overpotential provides information about the thermodynamic nature of an electrochemical reaction, the Tafel analysis helps to elucidate the kinetics, but also provides information about the overpotential. The Buttler-Volmer equation gives information about the current density i and is given by (29).[16,20,22,23]

$$i = i_0 \left[e^{\frac{\alpha_a nFE\eta}{RT}} + e^{\frac{\alpha_c nFE\eta}{RT}} \right] \tag{29}$$

$\alpha_{a/c}$ and i_0 are the anodic (a) and cathodic (c) transfer coefficients and exchange current density, respectively. Assuming that the current is mainly produced by anodic contribution, (29) can be simplified to (30), the Tafel equation.[16,20,22]

$$i \approx i_0 e^{\frac{\alpha_a nFE\eta_{OER}}{RT}} \tag{30}$$

In order to obtain the exchange-current density which is the current density at the equilibrium potential, (30) is re-formulated in a logarithmic form (31).[20]

$$\log(i) = \log(i_0) + \frac{\eta_{OER}}{b} \tag{31}$$

b is the Tafel slope which is defined as (32).[20]

$$b = \frac{\partial \eta_{OER}}{\partial \log(i_0)} = \frac{2.303RT}{\alpha_a F} \tag{32}$$

The Tafel slope measures therefore the change of the current density with respect to the overpotential. The higher the Tafel slope is, the more overpotential is required to obtain a certain current density as indicated by Figure 13.[20]

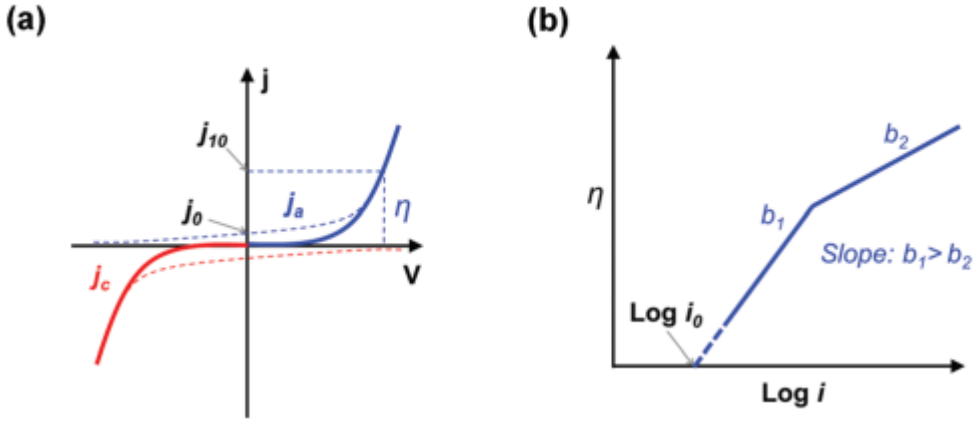

Figure 13: a) shows a LSV plot with a cathodic and anodic current j_c and j_a, the exchange current j_0 and the overpotential η at current density of 10mA cm^{-2} j_{10}. The Tafel plot in b) exemplifies two electrochemical experiments with Tafel slopes b_1 and b_2 in which b_2 represents a more active material than b_1 does. (Taken from [20])

Since the OER is an anodic reaction, its Tafel slope is positive. The Tafel slope is connected to the energy of the transition state.[20,21] Therefore, a high Tafel slope indicates a kinetic barrier which yields by definition a low exchange-current density, being the zero of this function.[20] The transfer coefficient determines further the Tafel slope as it quantifies how much the kinetic barrier is lowered upon applying potential. It is defined as[52]

$$\alpha_a = \frac{RT}{F}\frac{\partial i_0}{\partial E} \tag{33}$$

Note that for α_c the sign changes. To estimate the transfer coefficient in a multistep reaction such as the OER, Bockris and Reddy derived (34).[53]

$$\alpha_a = \frac{n_b}{\omega} + n_r\beta \tag{34}$$

n_b is the number of electrons which are transferred back before the rate-determining step takes place, ω is the number of steps which take place before, n_r is the number of electrons participating in the rate-determining step and β is the symmetry factor (usually 0.5).[20,53] If, for instance, the first electron transfer is the rate-determining step n_b is 0 and n_r is 1 so that a transfer coefficient of 0.5 is obtained.

3.1.3.3 Faradaic efficiency F_e and Turn over frequency (TOF)

The Faradaic efficiency is defined as the current being used to produce the desired product. It is therefore the yield of the reaction which is the quotient of produced and theoretically produced amount of product [P] and $[P]_{theo}$ or the amount of [P] at a certain current j over time t.[21]

$$F_e = \frac{[\mathrm{P}]}{[\mathrm{P}]_{theo}} = \frac{nF[\mathrm{P}]}{jt} \tag{35}$$

It is consequently a yield parameter, while the TOF quantifies the kinetic efficiency of an electrocatalyst since it indicates how much product is formed at certain overpotential.[21]

$$TOF = \frac{i_0 A}{\mathrm{nFg}} \tag{36}$$

A is the area of the electrode and g is the number of active sites in the electrocatalyst.

3.1.4 OER Descriptors

3.1.4.1 Thermochemical Descriptor

The thermochemical descriptor was proposed by Man et al. and is based on the electrochemical path and the Computational Hydrogen Electrode (CHE; see Chapter 4.12).[54] To calculate the change in free energy, the relations (37) to (40) are defined.[54]

$$\Delta G_1 = \Delta G_{HO^*} - \Delta G_{H_2O_{(l)}} - eU + k_b T \ln a_{H^+} \tag{37}$$

$$\Delta G_2 = \Delta G_{O^*} - \Delta G_{HO^*} - eU + k_b T \ln a_{H^+} \tag{38}$$

$$\Delta G_3 = \Delta G_{OOH^*} - \Delta G_{O^*} - eU + k_b T \ln a_{H^+} \tag{39}$$

$$\Delta G_4 = \Delta G_{O_{2(g)}} - \Delta G_{HOO^*} - eU + k_b T \ln a_{H^+} \tag{40}$$

$\Delta G_{H_2O_{(l)}}$, ΔG_{HO^*}, ΔG_{O^*}, ΔG_{HOO^*} and $\Delta G_{O_{2(g)}}$ are the free formation energy of water, and the adsorbates *OH, *O and *OOH and dioxygen, respectively, e is the elemental charge, U is the applied potential, k_b is Boltzmann's constant and T the temperature. The temperature is set to room temperature (T = 298.15 K) and the pH is set to 0, although the thermodynamic nature of the OER in this framework is independent of the pH. The overpotential of the OER, η_{OER}, is obtained as the difference between the potential-determining step (PDS) ΔG_{max} and the applied (equilibrium) potential U_{eq} (41).[54]

$$\eta_{OER} = \frac{\Delta G_{max}}{e} - U_{eq} \tag{41}$$

The authors screened a vast space of different catalysts and found two crucial relations:[54]

1. The free-energy difference between ΔG_{HO^*} and ΔG_{HOO^*} is approximately constant by 3.22 eV unlike the ideal value of 2.46 eV. Therefore, the thermodynamic nature of an OER catalyst is determined by the position of ΔG_{O^*} within the free-energy space.
2. The realisation of the first key finding allows the definition of a descriptor which is the difference ΔG_{O^*}-ΔG_{HO^*}. Consequently, volcanos such as in Figure 14 for each material class can be obtained.

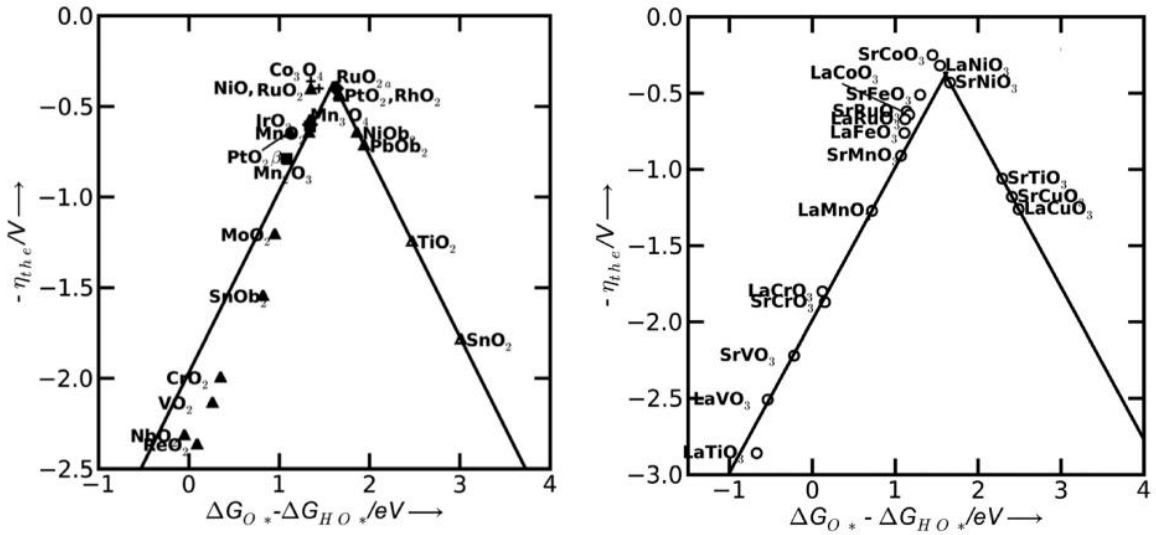

Figure 14: Volcano plot in which the overpotential is plotted at the OER descriptor ΔG_{O^*}-ΔG_{HO^*}. Rutile transition metal dioxides and perovskites are shown on the left and right side, respectively. (Taken from [54])

Here, the calculated overpotential is plotted to the descriptor ΔG_{O^*}-ΔG_{HO^*} and a volcano-shaped relation is obtained, with most active catalysts at the apex of the volcano.[54] These ideal catalysts feature the optimal binding energy of the respective intermediates, while the catalysts at the legs overbind or underbind a moiety as following Sabatier's principle.[54] The predictions of the CHE-based screening agree with experimental results and allow, therefore, valuable insights into the catalytic OER performance of materials. However, various approximations are made here such as neglecting solvation and interfacial effects, the effect of applied potential on the electronic and geometric structure of the catalyst and kinetic effects. Note that it is found for the latter effect that the formation of *OOH is kinetically determining the OER pathway and can be universally taken into account. Although CHE predictions are still powerful, other descriptors have been proposed. The Electrochemical-Step Symmetry Index (ESSI) by Govindarajan et al. addresses shortcomings when the scaling relation between ΔG_{HO^*} and ΔG_{HOO^*} seems to break down and is defined as[55]

$$\eta_{OER,ESSI} = \frac{1}{ne}\sum_{i=0}^{n}\Delta G_i - U_{eq} \tag{42}$$

Herein, all electrochemical steps above the equilibrium potential are taken into account and their average is used to calculate the overpotential. Interictally, kinetic effects are taken into account here. Another extension of the CHE-based prediction of the catalytic OER activity is the Electrochemical-Step Asymmetry Index (ESAI) which is defined by (43) to (45).[56,57]

$$\begin{aligned}\eta_{OER,ESAI,1} = \frac{1}{4}\big(&\left|\Delta G_1 - U_{eq}\right| + \left|\Delta G_2 - U_{eq} - \eta_a\right| + \left|\Delta G_3 - U_{eq}\right| \\ &+ \left|\Delta G_4 - U_{eq} + \eta_a\right|\big)\end{aligned} \tag{43}$$

$$\eta_{OER,ESAI,2} = \frac{1}{4}\left(\left|\Delta G_1 - U_{eq} + \eta_a\right| + \left|\Delta G_2 - U_{eq}\right| + \left|\Delta G_3 - U_{eq} - \eta_a\right| + \left|\Delta G_4 - U_{eq}\right|\right) \quad (44)$$

$$\eta_{OER,ESAI,3} = \frac{1}{4}\left(\left|\Delta G_1 - U_{eq}\right| + \left|\Delta G_2 - U_{eq} + \eta_a\right| + \left|\Delta G_3 - U_{eq}\right| + \left|\Delta G_4 - U_{eq} - \eta_a\right|\right) \quad (45)$$

One of three equations is chosen depending on whether the formation of *O, *OOH or dioxygen is rate-limiting at defined overpotential η_a. This descriptor is related to a descriptor $\Delta G_{max}(\eta_a)$ which is the most endergonic step in the thermodynamic landscape.[56] Besides the descriptors based on the difference ΔG_{O^*}-ΔG_{HO^*}, the formation energy of oxides ΔH_f and $\Delta G_{O(V)^*}$-$\Delta G_{O(IV)^*}$ have been proposed.[58] The latter originates from homogenous catalysis and accounts for the change of the oxidation state at the metal center.

3.1.4.2 Electronic Descriptor

Apart from thermodynamic descriptors, which were discussed in the previous section, the electronic structure of the material and the OER intermediates have been taken into account as possible descriptors. To introduce the underlying concepts in this approach, the basic considerations originating from molecular orbital (MO) theory are being reviewed.

Figure 15 shows the MO diagram of dioxygen, water and $^{-}$OH, the key product and reactants in acidic and alkaline conditions.[59]

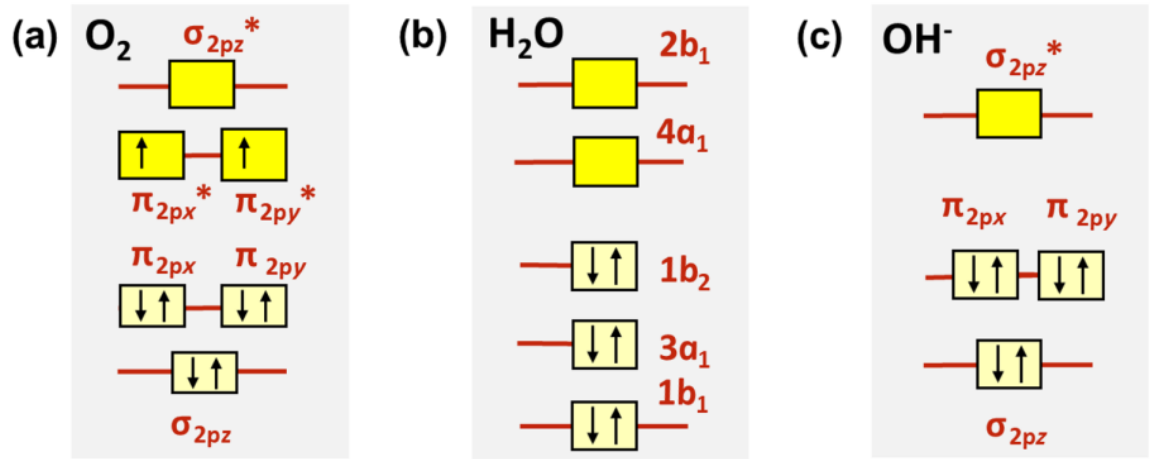

Figure 15: Molecular orbital diagrams of a) oxygen, b) water and c) $^{-}$OH. (Taken from [59])

The key difference between the product and the reactants is that the dioxygen features a triplet ground state with two unpaired spins, while all electrons are paired in both reactants. The orbitals of the latter two molecules hybridize with the *d* states of the active sites upon adsorption and are either physiosorbed only if the hybridisation is weak or chemisorbed when a chemical bond is formed. Accounting for these events occurring at the atomic

level, the OER proceeds according to Figure 16, showing both the OER mechanism of an Eley-Riley and Langmuir-Hinshelwood type in alkaline conditions.[59]

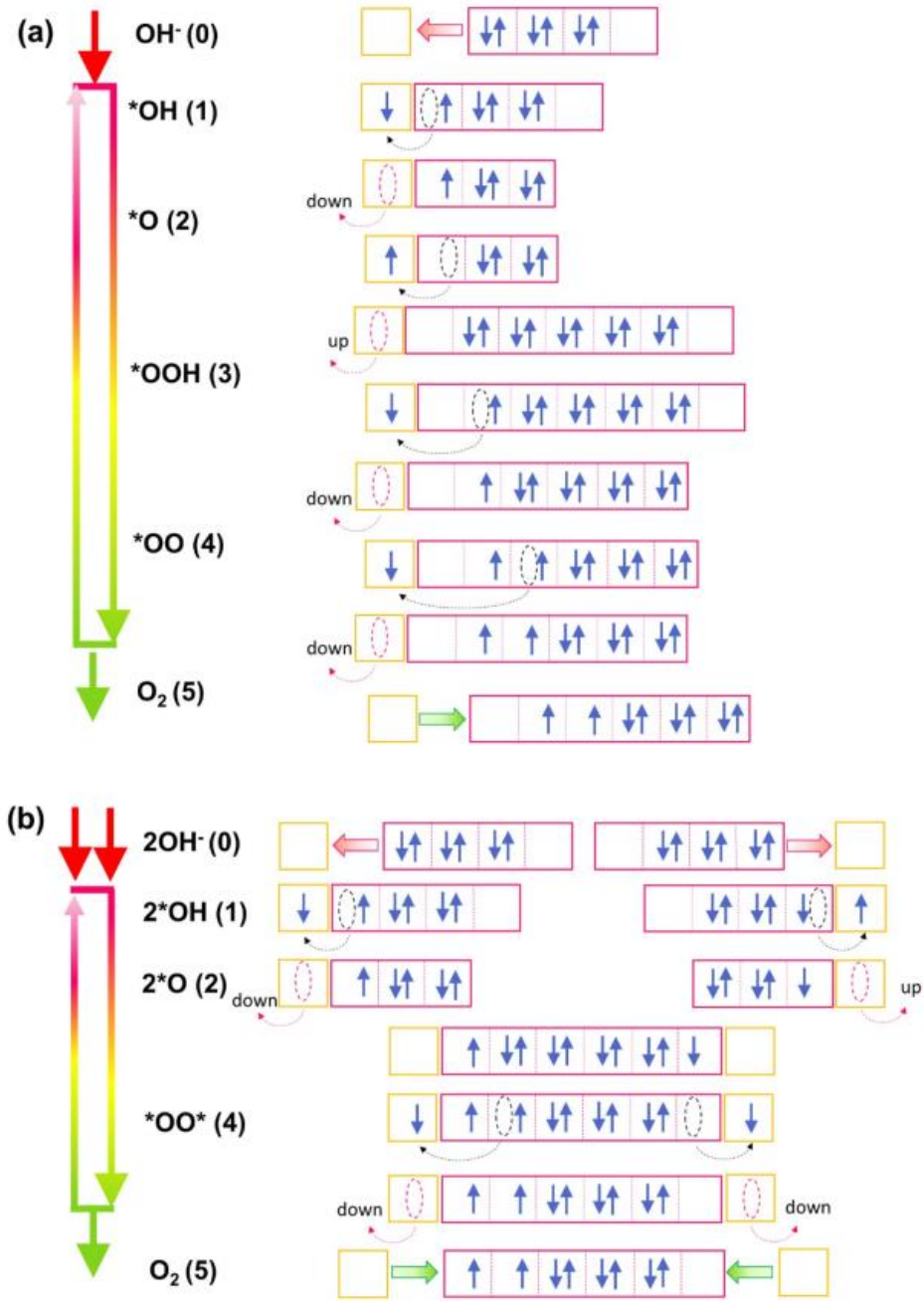

Figure 16: The a) electrochemical and b) electrochemical oxide path at alkaline conditions in which the electronic structure of the catalyst and the adsorbates is considered. (Taken from [59])

It becomes clear here that after hybridization of the catalyst's and reactant states, electrons are continuously withdrawn by the applied potential and the reactants are getting oxidized. Herein, electrons are transferred from the reactants and intermediates to the catalyst. Based on this assumption, the filling of the metal e_g orbital, the energetically highest orbital, has been suggested as a descriptor of the OER performance.[56,60] This orbital takes part into the bonding process and therefore its population determines how strong the bonding of each

intermediate is. In principle, the less the e_g orbital is populated, the stronger the adsorbate binds to the site and vice versa, reflecting Sabatier's principle in here.[56,60] In fact, when plotting the overpotential to the e_g orbital occupancy, a volcano-shaped plot is obtained showing that an occupancy around unity corresponds to efficient OER catalysts. However, the e_g orbital occupancy cannot be utilized as a universal descriptor as, for instance, the presence of different crystal fields such as in binary oxides might complicate the situation.[60] Therefore, descriptors based on the O*2p* orbitals have been proposed. The O*2p* band center (vs the overpotential) or the average O*2p* band energy, given by (46), plotted with respect the difference ΔG_{O^*}-ΔG_{HO^*} have been discussed as insightful OER activity parameters.[61]

$$\bar{\varepsilon}_{2p} = \frac{\int_{\varepsilon_{min}}^{\varepsilon_{max}} \rho_{2p} \varepsilon d\varepsilon}{\int_{\varepsilon_{min}}^{\varepsilon_{max}} \rho_{2p} d\varepsilon} \tag{46}$$

Additionally, *d* band occupancy has been used to reveal the OER trends within a group of materials. The *d* band centers of octahedral and tetrahedral transition metals with respect to O*2p* centers have been used as descriptors when plotted with the overpotential, showing a reasonable correlation. Herein, Sabatier's principle is reflected again by this descriptor when oxygen-containing intermediates are overbound or underbound. This descriptor was used to identify the spinel $MnAl_{0.5}Mn_{1.5}O_4$ as an efficient OER catalyst which was experimentally confirmed.

At last, the Number of Excess Electrons (NEE) has also been suggested as a useful descriptor.[62] Initially, it was used to optimize a TiO_2(110) electrode by varying the number of excess electrons via the bridge *OH, utilizing potentials for hydrogen atoms which contain different numbers of electrons. The pristine surface and models with OER intermediates were probed and Mo^{6+} was suggested as suitable dopant to decrease the overpotential.

3.1.5 OER Electrode Materials

3.1.5.1 Precious Metal Oxides

As Figure 14 already indicates, the group of precious metal oxides such RuO_2 and IrO_2 contains the most efficient OER electrocatalysts.[34,54] Both electrocatalyst exhibit excellent electrocatalytic properties such as low overpotentials (240mV for RuO_2 and 290mV for IrO_2 at i_0=1mA $cm^{-2,}$ on a Ti substrate and in 0.5M H_2SO_4).[20,63–65] However, these properties are dependent on the chosen substrate and electrolyte, and these materials also have a low stability as they dissolve into the electrolyte.[20] Even though improvements have been achieved when tantalum oxide is used as a host material,[66] the latter issue is problematic in economic terms as these materials are rare on Earth and therefore very costly. On top, as Kibsgaard and Chorkendorff have pointed out,[67] many OER electrocatalysts based on Earth-abundant elements such as (Fe,Ni)OOH have been developed and consequently benchmarking novel electrocatalysts against, for instance, RuO_2 and IrO_2 is problematic,[63,68–70] but still common practice. Nevertheless, other OER electrocatalysts based on other materials have also been proposed.

3.1.5.2 Transition Metal Oxides and Manganese Oxides (MnO_x)

As mentioned above, noble-metal-oxide-based materials such as RuO_2 and IrO_2 are too scarce to be accessible for most of the humankind and they are yet too unstable to be used on large scale.[20] Therefore, research on other materials have been conducted to find alternatives for the these very efficient electrocatalysts. For instance, perovskites (ABO_3; A and B are both a transition-metal cations), spinels (AB_2O_4) and layered metal oxides (for example, AOOH or (A,B)OOH such as (Fe,Ni)OOH which is among the most efficient OER anode materials) have drawn attention to researchers due to their OER efficiency similar to noble-metal oxides, their stability and the fact that they can consists of Earth-abundant materials such as iron, nickel or manganese.[33,63,68] Particularly manganese oxides (MnO_x) are interesting materials which have been subject of many studies in the past decades. Manganese is not only one of the most abundant elements on Earth but also is part of nature's solution in water splitting.[71] The Oxygen-Evolving Complex (OEC) in Photosystem II (PSII) drives the OER at reasonable overpotentials (0.3 V at pH 5) and is a manganese-oxide-based nanocluster which is shown in Figure 17.[25,72]

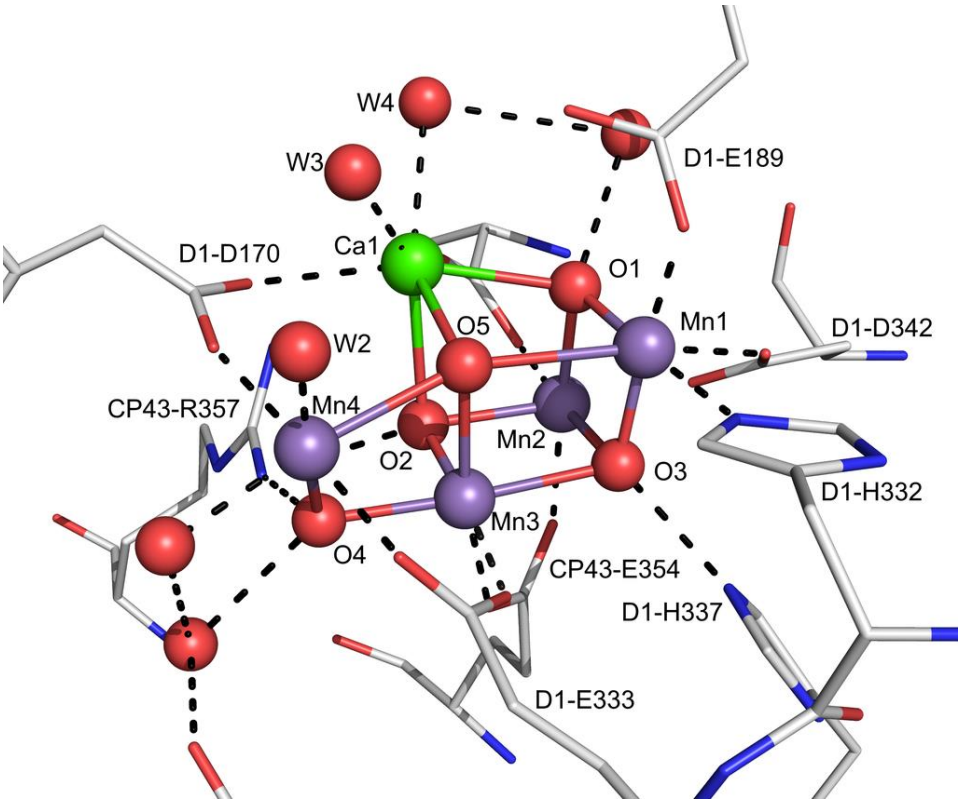

Figure 17: Structure of PSII in 1.9Å resolution. Oxygen, manganese, calcium, nitrogen and carbon are represented by red, purple, green, blue and grey spheres and sticks, respectively. (Taken from [72])

Since nature uses manganese oxide as its solution to drive the OER, research have been conducted to understand the high efficiency of the OEC and to draw inspiration from this system to design active OER electrocatalysts based on manganese oxide.[71,73] The following criteria have been formulated to obtain efficient OER catalysts based on manganese oxide. The inclusion of Mn^{3+} moieties has been demonstrated to be beneficial to the overall OER

activity.[71] Since the presence of Mn^{3+} moieties lower the HOMO-LUMO gap and change the e_g orbital to favorable position to interact with the OER intermediates, synthetic strategies should be geared towards these moieties.[71] Beside this unique design feature for this type catalysts, general design principles such as large surface area, a high number of available active sites, defects and sufficient conductivity are also crucial criteria which must be taken into account.[71]

MnO_x crystallizes in various structures. MnO already exhibits efficient OER activity, specifically with nickel doping.[71,73] Manganese dioxide crystallizes in various crystal structures as shown in Figure 18. In total, six basic structures for manganese dioxide have been found to be stable phases for anode materials.[71,73]

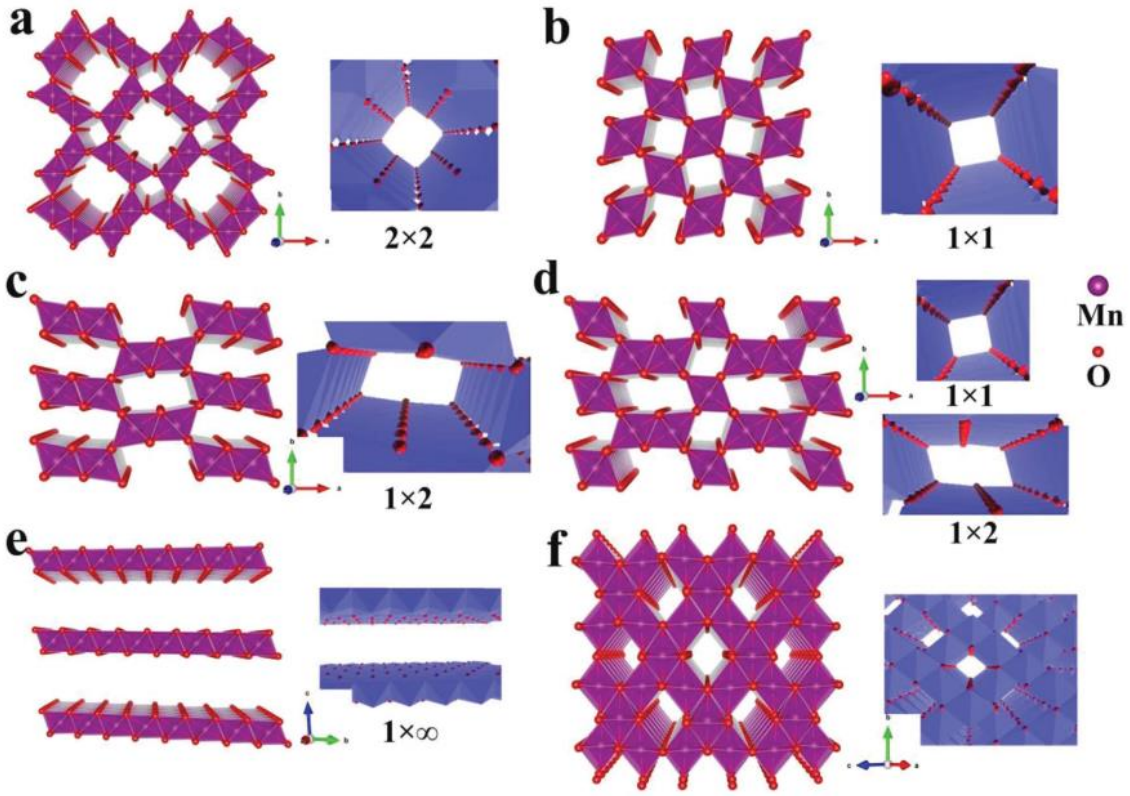

Figure 18: Structure of various manganese dioxides. Manganese is shown as a purple sphere, while oxygen is represented as a red sphere. α-MnO_2, β-MnO_2, γ-MnO_2, ε-MnO_2, δ-MnO_2 and λ-MnO_2 are shown in a), b), c), d), e), and f), respectively. (Taken from [73])

The α-MnO_2 exhibits huge tunnels and comprises of [MnO_6] octahedron double chains which corner-share with adjacent double chains in the plane. The tremendous size of the 1D tunnel in this crystal structure has shown high mass-transport capabilities which facilitate the flow of reactants, products and ions.[73] α-MnO_2 nanowires showed a low overpotential 394mV at 10mA cm^{-2} in 1M KOH as a result of the properties mentioned above.[71] β-MnO_2 features octahedron single chains by vertice-sharing which leads to a reduced size of the 1D tunnel. This crystal structure of manganese dioxide is thermodynamically most favored and therefore is very likely to be present in anodes based on manganese oxide.[71,73] However, studies showed that this type of manganese dioxide is very inactive for the OER. Although significant improvement with regard to the OER

activity is achieved when β-MnO_2 is doped with Ru, it raises the above-mentioned concern of sufficiently accessible Ru deposits to synthesize such catalysts.[71] γ-MnO_2 and ε-MnO_2 have also demonstrated promising properties as OER electrocatalysts since the formation of oxygen vacancies and consequently of Mn^{3+} moieties are facile.[73] A composite of γ-MnO_2 and graphene nanosheets or RuO_2 have shown promising results as dual ORR/OER catalysts as well as a composite made of ε-MnO_2, carbon and Fe_2O_3.[73] δ-MnO_2 is the MnO_2 structure which is the foundation of the manganese oxide nanosheet in our studies as our spectroscopic measurements suggest.[38] Different from the structures shown in Figure 17, δ-MnO_2 is a layered structure which is stabilized by cations between each layer such as potassium.[71] Birnessite is part of this family of manganese dioxides and exists either in a trigonal or tetragonal phase which also contains a mix of Mn^{3+} and Mn^{4+} moieties, making it to an interesting material which has not only been studied in our research. It has also been pointed out that birnessite features structural similarities to the OEC which transforms to a birnessite-like structure upon its agglomeration.[74] If the macrostructure of δ-MnO_2 is flower-like, it has shown outstanding OER activity.[71] Notably, the synergy between carbonaceous support materials such as graphene and δ-MnO_2 has been pointed out in literature since an improvement in conductivity and electrocatalytic performance is found.[71] However, the long-term stability is still an unresolved issue. Both results align with our study on manganese oxide nanosheets on HOPG in which we detect the activity at the interface between the nanosheet and support. Even though the first OER step does not have a thermodynamic barrier, concerns of closing the catalytic cycle are risen in our study.[38] To further improve the OER activity of δ-MnO_2, doping strategies to increase the amount of active Mn^{3+} moieties has been suggested. The modified birnessite $K_xFe[Co_{0.16}Mn_{0.84}O_2]$ shows a low overpotential (375mV at 10mA cm^{-2}) and small Tafel slope (56mV/dec) in 1M KOH.[71] Doping with iridium also leads to catalytic improvement of birnessite, although this strategy is questionable, given the limited deposits of iridium around the globe.[71] Apart from the MnO_2, Mn_2O_3 and Mn_3O_4 have been subject of various research efforts to study their OER performance. Since both oxides are rich in Mn^{3+} moieties and can easily stabilize oxygen vacancies, they have demonstrated remarkable OER activity.[71] Mn_3O_4 nanoparticle, for instance, have been found to have an overpotential of only 395mV at 10mA cm^{-2} at neutral conditions. Other manganese oxides such as MnOOH or even amorphous structures have been investigated in their OER activity.[71]

All in all, manganese oxides are a valuable choice to search for OER catalysts based on Earth-abundant materials. Due to its rich chemistry which offers a large number of different oxides and oxide classes, it offers a big toolbox for material design. Our studies on manganese nanosheets on carbonaceous supports also shed light on various questions such as the location of the active centers and the origin of these results.

Despite the fact that manganese oxide is already a promising OER electrocatalyst, it is also possible to optimize the support material. Beside metallic supports which are still used in heterogeneous catalysis, carbonaceous support materials have been chosen and be improved with regard to their OER activity as well.

3.1.5.3 Carbon-based OER Electrocatalysts

Pristine graphene and graphite have been proven to be inactive for the OER and other electrochemical reactions.[22] Our calculations support this statement and consequently manipulation of the pristine structure is needed to enhance the OER activity.[38] Doping is in this regard a valuable strategy to achieve this obstacle. Two ways of doping these materials

have been proposed. One is utilizing non-metallic elements such as nitrogen or boron, while the other is using metal atoms.

3.1.5.3.1 Metal-free carbon-based OER Electrocatalysts

Although graphene and graphite have demonstrated some OER activity at high overpotentials,[50] other carbon-based materials are better choice than graphene and graphite. The work on N(5)-ethylflavinium ion pioneered the usage of these electrocatalysts as an actual alternative to metal- and metal-oxide-based materials.[75] Though being an inefficient OER catalyst in the end, it could be shown that the electron-withdrawing effect of nitrogen and the ketone group in this ion could activate the neighbouring carbon and enable the adsorption of $^{-}$OH, the starting point of the OER at alkaline conditions.[20,22] Tremendous progress has been made after this discovery. The pre-treatment of carbon clothes and multi-walled nanotubes improved their electrocatalytic OER activity.[20,22] The reported overpotential for the latter system is 360mV at 10mA cm^{-2} in 1M KOH.[20,22] However, electrocatalysts based on pure carbon structures suffer from irreversible oxidation of carbon and degradation of the material. To circumvent this issue and to reduce the overpotential further, doping the structure with nitrogen, sulphur, oxygen, boron and phosphor have been investigated over decades.[20,22] Particularly, the inclusion of nitrogen into the graphene layer has been demonstrated to be beneficial to the electrocatalytic OER properties of carbonaceous catalysts. As it was shown for N(5)-ethylflavinium, the presence of nitrogen facilitates the adsorption of OER intermediates at the neighbouring carbon atom and drives the OER pathway at low overpotentials. Since the long-term stability of these electrocatalysts is also an ongoing issue, the inclusion of metal atoms has been suggested.

3.1.5.3.2 Metal-doped carbon-based OER Electrocatalysts

As discussed above, besides only doping with non-metallic heteroatoms such as nitrogen, the carbonaceous framework could also be doped by metals. It is important to bear in mind in this regard that the metals are preferably accessible with large deposits and affordable when designing such an electrocatalyst. However, it is crucial to bind and to stabilize the metal on the surface since it might leach into the electrolyte otherwise.[20,22] To synthesize such materials, a bottom-up or top-down approach are possible strategies.[76] Generally, a bottom-up strategy employs a precursor to synthesize the actual catalyst. For instance, we use molecular iron phthalocyanine which is carbonized or polymerized by pyrolysis and deposited onto a HOPG substrate. This strategy is simple and can easily be adopted for a wide range of similar precursor materials.[76] Therefore, the large-scale production of electrocatalysts by utilizing this method would be possible. However, careful consideration has to be taken to analyze and to characterize, for instance, the structure and the composition of the product. Top-down approaches, however, offer more control on the structural and atomic composition.[76] The host material is already prepared and provides adsorption sites for the metal which is delivered by other metal complexes. Nevertheless, the formation of cores with higher nuclearity than one can be formed which possibly feature different reactivity due to electronic and structural differences.[76]

Both strategies have been successfully employed to synthesize metal-doped carbonaceous OER electrocatalysts. They are found to have reasonable overpotentials of about 0.3V or 0.4V vs RHE at 20mA cm^{-2} in 1M NaOH.[20] The carbonized iron phthalocyanine, in which KOH instead of NaOH is used, has a similar overpotential as other metal-doped carbon-based electrocatalysts. In our study, we managed to visualize the OER activity of CFePc by

n-EC-STM which showed an image with isolated noise. We attribute this feature to the spatially isolated metal centers which drive OER at reasonable overpotentials. This result agrees with our DFT calculations which were initially tested and benchmarked, revealing a method dependency on the obtained prediction of the OER overpotential. Expanding our study, we combine CFePc with manganese oxide nanosheets and assign the enhanced OER activity to the interface between nanosheets and substrate.

3.2 The Nitrogen Oxidation Reaction

3.2.1 The Conventional Way of Nitrogen Oxidation

Nitrate (NO_3^-) is a crucial component of fertilizers and important for the formation of amino acids, nucleic acids and chlorophyll in plants.[77,78] However, prior to the absorption of nitrate by the plants, atmospheric nitrogen must be converted into nitrate. This process is divided into two steps. Firstly, nitrogen is fixated by bacteria in the soil which contain the nitrogenase enzyme. This enzyme reduces the atmospheric nitrogen to ammonia NH_3, following (47).[77,78]

$$N_2 + 8(H^+ + e^-) \rightarrow 2NH_3 + H_2 \quad (47)$$

However, ammonia is not bioavailable for most plant and bacteria and it is therefore oxidized to nitrate, involving two types of bacteria in the soil.[77,78]

$$NH_3 + O_2 + H_2O \rightarrow NO_3^- + 5(H^+ + e^-) \quad (48)$$

The nitrogen cycle in Figure 19a summarizes the sequence of chemical reactions which are involved in the redox reactions of nitrogen. After the initial reduction to ammonia and subsequent oxidation to nitrate via hydroxylamine and nitrite, the nitrate is reduced back stepwise to nitrogen which can then be fixated again.[78]

Basically, the same process occurs in industry to produce nitrate. The Haber-Bosch process reduces the atmospheric nitrogen to ammonia as shown in (49).[77]

$$N_2 + 3H_2 \rightarrow 2NH_3 \quad (49)$$

The produced ammonia is oxidized by the Ostwald process in which the ammonia is firstly oxidized to nitric oxide. The nitric oxide reacts further via nitrite to nitrate.[77]

$$4NH_3 + 5O_2 \rightarrow 4NO + 6H_2O \quad (50)$$

$$2NO + O_2 \rightarrow 2NO_2 \quad (51)$$

$$3NO_2 + H_2O \rightarrow 2HNO_3 + NO \quad (52)$$

Figure 19b shows the equilibrium potentials of each involved reaction. It becomes clear that the sequence of Nitrogen Reduction Reaction (NRR) and oxidation of ammonia is energetically less demanding than the direct oxidation of nitrogen.[79] Therefore, it is clear by considering this fact that nature has chosen a two-step process to produce nitrate from atmospheric nitrogen.

a)

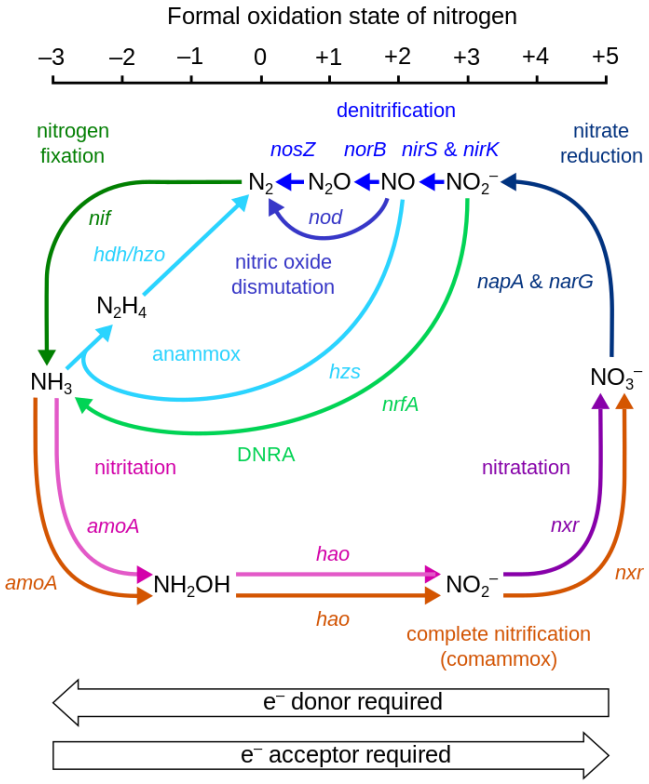

b)

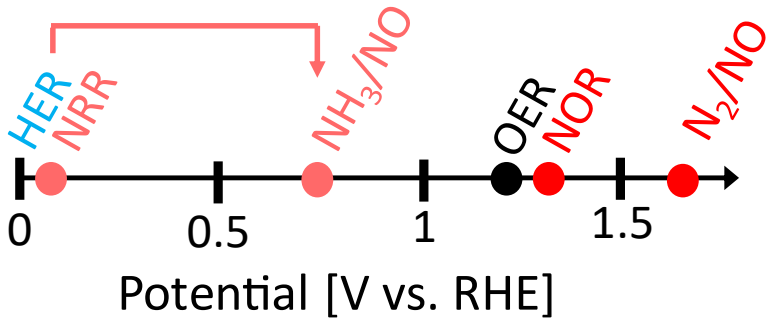

Figure 19: a) Natural nitrogen cycle with consideration of the oxidation state of nitrogen since nitrogen is first reduced and then oxidized to from nitrate. b) Equilibrium potentials HER, Nitrogen Reduction Reaction (NRR), ammonia oxidation, OER, Nitrogen Oxidation Reaction and nitrogen oxidation to NO. (a) taken from [80])

However, even if the combination of Haber-Bosch and Ostwald process imitates nature's solution, it is harmful to the climate and environment. The Haber-Bosch process accounts for 2% of the global energy consumption and 1% of the CO_2 emissions worldwide.[81] Therefore, research efforts have been put into finding alternatives for the Haber-Bosch process such as electrochemical processes.[17,82–88] Nevertheless, an environmentally friendly way to oxidize the ammonia produced by the NRR must be found. The Ostwald process, which could be used here, also produces 2.4 tons of CO_2 per ton nitrate.[89] Consequently, the entire way of producing nitrate must be revised. In this work, we also investigated the electrochemical Nitrogen Oxidation Reaction (NOR) as an alternative approach for nitrate production.[32]

3.2.2 The Direct Nitrogen Oxidation Reaction

The direct oxidation of nitrogen towards nitrate also occurs in nature and has been subject of research in the past. When lightning happens, the energy released during this event suffices to cleave the triple bond of nitrogen and following a complex reaction network, the atmospheric nitrogen gets oxidized towards nitrate and directly fixated.[90] Inspired by this process, Birkeland and Eyde proposed a process in 1903 in which an electrical arc oxidizes the atmospheric nitrogen in presence of oxygen.[91]

$$\mathrm{N}_2 + O_2 \rightarrow 2\mathrm{NO} \tag{53}$$

The second step of this process in which nitrous oxide reacts further towards nitrate is rather facile.

$$2NO + O_2 \rightarrow 2NO_2 \tag{54}$$

$$3NO_2 + H_2O \rightarrow 2HNO_3 + NO \tag{55}$$

However, beside the electrical arc, temperatures of 3000°C are also needed, giving an overall yield between 4% and 5%.[91,92] Since the demand for nitrate is high, an efficient process with appropriate yields is needed, and the excessive consumption of energy for this process is also problematic. Despite these challenges, the NOR has been reconsidered in photo- and electrochemistry since an efficient NOR electrocatalyst could not only replace the Haber-Bosch process but also the Ostwald process. Several experimental and theoretical studies have been published in the past years in which various electrocatalysts were investigated. Spinel structures and composite materials, for instance, were part of these works.[93–99] The theoretical studies mostly attempted to find a proper descriptor and to screen through the composition space of catalysts to find an efficient material.[100–102]

In contrast to these research works, we focus on understanding the NOR on a rutile-typed TiO_2(110) electrode holistically. Our approach not only took the electronic structure of the electrode and the reactants into account but also the effect of applied potential by employing Grand-Canonical DFT calculations and interfacial effects between the electrode and water.[32] Our study accounts for the competing OER and considers the mechanisms as described in Figure 20.[32]

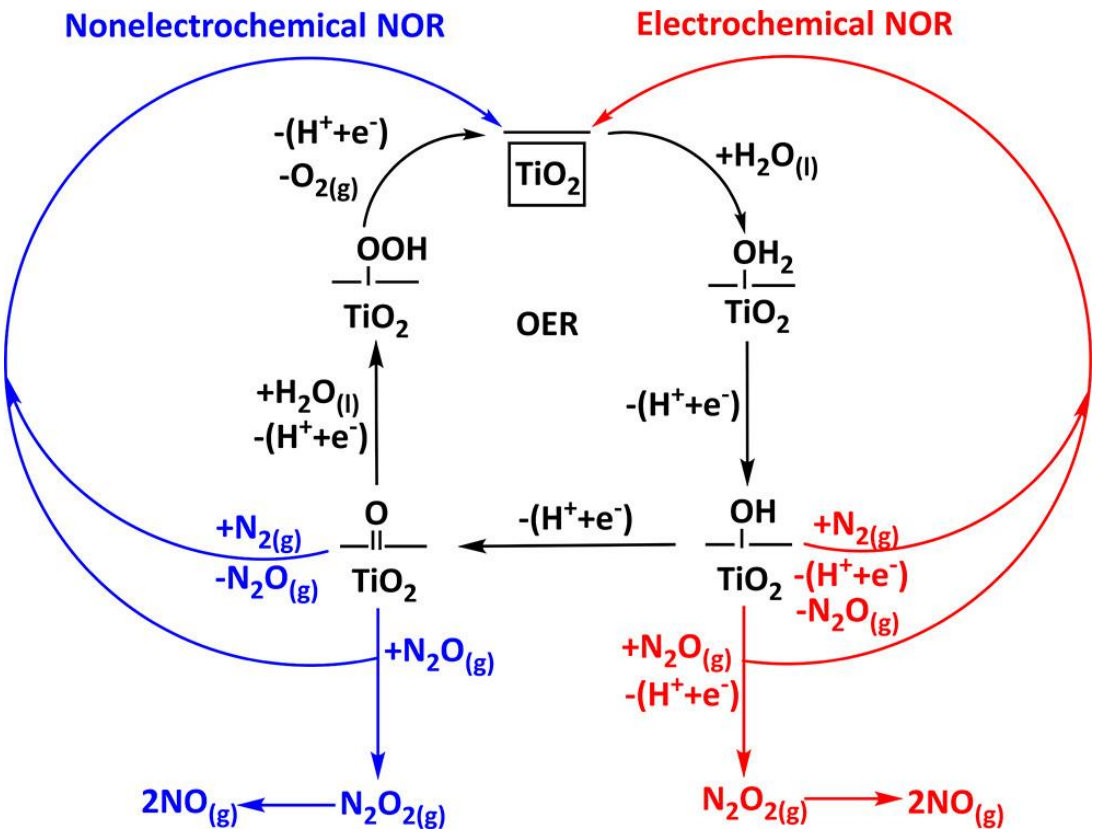

Figure 20: Possible mechanism for OER (black), the electrochemical NOR (red) and nonelectrochemical NOR (blue). (Taken from [32])

Since the first NOR steps which include the formation of N_2O and N_2O_2 are the most challenging, while the following steps towards nitrate are rather facile (see Birkeland-Eyde and Ostwald process), we only take these steps into account.[32] We find a very close competition between the OER and the nonelectrochemical NOR. N_2 and all other NOR intermediates get oxidized by the *O intermediate which could also proceed in the OER pathway to form *OOH. We identify the availability of nitrogen and the presence of water at the electrode as the factors which determine whether the NOR or OER takes place.[32] Note that the mechanism of the NOR is still a subject which is debated in literature. Some studies suggest the formation of $*N_2OH$ as the first NOR intermediate.[103] However, it is yet questionable if such pathways take place since the energetic barrier to form this intermediate are high and it has never been observed in surface science and surface chemistry.[100] Nevertheless, our work shed light on various questions and clarifies the importance of interfacial effects on the competition between OER and NOR.

4 Introduction to theoretical background

4.1 The Schrödinger equation

The foundation of modern quantum mechanics is the Schrödinger equation which shed light on many questions such as the black body problem or the electronic structure of atoms and molecules. As proposed by Erwin Schrödinger in 1926, the time-dependent Schrödinger equation in given in (56).[19,104]

$$i\hbar\frac{\partial}{\partial t}\Psi(r_{all},t) = \hat{H}\Psi(r_{all},t), \tag{56}$$

with $i\hbar\frac{\partial}{\partial t}$ as the time-evolution operator, $\Psi(r_{all},t)$ as the time-dependent electronic wave function containing the electronic and nuclear coordinates and $\hat{H}$ as the Hamiltonian. If the $\hat{H}$ is constant, the time-dependence can be separated from (x) and the wave function is expressed as the temporal evolution of the steady-state wave function $\Psi(r_{all},0)$ in (57)[19,105]

$$\Psi(r_{all},t) = e^{-\frac{iEt}{\hbar}}\Psi(r_{all},0), \tag{57}$$

with E as the energy eigenvalue. This assumption also leads to the time-independent Schrödinger equation (58) in which the stationary eigenfunctions and energy eigenvalues of the system in question are obtained.[19,105]

$$\hat{H}\Psi(r_{all},0) = E\Psi(r_{all},0) \tag{58}$$

$\hat{H}$ decomposes into

$$\hat{H} = \hat{T}_e + \hat{T}_n + \hat{V}_{ne} + \hat{V}_{nn} + \hat{V}_{ee} \tag{59}$$

with $\hat{T}_e$ and $\hat{T}_n$ are the kinetic energy operators of the electron and nuclei motion as defined in (60) and (61), respectively, and $\hat{V}_{ne}$, $\hat{V}_{nn}$ and $\hat{V}_{ee}$ are the potential energy operators of the electron-nucleus attraction, nucleus-nucleus repulsion and electron-electron repulsion for a system with N electrons and M protons:[19,105]

$$\hat{T}_e = -\frac{1}{2}\sum_{i}^{N}\frac{\nabla^2}{m_{e,i}} \tag{60}$$

$$\hat{T}_n = -\frac{1}{2}\sum_{j}^{M}\frac{\nabla^2}{M_{p,k}} \tag{61}$$

$$\hat{V}_{ne} = -\sum_{i=1}^{N}\sum_{k=1}^{M}\frac{e^2 Z_k}{|r_i - R_k|} \tag{62}$$

$$\hat{V}_{nn} = \sum_{k=1}^{M}\sum_{l>1}^{M}\frac{e^2 Z_k Z_l}{|R_k - R_l|} \tag{63}$$

$$\hat{V}_{ee} = \sum_{i=1}^{N}\sum_{j>1}^{N}\frac{e^2}{|r_i - r_j|} \tag{64}$$

with $\vec{\nabla} = \left(\frac{\partial}{\partial x} \quad \frac{\partial}{\partial y} \quad \frac{\partial}{\partial z}\right)^T$ the Nabla operator, m_e the electron mass, M_p the proton mass, e the elementary charge, Z the atomic number, r and R as the distances between the electrons i and j and nuclei k and l, respectively. Since the Schrödinger equation is a partial differential equation with 3N degrees of freedom, finding an analytical solution is impossible. Therefore, in order to reduce the complexity of this equation, the Born-Oppenheimer approximation is introduced.[19,105]

4.2 The Born-Oppenheimer approximation

The Born-Oppenheimer approximation assumes that an electron instantaneously follows the motion of nuclei as a nucleus is about 2000 times heavier than an electron. This adiabatic approach allows to express the electronic wave function as a product of two functions (65)[19,105,106]

$$\Psi(r,R) = \Psi_n(R)\Psi_e(r,R) \tag{65}$$

where $\Psi(r,R)$ is the time-independent wave function dependent on electronic and nuclear coordinates r and R, while $\Psi_n(R)$ and $\Psi_e(r,R)$ are the nuclear and the electronic wave function, respectively. The latter parametrically depends on the nuclear positions. Assuming that the action of the nuclear kinetic energy operator $\hat{T}_n$ in the electronic Hamiltonian $\hat{H}_e$ on $\Psi_e(r,R)$ can be neglected, i.e. vibronic couplings are negligible, the electronic Schrödinger equation (66) is solved for a given set of nuclear coordinates.[106] The obtained electronic energy eigenvalues E_e of (50) are added to the Hamiltonian $\hat{H}_n$ of the nuclear Schrödinger equation (67).[106]

$$\hat{H}_e\Psi_e(r,R) = \left[\hat{T}_e + \hat{V}_{ne} + \hat{V}_{ee}\right]\Psi_e(r,R) = E_e\Psi_e(r,R) \tag{66}$$

$$\hat{H}_n\Psi_n(R) = \left[\hat{T}_n + \hat{V}_{nn} + E_e\right]\Psi_n(R) = E_{tot}\Psi_n(R) \tag{67}$$

The latter Schrödinger equation yields the total energy E_{tot} of the system as its eigenvalue. Despite the simplifications of the Schrödinger equations which are achieved here, further effort has to be taken to reduce the mathematical complexity of these set of equations.

4.3 The Hartree-Fock Theory

As the Schrödinger equations (66) and (67) are still a many-body problem in which $\hat{V}_{ee}$ contains the electron-electron interactions, a simple separation similar to transitioning from the time-dependent to the time-independent Schrödinger equation is impossible. Consequently, further approximations are necessary to be able to solve the Schrödinger equation. Herein, the total electronic ground state wave function $\Psi_{0,e}(r,R)$ is approximated by a set of single-electron spin-orbitals $\theta_s(N)$ in a Slater determinant (68).[107]

$$\Psi_{0,e}(r,R) = \frac{1}{\sqrt{N!}} \begin{vmatrix} \theta_\alpha(1) & \theta_\beta(1) & \cdots & \theta_s(1) \\ \theta_\alpha(2) & \theta_\beta(2) & \cdots & \theta_s(2) \\ \vdots & \vdots & \ddots & \vdots \\ \theta_\alpha(N) & \theta_\beta(N) & \cdots & \theta_s(N) \end{vmatrix}, \tag{68}$$

with subscript s = α, β as spin channel and N as the number of electron(s). Such a formulation satisfies the antisymmetric nature of a fermion wave function and the Pauli exclusion principle. In order to address the electron-electron interactions, $\hat{V}_{ee}$ resembles to an effective potential $\hat{V}_{HF}$ which screens a single electron and consists of a mean field generated by the other electrons.[108,109] With this approximations, the electronic Hamiltonian decomposes into a set of single-electron Hamiltonians.[108,109]

$$\hat{H}_e \approx \sum_{i=1}^{N} \hat{h}(i) + \hat{V}_{HF}(i), \tag{69}$$

with

$$\hat{h}(i) = -\frac{1}{2}\frac{\nabla^2}{m_{e,i}} - \sum_{k=1}^{M} \frac{Z_k}{|r_i - R_k|} \tag{70}$$

where the first term is the kinetic energy of an electron i and the second term is the interaction of this electron with the nuclei. The effectively repulsive potential in $\hat{V}_{HF}(i)$ is given by (71).[108,109]

$$\hat{V}_{HF}(\vec{x}_1) = \sum_{i}^{N} \left(\hat{J}_i(\vec{x}_1) - \hat{K}_i(\vec{x}_1) \right) \tag{71}$$

$\vec{x}_1$s the position of the electron, $\hat{J}_i$ is the Coulomb integral, and $\hat{K}_i$ is the exchange integral given by (72) and (73): [108,109]

$$\hat{J}_i(\vec{x}_1)\theta_i(\vec{x}_1) = \int d\vec{x}_2 \theta_j^*(\vec{x}_2) \frac{1}{r_{12}} \theta_j(\vec{x}_2)\theta_i(\vec{x}_1) \tag{72}$$

$$\hat{K}_i(\vec{x}_1)\theta_i(\vec{x}_1) = \int d\vec{x}_2 \theta_j^*(\vec{x}_2) \frac{1}{r_{12}} \theta_i(\vec{x}_2)\theta_j(\vec{x}_1) \tag{73}$$

We realise from (72) and (73) that this eigenvalue problem initially depends on the spin-orbital functions $\theta_s(N)$. Consequently, this function is subject of an initial guess and is then minimised in a self-consistent cycle until a set convergence threshold is satisfied.[108,109]

As the Hartree-Fock approximation neglects correlation effects of the electrons, particularly the electron-electron interactions, which is replaced by a mean field, the obtained total energies are overestimated.[19] The reason here is that the mean field overestimates the electron repulsion. To correct for these correlation effects, several methods such as Coupled Cluster, multideterminant approaches and Density Functional Theory have been developed.[110,111]

4.4 Density Functional Theory (DFT)

Apart from commonly used quantum chemical approaches like Hartree-Fock or Møller-Plesset theory, density functional theory (DFT) became important for modelling especially systems with many atoms. Basically, the general idea is given by the Hohenberg-Kohn theorem which states that the ground state energy E_0 of any system is a functional of the ground state electron density ρ_0. Finding an electron density ρ which minimizes the energy E of the system yields E_0 in the end.[110,111]

$$\min_{\rho} E[\rho] = E_0 \tag{74}$$

The functional $E_0[\rho_0]$ can be divided up into the three functionals: the mean kinetic energy $\bar{T}[\rho_0]$, the mean potential energy of electron-electron repulsion $\overline{V}_{ee}[\rho_0]$ and the mean potential energy of the core-electron attraction $\overline{V}_{ne}[\rho_0]$.[110,111]

$$E_0[\rho_0] = \bar{T}[\rho_0] + \overline{V}_{ee}[\rho_0] + \overline{V}_{ne}[\rho_0] \tag{75}$$

$\overline{V}_{ne}[\rho_0]$ is system-dependent and known (given in (76)) whereas both $\overline{T}[\rho_0]$ and $\overline{V}_{ee}[\rho_0]$ are universal but unknown.[110,111]

$$\overline{V}_{ne}[\rho_0] = \int \rho_0(\vec{r}) v(\vec{r}) d\vec{r} \tag{76}$$

$v(\vec{r})$ is the external potential, generated by the protons. Since many expressions are missing in (75), the Hohenberg-Kohn variation principle and the Kohn-Sham method were used to derive the ground state electron density ρ_0.[111] Using the Hohenberg-Kohn variation principle, an electron density ρ_{tr} is estimated as an initial guess which cannot generate an energy lower than E_0.[111] In order to find ρ_0, the Kohn-Sham method is used which schedules a reference system with N non-interacting electrons (variables with regard to this system have a "s" in the index). The electrons inside this system are exposed to an external potential $v_s(\vec{r}_z)$, generated by the protons. $v_s(\vec{r}_z)$ has to be optimized in a way that the electron density at r converges to ρ_0. Now, a Hamiltonian (77), including these estimations, can be formulated.[110,111]

$$\hat{H}_s = \sum_{z=1}^{n}[-\frac{1}{2}\Delta_z + v_s(\vec{r}_z)] = \sum_{z=1}^{n}[\hat{h}_{KS,z}] \tag{77}$$

where

$$\hat{h}_{KS,z} = -\frac{1}{2}\Delta_z + v_s(\vec{r}_z) \tag{78}$$

The Kohn-Sham equations (79) are set up and solved iteratively.[111]

$$\hat{h}_{KS,z}\theta_{KS} = \varepsilon_{KS,z}\theta_{KS} \tag{79}$$

where $\theta_{KS,z}$ are the Kohn-Sham orbitals and $\varepsilon_{KS,z}$ the Kohn-Sham energies as eigenvalues of this equation. In this thesis, plane waves with pseudopotentials were used to model the $\theta_{KS,z}$. (81) yields the electron density using the converged θ_{KS}.[111]

$$\rho_0 = \rho_s = \sum_{z=1}^{n} |\theta_{KS}|^2 \tag{80}$$

In order to find expressions for $\overline{\mathrm{T}}[\rho_0]$ and $\overline{\mathrm{V}}_{ee}[\rho_0]$, the Kohn-Sham method is used. The functionals $\overline{\mathrm{T}}_s[\rho_0]$ and $\overline{\mathrm{V}}_{ee,s}[\rho_0]$ with regard to the reference system are set up and the difference between $\bar{T}[\rho_0]$ and $\overline{\mathrm{V}}_{ee}[\rho_0]$ are derived, given in (81) and (82).[110,111]

$$\Delta\overline{\mathrm{T}}[\rho_0] = \overline{\mathrm{T}}[\rho_0] - \overline{\mathrm{T}}_s[\rho_0] \tag{81}$$

$$\Delta\bar{V}_{ee}[\rho_0] = \bar{V}_{ee}[\rho_0] - \bar{V}_{ee,s}[\rho_0] \tag{82}$$

Since $\bar{T}_s[\rho_0]$ and $\overline{\mathrm{V}}_{ee,s}[\rho_0]$ do not include electron-electron interactions, their solution is trivial and given; $\overline{\mathrm{V}}_{ee,s}[\rho_0]$ is the classical Coulomb repulsion. When (81) and (82) are changed to $\bar{T}[\rho_0]$ and $\overline{\mathrm{V}}_{ee}[\rho_0]$, respectively, they are substituted in (75), yielding (83).[111,112]

$$E_0[\rho_0] = \int \rho_0(\vec{r})v(\vec{r})d\vec{r} + \overline{\mathrm{T}}_s[\rho_0] + \frac{1}{2}\iint \frac{\rho_0(\vec{r}_1)\rho_0(\vec{r}_2)}{r_{12}} d\,\vec{r}_1 d\vec{r}_2 + \Delta\overline{\mathrm{T}}[\rho_0] + \Delta\bar{V}_{ee}[\rho_0] \tag{83}$$

Both $\Delta\overline{\mathrm{T}}[\rho_0]$ and $\Delta\overline{\mathrm{V}}_{ee}[\rho_0]$ are the exchange-correlation functional $E_{xc}[\rho_0]$ which can be estimated in so far four different ways (from low to higher chemical accuracy, also shown in Figure 21):

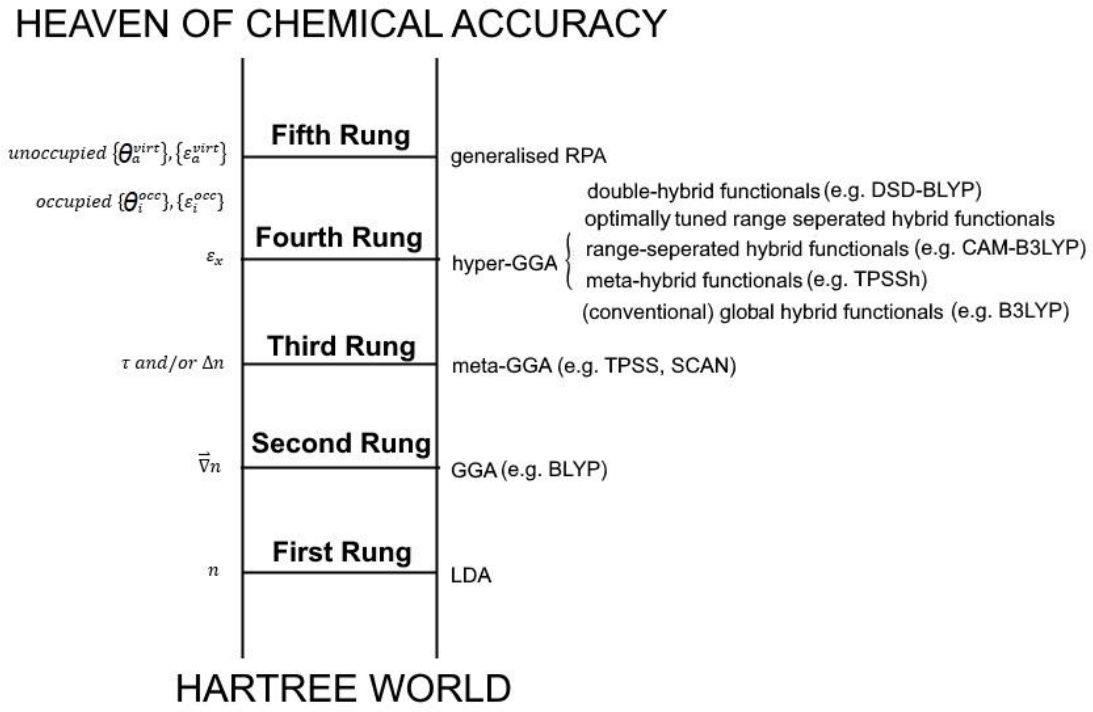

Figure 21: Jacob's ladder of DFT with all different levels of accuracy.

- LDA (Local Density Approximation): The electron density is assumed as a uniform electron gas. No gradient is included.[113]

$$E_{xc}^{L(S)DA}[n_\uparrow, n_\downarrow] = \int d^3r n\varepsilon_{xc}^{unif}(n_\uparrow, n_\downarrow)$$
$$\text{with } \varepsilon_{xc}^{unif}(n_\uparrow, n_\downarrow) = -\frac{3}{4}\left(\frac{3}{\pi}n\right)^{\frac{1}{3}} + \varepsilon_c^{VWN} \tag{84}$$

- GGA (Generalized Gradient Approximation): A gradient for the electron density is included, using its first derivative.[114,115]

$$E_{xc}^{GGA}[n_\uparrow, n_\downarrow] = \int d^3r n\varepsilon_{xc}^{GGA}\left(n_\uparrow, n_\downarrow, \vec{\nabla} n_\uparrow, \vec{\nabla} n_\downarrow\right) \tag{85}$$

- The chosen functional PBE is an example for a GGA functional. The exchange and the correlation functional $E_{x,PBE}$ and $E_{c,PBE}$ are given by (86) and (87), respectively.[114,115]

$$E_{x,PBE} = E_{x,LDA}F(x) \tag{86}$$

$$E_{c,PBE} = E_{c,LDA} + H(t) \tag{87}$$

where *x* and *t* are:[114,115]

$$x = \frac{|\nabla\rho|}{\rho^{\frac{4}{3}}} \tag{88}$$

$$t = \frac{1}{\sqrt{6\pi^3 f_3}} x \tag{89}$$

- m-GGA (meta-GGA): In the exchange-correlation functional, higher order derivatives of the electron density are included.[116]

$$E_{xc}^{meta-GGA}[n_\uparrow, n_\downarrow] = \int d^3r n\varepsilon_{xc}^{meta-GGA}\left(n_\uparrow, n_\downarrow, \vec{\nabla}n_\uparrow, \vec{\nabla}n_\downarrow, \Delta n_\uparrow, \Delta n_\downarrow, \tau_\uparrow, \tau_\downarrow\right) \quad \text{with } \tau_\sigma = \frac{1}{2}\sum_i^{occ.}\left|\vec{\nabla}\theta_{KS,i\sigma}\right|^2 \tag{90}$$

- h-GGA (hyper- or hybrid-GGA): The exact exchange term of Hartree-Fock is included and additionally, the occupied θ_{KS} are included as variables. Examples for such functionals are B3LYP or HSE.[117]

$$\varepsilon_{x\sigma}(r) = -\frac{1}{2n_\sigma(r)}\int d^3r' \frac{\left|\sum_i^{occ}\theta^*{}_{KS,i\sigma}(r)\theta_{KS,i\sigma}(r')\right|^2}{|r-r'|} \tag{91}$$

The exact exchange density is now included into the exchange-correlation functional of hybrid DFT methods or hyper-GGA $E_{xc}^{hyper-GGA}[n_\uparrow, n_\downarrow]$ (92).[117]

$$E_{xc}^{hyper-GGA}[n_\uparrow, n_\downarrow] = \int d^3r n\varepsilon_{xc}^{hyper-GGA}\left(n_\uparrow, n_\downarrow, \vec{\nabla}n_\uparrow, \vec{\nabla}n_\downarrow, \Delta n_\uparrow, \Delta n_\downarrow, \tau_\uparrow, \tau_\downarrow, \varepsilon_{x\uparrow}, \varepsilon_{x\downarrow}\right) \tag{92}$$

- Including all information of the θ_{KS} are methods which are still under developement.[118]

Beside these approaches which add more terms and complexity to the exchange-correlation functional and correct for errors which occur at lower level of theories, some empirical and *a posteriori* correction schemes also exist. For instance, conventional DFT functionals (except for double hybrids) do not account for long-range correlation effects such dispersion and various correlations have been formulated to include this effect into DFT calculations.[119–123] These approaches are being discussed in Chapter 4.6. Another drawback of DFT is the so-called self-interaction error (SIE) which arises from the Coulomb term in (84) and erroneously counts in interactions of electrons with themselves. As a consequence of this self-repulsion, electrons are overdelocalized in space which leads to, for instance, the underestimation of band gaps in semiconductors or insulators.[124,125] In principle, the inclusion of Hartree-Fock exchange (92) could counteract the Coulomb term in (84) or the self-interaction error correction (SIC) as formulated by Perdew and Zunger in could correct for this error.[117,126] These approaches are, however, computationally very demanding and not applicable to every model system which requires a certain size, for

example, to capture the complexity to be modelled. Therefore, the DFT+U_{Hub} approach has been developed which was inspired by the Hubbard impurity model and is being explained in the following chapter 4.5.[127]

4.5 The Hubbard U_{Hub} correction

The Hubbard U_{Hub} correction is derived from the Hubbard model which generates an "on-site repulsion" on electrons at the same atom. The original theory addresses the flaws of band theory, which predicted some experimentally found insulators to be conducting metals.[128] Herein, two competing contributions are relevant to correctly determine the electronic character of a material: On one hand, the hopping amplitude t determines whether an electron changes from one atom to another. On the other hand, the on-site Coulomb interactions U_{Hub} prevents the electron hopping, but ensures that electrons "stay" in their designated states.[128] The Hubbard Hamiltonian $\hat{H}_{Hub}$ is formulated in (93).[128]

$$\hat{H}_{Hub} = -t \sum_{ij} \sum_{\sigma} \hat{c}_{i\sigma}^{+} \hat{c}_{j\sigma} + U_{Hub} \sum_{i} \hat{n}_{i,\alpha} \hat{n}_{i,\beta} \quad \text{with } \hat{n}_{i,\sigma} = \hat{c}_{i\sigma}^{+} \hat{c}_{i\sigma} \tag{93}$$

Therefore, this Hamiltonian describes the interactions between the atomic sites i and j. The first term is the hopping probability between site i to j where the corresponding electronic states with spin σ are created or annihilated by the operators $\hat{c}_{i\sigma}^{+}$ and $\hat{c}_{i\sigma}$, respectively. The second term quantifies the repulsion of site. If $t << U_{Hub}$, an insulator is obtained.[128] Inspired by this approach, several DFT+U_{Hub} corrections have been formulated. Lichtenstein et al. pioneered with their rotationally invariant formulation, while a simplified variant has been formulated by Dudarev et al.[127,129] The latter is used in this thesis, whose model Hamiltonian is given by (95).[127]

$$\hat{H}_{DFT-Hub} = \frac{\bar{U}_{Hub}}{2} \sum_{m,m'} \sum_{\sigma} \hat{n}_{m,\sigma} \hat{n}_{m',-\sigma} + \frac{\bar{U}_{Hub} - \bar{J}_{Hub}}{2} \sum_{m \neq m'} \sum_{\sigma} \hat{n}_{m,\sigma} \hat{n}_{m',\sigma} \quad \text{with } \hat{n}_{\sigma} = \hat{c}_{\sigma}^{+} \hat{c}_{\sigma} \tag{94}$$

m and m' denote the orbital momentum, $\bar{U}_{Hub}$ and $\bar{J}_{Hub}$ are spherically averaged matrix elements of the screened electron-electron interaction. Note that $\bar{J}_{Hub}$ represents an exchange parameter in Lichtenstein's formulation, while only $\bar{U}_{Hub}$-$\bar{J}_{Hub}$ are meaningful in Dudarev's approach. The DFT+U_{Hub} functional is then obtained.[127,129]

$$E_{DFT+U_{Hub}} = E_{DFT} + \frac{\bar{U}_{Hub} - \bar{J}_{Hub}}{2} \sum_{\sigma} \left[\left(\sum_{j} \rho_{jj}^{\sigma} \right) - \left(\sum_{j,l} \rho_{jl}^{\sigma} \rho_{lj}^{\sigma} \right) \right] \tag{95}$$

ρ_{jl}^{σ} is the density matrix of correlated electrons such as *d* (as originally proposed in Dudarev's paper) or *f* electrons. The second term in the DFT+U_{Hub} functional adds a repulsive on-site term which forces the occupation of each energy to be either 0 or 1.[127]

4.6 Dispersion correction methods

Even though DFT can simulate electronic properties of many systems successfully and in acceptable computational time, the simulation of dispersion interactions like van der Waals interactions was challenging for a long time. Nevertheless, dispersion interactions play a key role in many chemical systems. The issue not to be able to consider dispersion in the electronic structure of the systems is not an issue inherent to DFT. According to the Hohenberg-Kohn theorem,[110,111] all ground state properties of all systems are available if the exact functional of the ground state electron density is known. So, the wrong description of dispersion resulted from the approximated exchange-correlation functionals. The main challenge for these functionals is to correctly model the asymptotic $\frac{1}{r^6}$ behaviour of dispersion interactions. To overcome these problems, several approaches were developed. These approaches can be divided up into four main categories:

1. Semi-empirical and pairwise approaches for dispersion like DFT-D2.[121]

2. Approaches which on top take environmental dependency of dispersion into account like DFT-D3 or Tkatchenko-Scheffler.[119,120]

3. Approaches which model dispersion based on appropriate functionals like in vdW-DF or BEEF.[130,131]

4. Approaches which also consider dispersion interactions beyond pairwise interactions like many-body dispersion or random-phase approximation.[122]

In this thesis, DFT-D2,[121] DFT-D3,[132] Tkatchenko-Scheffler (TS),[123] Tkatchenko's Many-Body Dispersion (MBD),[122] the Bayesian error estimation functional (BEEF)-vdW[130] and the revised Vydrov and van Voorhis (rVV10)[133] functional were used to model dispersion and will be described in detail in the following.

4.6.1 DFT-D2

The general approach of Grimme's DFT-D2 is described in (96):[121]

$$E_{DFT-D2} = E_{DFT-KS} + E_{disp} \tag{96}$$

E_{DFT-D2} is the total energy obtained from the simulation, including dispersion, E_{DFT-KS} is the energy obtained only from the chosen functional and E_{disp} is the contribution of dispersion to E_{DFT-D2}. $E_{disp,DFT-D2}$ is defined according to (97):[121]

$$E_{disp,DFT-D2} = -\frac{1}{2} s_6 \sum_{i \neq j} \frac{C_{6,ij,DFT-D2}}{r_{ij}^6} f_{d,DFT-D2}(r_{ij}) \tag{97}$$

where $C_{6,ij,DFT-D2}$ is the dispersion coefficient for the atom pair ij, s_6 is a global scaling factor, depending on the chosen functional (for the chosen functional PBE the value is 0.75), and r_{ij} is the interatomic distance between atoms i and j.[121] The purpose of the damping function $f_{d,DFT-D2}(r_{ij})$ is to avoid double-counting for small r which is defined as

$$f_{d,DFT-D2}(r_{ij}) = \frac{1}{1 + e^{-d(\frac{r_{ij}}{r_{ij,o,DFT-D2}} - 1)}} \tag{98}$$

where d is a damping factor which is set at 20.0 and $r_{ij,0,DFT-D2}$ is the sum of atomic van der Waals radii $r_{i,0,DFT-D2}$ and $r_{j,0,DFT-D2}$ for the elements i and j. The dispersion coefficient $C_{6,ij,DFT-D2}$ is derived by the expression (99):[121]

$$C_{6,ij,DFT-D2} = \sqrt{C_{6,i,DFT-D2} C_{6,j,DFT-D2}} \tag{99}$$

where $C_{6,i,DFT-D2}$ and $C_{6,j,DFT-D2}$ are tabulated, element specific dispersion coefficients for the elements i and j, respectively. As it can be seen, for this kind of correction some parameters needs to be implemented.[121] Here, values for $C_{6,DFT-D2}$, $r_{0,DFT-D2}$, s_6 and d have to be found. For periodic systems, additionally, a value R_{cut} has to be defined which is a cutoff distance to truncate direct lattice summation.[121] Here, a value of 50.0 Å for R_{cut} was chosen. Note that DFT-D2 is only parameterized for the first five rows of the periodic table and further advances in this regard were needed.[121]

4.6.2 DFT-D3

Following the general idea of DFT-D2, DFT-D3 improves the dispersion correction by implementing a geometrically dependent $C_{6,ij,DFT-D3}$ factor. There are three variants of DFT-D3 which, in general, differ with regard to the damping function $f_d(r_{i,j})$: DFT-D3(zero),[120] DFT-D3(BJ)[134] and DFT-D3(CSO).[135] The first mentioned method was used in this thesis. On top, so called three-body effects can be taken into account by this method to consider contributions of dispersion which go beyond the pairwise interactions between atoms. Indeed, this latter approach was not used in this thesis since it is not implemented in VASP.

In general, the dispersion energy contribution of DFT-D3(zero) $E_{disp,DFT-D3(zero)}$ is given by (100):[120]

$$E_{disp,DFT-D3(zero)} = -\frac{1}{2} \sum_{i \neq j} \sum_{n=6,8} s_n \frac{C_{n,ij,DFT-D3}}{r_{ij}^n} f_{d,n,DFT-D3(zero)}(r_{ij}) \tag{100}$$

where s_n are again scaling factors, depending on the used functional, $C_{n,ij,DFT-D3}$ are environmental dependent dispersion coefficients, r_{ij} are the interatomic distances between the atoms i and j and $f_{d,n,DFT-D3(zero)}(r_{ij})$ are the corresponding damping functions.[120] While for n=6 the dispersion energy of DFT-D2 is again obtained, for n=8 a higher-ordered dispersion coefficient $C_{8,DFT-D3}$ is taken into account. So, medium-range interactions can be considered by this method.[120] During the development of DFT-D3, it was found that coefficients with an order higher than eight do not have to be taken into account since their contribution is very small. To consider errors due to this approach, the corresponding scaling factor s_8 was adjusted. The six- and eight-ordered damping functions of DFT-D3(zero) are given in (101) and (102), respectively:[120]

$$f_{d,6,DFT-D3(zero)}(r_{ij}) = \frac{1}{1 + 6(\frac{r_{ij}}{s_{r,6} r_{ij,0,DFT-D3}})^{-\alpha_6}} \tag{101}$$

$$f_{d,8,DFT-D3(zero)}(r_{ij}) = \frac{1}{1 + 6(\frac{r_{ij}}{r_{ij,0,DFT-D3}})^{-(\alpha_6+2)}} \quad (102)$$

where $s_{r,6}$ is the scaling factor, depending on the chosen functional, $r_{ij,0,DFT-D3}$ are the cutoff radii for the atom pairs ij and α_6 determines the steepness of the damping function. The values of the cutoff radii $r_{ij,0,DFT-D3}$ were computed for each combination of the first 94 elements in the periodic table.[120] For this purpose, the first-order DFT energy E_1 was calculated as a cutoff energy which has values between 8 and 40 kJ mol^{-1}.[120] This calculation was carried out by building a diatomic ij and adding antisymmetrized and spherical ground state KOHN-SHAM determinants to them. By subtracting from the KOHN-SHAM energy of the unrelaxed system the separate energies of i and j, E_1 is obtained and $r_{ij,0,DFT-D3}$ can be calculated.[120] For the chosen functional PBE, the values for s_6, $s_{r,6}$ and s_8 are 1.0, 1.217 and 0.722, respectively. For every functional, α_6 is 14.[120]

Since these damping functions show for medium-range distances a maximum of contribution of the dispersion energy and then are damped down fast, the correction is called "zero damping".[1,2] To avoid this behaviour and to obtain constant attractive value for these distances, the DFT-D3(BJ) variant with damping functions, proposed by Becke and Johnson, was published in 2011. The dispersion energy $E_{disp,DFT-D3(BJ)}$ is given by (104).[134]

$$E_{disp,DFT-D3(BJ)} = -\frac{1}{2}\sum_{i\neq j}\sum_{n=6,8} s_n \frac{C_{n,ij,DFT-D3}}{r_{ij}^n + [f_{d,DFT-D3(BJ)}(r_{ij,BJ})]^n} \quad (103)$$

where s_n and $C_{n,ij,DFT-D3}$ have the same meaning as in equation (100), while the damping function is now as described in (104).[134]

$$f_{d,DFT-D3(BJ)}(r_{ij,BJ}) = \alpha_1 r_{ij,BJ,DFT-D3} + \alpha_2 \quad (104)$$

where α_1 and α_2 are functional-dependent parameters. To obtain the specific cutoff radii $r_{ij,BJ,DFT-D3}$, (105) is used.[134]

$$r_{ij,BJ,DFT-D3} = \sqrt{\frac{C_{6,ij,DFT-D3}}{C_{8,ij,DFT-D3}}} \quad (105)$$

where $C_{6,ij,DFT-D3}$ and $C_{8,ij,DFT-D3}$ are the environmental dependent six- and eight-ordered dispersion coefficients for the atom pair ij. For PBE, the specific parameters s_6, s_8, α_1 and α_2 are 1.000, 0.7875, 0.4289 and 4.4407, respectively.[134] Apart from these two variants, used in this thesis, there is the approach by Schwabe and co-workers who removed the eight-ordered part in $E_{Disp,DFT-D3}$ and substitute it by a sigmoidal function.[135] From their point of view, the eight-ordered part only interpolates the connection between dispersion energy and the total energy, obtained only by the chosen density functional. So, it is sufficient to model it by their interpolation scheme. For more details, we refer to [135].

As mentioned in the beginning, the main improvement in DFT-D3 is to implement dispersion coefficients which depend on the molecular geometry and thus are system-

dependent. To achieve this, the concept of fractional coordination numbers (CNs) is introduced and given for the atom i in (106).[120]

$$CN(i) = \sum_{i \neq j} \frac{1}{1 + e^{-16\left[\frac{4\left(r_{i,cov} + r_{j,cov}\right)}{3r_{ij}} - 1\right]}} \tag{106}$$

where r_{cov} are covalent radii, based on the concept by Pyykkö and Atsumi. To achieve a consistent treatment in calculating the six-ordered reference dispersion coefficient $C_{6,ij,DFT\text{-}D3,ref}$ are obtained by a modified variant of the Casimir-Polder formula (107).[120]

$$C_{6,ij,DFT-D3,ref}(CN(i), CN(j)) = \frac{3}{\pi}\int_0^\infty d\omega \frac{1}{m}\left[\alpha_{i_m H_n}(i\omega) - \frac{n}{2}\alpha_{H_2}(i\omega)\right] \times \frac{1}{k}\left[\alpha_{i_k H_l}(i\omega) - \frac{1}{2}\alpha_{H_2}(i\omega)\right] \tag{107}$$

where i_mH_n and j_kH_l are element hydrides with specific CNs which are used as reference compounds, m, n, l and k are stoichiometric coefficients and α(iω) are the dipole polarizabilities at an imaginary frequency ω. Instead of using the elements itself as a reference, hydrides were chosen to have a reasonable and consistent approach since energetically low-lying atomic states influence the polarizability in a way that leads to large dispersion coefficients. Due to the fact that in molecules this effect is quenched, and they are simple and well-defined, hydrides were chosen. To obtain the environmental dispersion coefficient $C_{6,ij,DFT\text{-}D3}$, a 2D-grid-based procedure is done in which the reference dispersion coefficients of the environment is included, given by (108).[120]

$$C_{6,ij,DFT-D3}\big(CN(i), CN(j)\big) = \frac{\sum_a^{N_a}\sum_b^{N_b} C_{6,ij,DFT-D3,ref}(CN(i)_a, CN(j)_b) L_{ab}}{\sum_a^{N_a}\sum_b^{N_b} L_{ab}} \tag{108}$$

where N_a and N_b are the numbers of the grid points. This grid is spanned by CN(i) and CN(j). L_{ab} is a Gaussian-type function which describes the distance between the grid points with values of $C_{6,ij,DFT\text{-}D3,ref}$ and ij. L_{ab} is given by (110).[120]

$$L_{ab} = e^{-4[(CN(i)-CN(i)_a)^2 + (CN(j)-CN(j)_b)^2]} \tag{109}$$

After obtaining the geometrically dependent $C_{6,ij,DFT\text{-}D3}$, higher ordered coefficients can be derived. The relevant $C_{8,ij,DFT\text{-}D3}$ dispersion coefficient can be obtained by (110)[120]

$$C_{8,ij.DFT-D3} = 3C_{6,ij,DFT-D3}\sqrt{\frac{1}{4}\sqrt{\frac{z_i}{z_j}}\frac{\langle r^4\rangle_i \langle r^4\rangle_j}{\langle r^2\rangle_i \langle r^2\rangle_j}} \tag{110}$$

where Z are the nuclear charges of i and j, respectively, and $\langle r^2\rangle$ is a dipole- and $\langle r^4\rangle$ is a quadrupole-type expectation values which can be derived by atomic densities.

4.6.3 Tkatchenko-Scheffler method

The dispersion correction method proposed by Tkatchenko and Scheffler nearly follows the idea of Grimme's DFT-D2. The dispersion energy $E_{disp,TS}$, given in (111), obtained by

this method, is nearly calculated in the same way as in (97). Only the scaling factor s_6 is not included.[123]

$$E_{disp,TS} = -\frac{1}{2}\sum_{i\neq j}\frac{C_{6,ij,TS}}{r_{ij}^6} f_{d,TS}(r_{ij}) \tag{111}$$

Instead of a simplified approach to obtain the pairwise dispersion coefficients like in DFT-D2, described in (97), this correction method includes environmental effects on the dispersion coefficients.[123] To do so, a formula for calculating the dispersion coefficient $C_{6,ij,TS}$ is derived by approximating the Casimir-Polder formula via a Padé series which yields the London formula. By substituting the effective frequencies by expressions which are derived by simplifying the London formula to a homonuclear case, (112) for calculating $C_{6,ij,TS}$ is obtained.[123]

$$C_{6,ij,TS} = \frac{2C_{6,ii,TS}C_{6,jj,TS}}{\frac{\alpha_{0,j}}{\alpha_{0,i}}C_{6,ii,TS} + \frac{\alpha_{0,i}}{\alpha_{0,j}}C_{6,jj,TS}} \tag{112}$$

where α_0 is the tabulated static polarizability of the atoms i and j and $C_{6,ii,TS}$ and $C_{6,jj,TS}$ are the environmental dependent homonuclear dispersion coefficients for the diatomic molecules ii and jj. To include the environmental effects in the dispersion coefficients for homonuclear systems, an effective volume V_{eff} is defined and referenced to a volume of a free atom V_{free}. Since there is a relation given between volume and polarizability and the volume can be estimated by Hirshfeld partitioning, (113) can be obtained.[123]

$$\frac{\tau_{i,eff}}{\tau_{i,free}}\frac{\alpha_{i,eff}}{\alpha_{i,free}} = \frac{V_{i,eff}}{V_{i,free}} = \frac{\int r^3 w_i(r) n(r) d^3 r}{\int r^3 n_{i,free}(r) d^3 r} \tag{113}$$

with (114)

$$w_i(r) = \frac{n_{i,free}(r)}{\sum_{all} n_{all,free}(r)} \tag{114}$$

where τ is a proportionality constant between polarizability and volume, n(r) is the total electron density, $n_i(r)$ is the electron density of the atom i, $n_{all,free}(r)$ is the electron density of all free atoms in the system, $w_i(r)$ is the weight function and r^3 is the cube distance from the nucleus of an atom i. Now, the environmental dependent homonuclear dispersion coefficients $C_{6,ii,TS}$ (and analogous for $C_{6,jj,TS}$) can be obtained by (115).[123]

$$C_{6,ii,TS} = \frac{\mu_{i,eff}}{\mu_{i,free}}\left(\frac{\tau_{i,free}}{\tau_{i,eff}}\right)^2\left(\frac{V_{i,eff}}{V_{i,free}}\right)^2 C_{6,ii,free} \tag{115}$$

assuming that

$$\frac{\mu_{i,eff}}{\mu_{i,free}}\left(\frac{\tau_{i,free}}{\tau_{i,eff}}\right)^2 = 1 \tag{116}$$

where μ is the effective frequency of an atom i and $C_{6,ii,free}$ are tabulated homonuclear dispersion coefficients of an atom pair ii. To obtain the dispersion coefficients $C_{6,ij,TS}$ of a heteronuclear atom ij, (112) has to used. For intermolecular dispersion coefficients $C_{6,mol,TS}$ the following rule (117) is used.[123]

$$C_{6,mol,TS} = \sum_{i \in M_1} \sum_{j \in M_2} C_{6,ij,TS} \tag{117}$$

where M_1 and M_2 refer to two different molecules. The damping function $f_{d,TS}(r_{ij})$ has the form of (99) from DFT-D2 but is slightly different, shown in (118).[123]

$$f_{d,TS}(r_{ij}) = \frac{1}{1 + e^{-d\frac{r_{ij}}{s_R r_{ij,0,TS}} - 1}} \tag{118}$$

where d is a damping parameter, here set to 20.0 like in DFT-D2 and s_R is a functional dependent scaling parameter. For the chosen functional PBE, s_R is 0.94. $r_{ij,0,TS}$ are effective van der Waals radii of an atom pair ij which can be obtained the following way via (119).[123]

$$r_{ij,0,TS} = r_{i,0,TS} + r_{j,0,TS} \tag{119}$$

where $r_{i,0,TS}$ and $r_{j,0,TS}$ are the effective van der Waals radii of the atoms i and j, respectively. This effective van der Waals radii can be obtained by (120).[123]

$$r_{0,TS} = \left(\frac{V_{eff}}{V_{free}}\right)^{\frac{1}{3}} r_{0,free} \tag{120}$$

where $r_{0,free}$ is the tabulated van der Waals radius of a free atom. Using this method, the Hirshfeld charges Q_{HF} are obtained according to (121).[123]

$$Q_{HF} = Z - \int dr \frac{n_i(r)}{\sum_{all} n_{all}(r)} n(r) \tag{121}$$

where *Z* is the atomic number of the respective atom.

4.6.4 Many-Body Dispersion (MBD) interaction

Since the TS method only accounts for pairwise dispersion interactions, long-range interactions beyond pairwise contributions are neglected. However, these long-range interactions are getting important for atoms embedded in extended condensed material or big material. Herein, the local environment of the atom in question, the surrounding atoms and their dipoles are significantly affected by each other such that an isolated pairwise consideration does not suffice. Therefore, higher-order interaction terms must be taken into account. One way to address this problem is the Many-Body Dispersion (MBD) approach as proposed by Tkatchenko. Herein, the correlation energy of the random-phase approximation (RPA) as in (123) is considered.[122]

$$E_c = \int_0^\infty \frac{d\omega}{2\pi} Tr[\ln(1 - \nu\chi_0(i\omega)) + \nu\chi_0(i\omega)] \tag{122}$$

ω is the frequency, ν is the interaction potential and $\chi_0(i\omega)$ is the response function.[122] The latter is usually computed by Hartree-Fock or DFT orbitals. However, to conveniently reduce the computational costs and to be able to divide E_c into a short-range and long-range contributions $E_{c,SR}$ and $E_{c,LR}$, a set of quantum harmonic oscillators to model the response function is used.[122] A single oscillator suffices to model the polarizability of an atom $\alpha^0(i\omega)$. This value is obtained by reference data as in the TS scheme. Since range-separation is assumed here, these polarizabilities $\alpha^0(i\omega)$ are screened in the short-range regime and updated.[122]

$$\alpha^{rsSCS}(i\omega) = \alpha^0(i\omega) - \alpha^0(i\omega)\boldsymbol{T_{SR}}\alpha^{rsSCS}(i\omega) \tag{123}$$

with $\mathbf{T_{SR}}$ is the dipole-dipole short-range interaction tensor and $\alpha^{rsSCS}(i\omega)$ are the updated range-separated self-consistently screened polarizabilities.[122] These updated quantities become entries of the polarizability matrix **A** with $3N_{at}x3N_{at}$ entries where N_{at} is the number of atoms. This matrix is used to compute the long-range correlation energy, i.e. the dispersion energy $E_{disp,MBD}$. The computation is carried out in practice for periodic systems in reciprocal space as a discretely summing over the irreducible Brillouin zone (IBZ) as modification of (123):[136]

$$E_{disp,MBD} = -\sum_{k\epsilon IBZ} w_k \int_0^\infty \frac{d\omega}{2\pi} Tr[\ln(1 - \boldsymbol{A}_{LR}\boldsymbol{T}_{LR})] \tag{124}$$

A_{LR} and T_{LR} are the long-range polarizability matrix and long-range dipole-dipole interaction tensor, respectively. The factor w_k weights the summation the space.

4.6.5 The Bayesian error estimation functional (BEEF)-vdW

The Bayesian error estimation functional (BEEF) incorporates non-local dispersion interactions by expanding the enhancement factor F(x) in the GGA exchange functional in (87) by basis of M_x Legendre polynomials $B_m[t(s)]$ from the 0^{th} to the M_x-1^{th} order in a transformed reduced density gradient t(s):[130]

$$\begin{aligned} t(s) &= \frac{2s^2}{4 + s^2}, -1 \le t \le 1 \\ F_x^{GGA}(s) &= \sum_m a_m B_m[t(s)], \\ E_x^{GGA} &= \sum_m a_m \int \varepsilon_x(n)\, B_m[t(s)]dr \\ &= \sum_m a_m E_{x,m}^{GGA} \end{aligned} \tag{125}$$

a_m are the Legendre expansion coefficients and $E_{x,m}^{GGA}$ is the exchange energy with respect to the distinct B_m.[130] To include local and semi-local correlation into this functional, the LDA and PBE correlation functionals E_c^{LDA} and E_c^{PBE} are chosen for this model. The nonlocal vdW correlations are evaluated by the functional E_c^{nl} resulting from a double integration of the nonlocal kernel $\phi(r,r')$ (127) which is also used in vdW-DF2.[131]

$$E_c^{nl} = \frac{\hbar}{2} \iint n(r)\phi(r,r')n(r')drdr' \tag{126}$$

Combining the exchange and correlation functionals results into the BEEF exchange-correlation functional $E_{xc}^{BEEF\text{-}vdW}$.

$$E_{xc}^{BEEF-vdW} = \sum_{m=0}^{M_x-1} a_m E_{x,m}^{GGA} + \alpha_c E_c^{LDA} + (1-\alpha_c)E_c^{PBE} + E_c^{nl} \tag{127}$$

M_x is set to 31, resulting in 30 fitting parameters.[130]

4.6.6 Revised Vydrov and van Voorhis (rVV10) functional

Another density-based functional accounting for non-local interactions is the revised Vydrov and van Voorhis (rVV10) functional in combination with the SCAN functional.[133,137] To obtain the nonlocal functional E_c^{nl}, the kernel $\phi(r,r')$ is evaluated which is given for rVV10 in (128):[133]

$$\begin{aligned}
&\phi^{rVV10}(r,r') \\
&= -\frac{3e^4}{2m^2} \frac{1}{(q|r'-r|^2+1)(q'|r'-r|^2+1)(q|r'-r|^2+q'|r'-r|^2+2)} \\
&\text{with } q(r) = \frac{\omega_0(n(r),\nabla n(r))}{k(n(r))}, \\
&\omega_0 = \sqrt{\omega_g^2 + \frac{\omega_p^2}{3}}, \\
&\omega_p^2 = \frac{4\pi n e^2}{2} \text{ and } \omega_g^2 = C\frac{\hbar^2}{m^2}\left|\frac{\vec{\nabla} n}{n}\right|^4, \\
&\text{and } k = 3\pi b\left(\frac{n}{9\pi}\right)^{\frac{1}{6}}
\end{aligned} \tag{128}$$

ω_p^2, ω_g^2 and k are the plasma frequency, the so-called band gap and a control parameter which ensures the short-range damping of the $|r'-r|^{-6}$ divergence in $\phi^{rVV10}(r,r')$, respectively.[138] The parameter C controls the accurate van-der-Waals interactions at large distances between atoms and molecules, and it is set to 0.0093 also in SCAN-rVV10 like in semi-local functionals. However, the parameter b in (128) was reconsidered for merging rVV10 and SCAN. As a result of benchmark calculations, comparing SCAN-rVV10 to, for instance, coupled cluster results, the best agreement is found for b=15.9.[133]

4.7 Periodic Systems

4.7.1 Bloch's Theorem

In contrary to isolated molecules, in periodic systems an atom or molecules at a position $\vec{r}$ is invariant in terms of its properties, translating it by $\vec{R}$. This can be postulated since a particle at $\vec{r}$ is in an identical environment as at $\vec{r}+\vec{R}$. Therefore, the potential energy of an electron $V(\vec{r})$ must be same as $V(\vec{r}+\vec{R})$, as Bloch's theorem proposes. The same applies to Hamiltonian and the wavefunction $\psi(\vec{r})$ of the electron.[139]

$$\psi(\vec{r}) = f(\vec{r})\psi(\vec{r}+\vec{R}) \tag{129}$$

where $f(\vec{r})$ is a location-independent factor to consider symmetry of the system, given by (130).[139]

$$f(\vec{r}) = e^{i\vec{k}\vec{r}} \tag{130}$$

where $\vec{k}$ is the wave vector which determines the position of a particle in reciprocal space. In order to apply the periodic boundary conditions to the wavefunction, a function $u_{\vec{k}}(\vec{r})$ is defined which is invariant by translation with $\vec{R}$, so that $u_{\vec{k}}(\vec{r})$ and $u_{\vec{k}}(\vec{r}+\vec{R})$ are identical. Now, the wavefunction $\psi(\vec{r})$ is given by (131).[139]

$$\psi(\vec{r}) = e^{i\vec{k}\vec{r}}u_{\vec{k}}(\vec{r}) \tag{131}$$

It can be shown that DFT simulations are less demanding in terms of computational time. So, simulations of periodic systems are performed in reciprocal space which can be obtained by Fourier-transforming the real-space coordinates. There are several approaches to model $u_{\vec{k}}(\vec{r})$. For this thesis, planes waves were used.[139]

4.7.2 Planes Waves

In order to model $u_{\vec{k}}(\vec{r})$, a linear combination of plane waves is used, given by (132).[140,141]

$$u_{\vec{k}}(\vec{r}) = \frac{1}{\sqrt{\Omega_{Brillouin}}}\sum_{\vec{G}}^{\vec{G}\leq\vec{G}_{cut}} C_{\vec{G}}e^{i\vec{G}\vec{r}} \tag{132}$$

where $\Omega_{Brillouin}$ is the volume of the first Brillouin zone of the periodic unit cell, $\vec{G}$ is the sum of the space vectors in reciprocal space, $\vec{G}_{cut}$ is a cutoff criteria and $C_{\vec{G}}$ is complex Fourier factor. If (132) is used in (131), (133) can be obtained.[140,141]

$$\psi_{\vec{k}}(\vec{r}) = \frac{1}{\sqrt{\Omega_{Brillouin}}}\sum_{\vec{G}}^{\vec{G}\leq\vec{G}_{cut}} C_{\vec{k}+\vec{G}}e^{i(\vec{G}+\vec{k})\vec{r}} \tag{133}$$

whereby a plane wave P_w is defined by (134)[140,141]

$$P_w = \frac{1}{\sqrt{\Omega_{Brillouin}}} C_{\vec{k}+\vec{G}_w} e^{i(\vec{G}_w+\vec{k})\vec{r}} \tag{134}$$

where $C_{\vec{k}+\vec{G}}$ and $C_{\vec{k}+\vec{G}_w}$ are again complex Fourier factors, respectively, and $\vec{G}_w$ represents one cell vector in reciprocal space. Since the first Brillouin zone is the smallest symmetry unit in the periodic unit cell it is sufficient to simulate the electronic properties inside the first Brillouin zone. Symmetry operations are used to transfer the calculated properties to the overall system. During simulations, $C_{\vec{k}+\vec{G}}$ are optimized. For modelling $\theta_{KS,z}$, P_w and the linear combination of them in (133) is used. In fact, a cutoff $\vec{G}_{cut}$ has to be defined to truncate computational time and to guarantee that the contribution of $C_{\vec{k}+\vec{G}}$ does not become too small so that reasonable results are obtained, given in (135).[140,141]

$$\left|\vec{G}_{cut}\right| = \frac{\sqrt{2m_e E_{cut}}}{h} \tag{135}$$

where m_e is the mass of one electron, E_{cut} is the cutoff energy which needs to be defined and h is the Planck constant. This approach is advantageous due to the fact that for example basis-set superposition errors are avoided. Nevertheless, electrons near the core have wavefunctions with high frequencies. Either a high cutoff energy, i.e. many plane waves need to be used which means high computational effort, though, or the following two approaches are used: Pseudopotentials (PP) and Projector-Augmented-Wave (PAW) method.[142,143] The first approach will be described short in the following since the latter approach was used in this thesis.

4.7.3 Pseudopotentials

Pseudopotentials have been introduced to avoid the strong oscillation of the wavefunction of electrons near to the core. In fact, the number of nodes of these wavefunctions has to be reduced or ideally removed completely. To do so, three approximations are assumed: the one-electron picture, the frozen-core approximation and the small-core approximation.[142] All these assumptions together enable to divide up the electrons into core and valence electrons whose states do not overlap. Moreover, the states of the core electrons are assumed to be constant. Figure 22 shows how a wavefunction and potential look if the pseudopotential is and is not used.

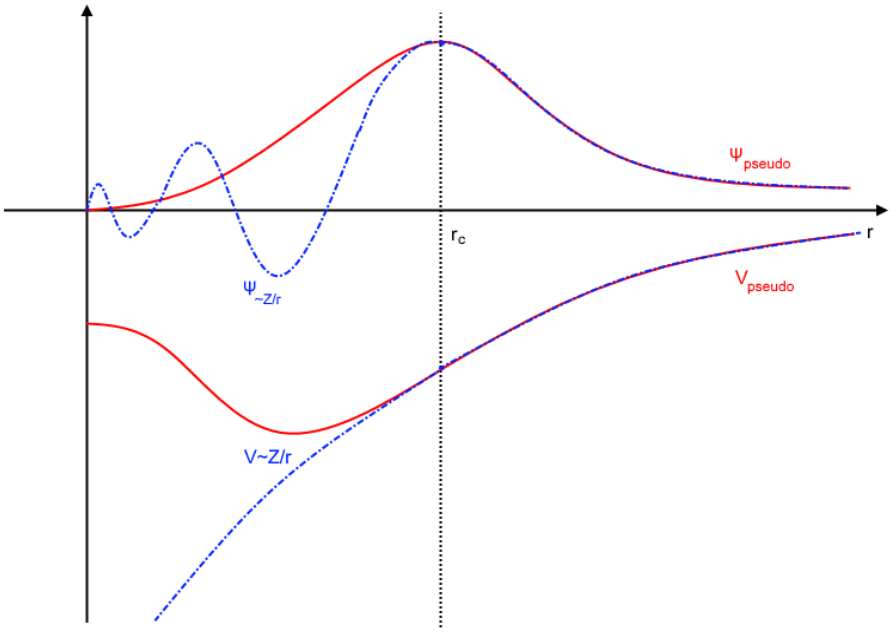

Figure 22: Comparison between a pseudopotential V_{pseudo} (red lines) and a Coulomb potential V~Z/r (blue dashed lines; Z is the nuclear charge number) for core electrons and their wavefunctions ψ, depending on the distance r (r_c is the cutoff radius). (Adapted from [142])

Inside the augmentation region ($r<r_c$), the wavefunction with a pseudopotential does not have nodes and is not oscillating, whereas the wavefunction with a Coulomb potential does. Outside the augmentation region ($r>r_c$) they show the same behavior. Pseudopotentials must conserve the nuclear charge, the eigenvalues of the valence electrons have to be same as with an all-electron potential, the wavefunction should not oscillate much and by inversion of Schrödinger's equation excited states should be considered. Norm-conserving pseudopotentials and ultra-soft pseudopotentials are the most common pseudopotentials nowadays. Due to the rough estimation made for the core electron, on the one hand the computational effort is reduced since many states are reduced to one. One the other hand, all information of the core electron is lost and is not known beforehand. To address this issue, the PAW method has been introduced.[142]

4.7.4 Projector Augmented-Wave Method

The PAW method, first introduced by Blöchl in 1994, is a generalization of the Augmented-Plane-Wave (APW) method.[143] Inside an augmentation sphere the wavefunctions are taken as some atom-like partial waves and outside this sphere- the bonding region- envelop functions are defined. In the beginning, a transformation operator $\hat{T}$ is defined which transforms an auxiliary wavefunction $|\tilde{\Psi}_m\rangle$ to the true all-electron Kohn-Sham single particle wavefunction $|\Psi_m\rangle$.[143]

$$|\Psi_m\rangle = \hat{T}|\tilde{\Psi}_m\rangle \tag{136}$$

where m a quantum labels. A transformed Kohn-Sham equation is obtained which now need to solved.[143]

$$\hat{T}^* \hat{H}_s \hat{T} \left| \tilde{\Psi}_m \right\rangle = \varepsilon_m \hat{T}^* \hat{T} \left| \tilde{\Psi}_m \right\rangle \tag{137}$$

where $\hat{T}^*$ is the complex conjugated form of $\hat{T}$. In order to address only the core electrons with their oscillating wavefunctions the transformation operator $\hat{T}$ is defined like in (138).[143]

$$\hat{T} = 1 + \sum_a \hat{T}_a \tag{138}$$

where a is an atom index. Due to this definition, $\hat{T}_a$ affects only the wavefunction of electrons within a certain augmentation sphere. On top, the wavefunction $|\Psi_m\rangle$ can be expanded inside the augmentation sphere in partial waves $|\varphi_{y,a}\rangle$ which are obtained by the transformation of each corresponding auxiliary partial wavefunctions $|\tilde{\varphi}_{y,a}\rangle$.[143]

$$|\varphi_{y,a}\rangle = (1 + \hat{T}_a) \, |\tilde{\varphi}_{y,a}\rangle \tag{139}$$

The PAW method also assumes the frozen-core approximation. However, it can reconstruct all-electron orbitals by re-transforming the pseudo-orbitals which are used to model the augmentation region, i.e. the core region. Only the latter region needs to be corrected by an all-electron calculation of each atom.[143]

4.8 Electron Density Difference Analysis

In order to get an idea of the electronic structure of a system, the electron density difference analysis is a useful tool. It is calculated by (140).

$$\Delta\rho(A, B, C, \ldots) = \rho(A, B, C, \ldots) - \sum_{i=A,B,C,\ldots} \rho(i) \tag{140}$$

where Δρ(A, B, C, …) is the electron density difference of the whole system, ρ(A, B, C, …) is the electron density of the whole system and ρ(i) is the electron density of each component A, B, C, … in the system. Using this idea, it can be seen where electron density accumulates for instance.

4.9 Quantum Theory of Atoms in Molecules (QTAIM)

The Quantum Theory of Atoms in Molecules was developed by Richard Bader and analyses the amount of space which one atom in a molecule needs by analysing its electron density in space $\rho(\vec{r})$.[144] In this context one also speaks of the topological analysis of the

electron density. An atom is in sense of this theory defined by an atomic basin. The boundaries of a basin are given by the zero-flux surfaces.[144] The gradient of the electron density $\vec{\nabla}\rho(\vec{r})$ always starts at the nuclear attractors which are cores of an atom. Those surfaces which the gradient of electron density approaches asymptotically, but which it never crosses are the zero-flux surfaces. Therefore, the condition (141) applies for zero-flux surfaces.[144]

$$\vec{\nabla}\rho(\vec{r}) \cdot \vec{n} = 0 \tag{141}$$

where $\vec{n}$ normal vector and $\vec{\nabla}$ is defined as

$$\vec{\nabla} = \begin{pmatrix} \frac{\partial}{\partial x} \\ \frac{\partial}{\partial y} \\ \frac{\partial}{\partial z} \end{pmatrix} \tag{142}$$

The atomic properties of the basin B are the atomic volume V(B) and the atomic charge Q(B) which can be obtained by integrating over the volume unit dV.[144]

$$V(B) = \int_0^B dV \tag{143}$$

$$Q(B) = Z - N(B) = Z - \int_0^B \rho(\vec{r}) dV \tag{144}$$

where Z is the nuclear charge and N(B) is the number of charge carriers in the basin B. Especially, the basins of terminal atoms can be infinitely large and therefore the isovalue of electron density is defined as a cutoff criteria.[144] For instance, if a isovalue of 0.0001 a.u. as in this thesis is chosen, the atomic volume and the atomic charge are defined by $V_{0001}(B)$ and $Q_{0001}(B)$, respectively. Apart from the zero-flux surface there are the critical points where the gradient of the electron density is zero. To classify these points, the curvature at these points is analysed by defining a Hessian $H(\vec{r})$ (145) which here is diagonalised.[144]

$$H(\vec{r}) = \begin{pmatrix} \frac{\partial^2}{\partial x^2} & 0 & 0 \\ 0 & \frac{\partial^2}{\partial y^2} & 0 \\ 0 & 0 & \frac{\partial^2}{\partial z^2} \end{pmatrix} = \begin{pmatrix} \lambda_1 & 0 & 0 \\ 0 & \lambda_2 & 0 \\ 0 & 0 & \lambda_3 \end{pmatrix} \tag{145}$$

In order to characterise the critical points, two parameters are used: the rank χ and the signature σ. The rank χ is the number of λ which are not zero, so χ is by definition always 3 for critical points. The signature σ is the sum of the mathematical signs of λ. Therefore, there is the following nomenclature for the critical points depending on χ and σ:

(3, -3): nuclear attractor; it has a maximum of the electron density in each spatial direction. In the most cases it corresponds to the atomic core.[144]

(3,-1): bond critical point; it is a saddle point in the electron density with one minimum along the bond and two maxima. In the most cases, it is a part of a chemical bond.[144]

(3,+1): ring critical point; it is also a saddle point in the electron density with two minima inside the ring plane and one maximum.[144]

(3,+3): cage critical point; it is a total minimum in the electron density, so the corresponding system has to be cage-like.[144]

The number in the parentheses are (χ, σ). Especially, the bond critical point is interesting for analysis of a chemical bond. It has to be part of the bond path which is between two nuclear attractors. In sense of QTAIM, a chemical bond is present between two atoms if the corresponding nuclear attractors have a bond path and share an interatomic zero-flux surface and a bond critical point which is located on the corresponding zero-flux surface. In order to characterise the bond, there are several parameters. In this thesis, the electron density ρ_{bcp} the Laplacian $(\vec{\nabla})^2\rho_{bcp}$ of the electron density at the bond critical point BCP and the ellipticity ε_{bcp} were used. The latter is given by (146):[144]

$$\epsilon_{bcp} = \frac{\lambda_1}{\lambda_2} - 1 \tag{146}$$

The first two criteria define the character of the bond, and the latter estimates its order and symmetry.

4.10 Calculation of the reaction intermediates

In order to be able to calculate reaction pathways, the free-energy landscape of a reaction including their intermediates must be evaluated. In case of computational electrocatalysis, proton-electron transfers are crucial to drive an electrochemical reaction as they respond to the application of potential. In case of an oxidative reaction, the reaction free energy at non-applied potential $\Delta G_{H_{n-1}A^*}(U=0)$ of the proton-electron-transfer step is given by (147):[145]

$$\Delta G_{H_{n-1}A^*}(U=0) = \left(G_{H_{n-1}A^*} + \frac{1}{2}G_{H_2}\right) - G_{H_nA^*} \tag{147}$$

$G_{H_{n-1}A^*}$, G_{H_2} and $G_{H_nA^*}$ are the free energy of the oxidized intermediate, of the hydrogen molecule and the reduced intermediate. The proton-electron transfer step is approximated by the free energy of a hydrogen molecule since the Computational Hydrogen Electrode (CHE) is employed here.[145] This method is being explained in the section 4.12. We are now introducing how the DFT energies are corrected to obtain free energies.

4.11 Free energy and Thermodynamic Corrections

DFT-obtained electronic energies are calculated at 0K temperature. Thermodynamic corrections are needed to compare energies obtained from calculation with experimental data, and the Gibbs free energies can be given by:[19]

$$G^0 = E_{DFT} + E_{ZPE} + U^0 - TS^0 \tag{148}$$

where, E_{DFT} is the ground-state energy calculated with DFT and E_{ZPE} is the zero-point energy correction and is expressed as:[19]

$$E_{ZPE} = \sum_i \frac{h\nu_i}{2} \tag{149}$$

The standard molar vibrational, thermal energy is expressed as:[19]

$$U^0_{vib} = RT \sum_i \frac{{}^{h\nu_i}/_{k_B}}{e^{{}^{h\nu_i}/_{k_BT}} - 1} \tag{150}$$

Finally, vibrational entropy is given by:[19]

$$S^0_{vib} = R \sum_i [\frac{{}^{h\nu_i}/_{k_B}}{e^{{}^{h\nu_i}/_{k_BT}} - 1} - \ln\,(1 - e^{{}^{h\nu_i}/_{k_BT}})] \tag{151}$$

where h is Plank's constant, ν_i is the vibrational frequency calculated based on the harmonic oscillator approximation, R represents the gas constant and k_B is Boltzmann's constant.

4.12 The Computational Hydrogen Electrode (CHE)

To model electrochemical systems and to obtain and to predict properties of this system is a challenging and formidable task in which many parameters need to be taken account. The electrolyte and the interface between electrolyte and electrode, for instance, are dynamic systems which are interconnected and affect the stability of the reaction intermediates.[146,147] Additionally, the electric field which is generated upon the presence of a voltage affects the physical and chemical properties of the electrochemical system. Nevertheless, to approximate the thermodynamic landscape of electrochemical reactions, the CHE method has been developed and become a useful tool for deciphering and predicting reactions in these systems. To account for the effect of applied potential U, the reaction free energy $\Delta G_{H_{n-1}A^*}(U=0)$ is corrected by a linear term eU.[145]

$$\Delta G_{H_{n-1}A^*}(U) = \Delta G_{H_{n-1}A^*}(U = 0) + eU \quad (152)$$

The effect of applied potential on the reaction step is intrinsically considered in this method and it only requires calculating the free energy without potential in the beginning. The free energy change $\Delta G_i(U)$ to transform from intermediate $H_{n-1}A^*$ to $H_{n-2}A^*$, i.e. an oxidation.[54,145]

$$\Delta G_i(U) = \Delta G_{H_{n-2}A^*}(U) - \Delta G_{H_{n-1}A^*}(U) \quad (153)$$

The potential U in the CHE approach is referenced at the Reversible Hydrogen Electrode (RHE) for which the reaction (155) is assumed to be in equilibrium.[145]

$$\frac{1}{2}H_2 \rightleftharpoons H^+ + e^-; \Delta G \stackrel{\text{def}}{=} 0 \quad (154)$$

The chemical transformation of the different intermediates becomes thermodynamically feasible if $\Delta G_i(U)<0$. The step which requires the highest potential to drive the reaction exergonically is the potential-determining step (PDS) which defines the thermodynamic barrier of the electrochemical reaction.

5 Summary of Articles

5.1 Article I

"Perspectives on the Competition between the Electrochemical Water and N_2 Oxidation on a TiO_2(110) Electrode"

The Journal of Physical Chemistry Letters 13 no. 26 (2022): 6123-6129.

The conventional way of nitrogen (N_2) oxidation towards nitrate (NO_3^-), an important component of fertilizers, is a two-step process. Atmospheric nitrogen is firstly reduced to ammonia (NH_3) by the Haber-Bosch process or bacteria in the soil which is then oxidized by the Ostwald process or other bacteria. Since both the Haber-Bosch and the Ostwald process account for 2% of the carbon dioxide emissions worldwide, alternative approaches must be found. The direct oxidation of nitrogen, occurring in nature during lightning, requires a huge amount of energy, reflecting the strength of nitrogen triple bond. Despite unsuccessful attempts to commercialize the nitrate production by nitrogen oxidation through the Birkeland-Eyde process, the electrochemical Nitrogen Oxidation Reaction (NOR) has drawn attention to researchers and has been reconsidered for sustainable nitrate production. In our work, we explored the competition between nitrogen and water oxidation on rutile TiO_2(110) electrode. We employ thermodynamic and advanced Grand-Canonical- (GC-) DFT calculations which account for implicit and explicit solvation effects and the effect of applied potential on the solid-liquid interface.

Our calculations reveal a close competition between the NOR and OER. The formation of the peroxide intermediate *OOH is identified as the rate-determining step, featuring a high barrier. Therefore, the combination of the previous OER intermediate *O and N_2 and other NOR intermediates become feasible. However, the NOR steps are barely affected by the potential, whereas the competing OER step is electrochemical. On top, nitrogen is a hydrophobic reactant which hardly dilutes into an aqueous electrolyte. Based on our results and to address the concerns, we suggest saturating the electrolyte with oxygen and potential pulsing as valuable strategies to enable the NOR and to supress the OER.

5.2 Article II

"Elucidating the Active Sites and Synergies in Water Splitting on Manganese Oxide Nanosheets on Graphite Support"

Advanced Energy Materials 13 no. 43 (2023): 2302039.

The pressing challenges of the climate crisis reflect the urgent need to transform from a fossil-fuel-based to a sustainable society. A crucial cornerstone to achieve this transformation is utilising electrochemical devices such as fuel cells. However, costly

materials such as iridium oxide are the most efficient electrocatalysts for the anodic Oxygen Evolution Reaction (OER). To ensure accessibility to countries with limited financial resources, we have chosen to investigate electrode materials derived from Earth-abundant sources, considering the need for affordability and availability. Carbon is such a material with huge deposits around the globe. However, electrodes, being made of pristine carbon materials such as Highly Oriented Pyrolytic Graphite (HOPG), are poor OER catalysts with high overpotential. Therefore, we choose to study a composite material which consists of HOPG and manganese oxide nanosheets (MnO_2NS), which is also an abundant material. Furthermore, nature's solution also uses a manganese-oxide-based cluster embedded in a protein matrix to drive the OER at low overpotentials. Consequently, we expect significant improvement of the OER activity of MnO_2NS/HOPG compared to the pristine components.

We study these materials with various electrochemical and spectroscopic techniques, noise electrochemical scanning electrochemical microscopy (n-EC-STM) and our DFT calculations. After synthesizing and characterizing the materials, electrochemical measurements revealed the expected enhanced OER activity of MnO_2NS/HOPG. To elucidate the origin of the heightened catalytic performance, microscopic measurements are employed which detect electrochemical activity at the MnO_2NS/HOPG interface. Our DFT calculations on various model systems including pristine graphene and graphite and interface models of the MnO_2NS/HOPG composite could propose a reasonable mechanism. The proposed pathways align with the experimental findings and reveal a barrierless initiation of the OER at the edges of the MnO_2NS. The terminal oxygen bound to manganese are the moieties which are the key component in this bicomponent system. Consequently, the synthetic strategy to deposit the MnO_2NS onto HOPG should be geared towards small particles with a high amount of edge sites.

5.3 Article III

"The Role of Manganese Oxide Nanosheets in Pyrolyzed Carbonaceous Supports for Water Oxidation"

submitted in April 2024

The climate crisis is not only an environmental and humanitarian crisis which comes with an enhancing number of catastrophic instances such as draughts and floods but also heightened monetary costs to compensate damages and prevention measures. To address the latter concern, affordable and accessible resources are needed to build energy devices such as batteries or fuel cells which store or produce energy from renewable sources. Building upon our previous study on the electrochemical Oxygen Evolution Reaction (OER) in Highly Oriented Pyrolytic Graphite (HOPG) without and with deposited manganese oxide nanosheets (MnO_2NS), we study carbonized iron phthalocyanine (CFePc) deposited onto HOPG without and with deposited MnO_2NS. We employ spectroscopic and electrochemical techniques, noise electrochemical scanning tunnelling microscopy (n-EC-STM) and Density Functional Theory (DFT) calculations to gain holistic insights into the different investigated electrocatalysts.

Following the synthesis and spectroscopic characterization of the materials, the electrochemical measurements reveal that CFePc on HOPG (CFePc/HOPG) already outperforms HOPG without and with MnO_2NS (HOPG and MnO_2NS/HOPG, respectively) with respect to OER performance. Moreover, the tricomponent material consisting of HOPG, CFePc and MnO_2NS shows further improvement in its OER activity compared to the other catalysts, remarkably in the low-overpotential region. The n-EC-STM measurements visualize the OER activity in the material and detect active areas at the metal centers of the CFePc and the interface between MnO_2NS and CFePc/HOPG. The DFT calculations explain these findings further. The improved electrocatalytic activity of CFePc is assigned to a low overpotential at the iron center of this material which dominates the generated current density at potentials higher than 1.65 V vs RHE. At potentials lower than 1.65 V vs RHE, the produced current largely originates from MnO_2NS in which their edge sites feature a lack of thermodynamic barrier, unveiled by our DFT calculations. Based on our results, we propose a blueprint for this kind of electrocatalysts which should contain small MnO_2 particles to obtain many edge sites and a sufficient amount of metal doping from appropriate precursors such as phthalocyanine.

6 Conclusion and Outlook

This thesis deals with shedding light on electrochemical oxidation reactions on electrode materials made of abundant resources, combining experimental and computational tools. We explore a space of various materials and their combinations and elucidate their role in the anodic reactions. In the end of each study, we could provide the reader and fellow researchers with guidelines how to perform future studies and to optimize the results which are obtained in our studies. Research objectives and questions have been defined in the beginning of this dissertation which are being answered explicitly in the following.

Research Objectives:

1. *Explain the reason for the enhanced OER activity of Highly Oriented Pyrolytic Graphite (HOPG) with manganese oxide nanosheets (MnO_2NS) compared to pristine HOPG.*
   Our joint experimental and theoretical efforts elucidate the reason of the low activity of HOPG and the enhanced OER performance of the other composite materials. The origin is assigned to the edges of the manganese oxide nanosheets (MnO_2NS) at the interface between HOPG and MnO_2NS which improve the measured electrocatalytic activity. Furthermore, the iron doping improves the catalytic OER activity which is explained by the presence of the metal centers. The DFT calculations revealed a) a lack of a thermodynamic barrier at the interface between MnO_2NS and the carbonaceous support and b) a low overpotential at the iron center which starts to dominate the production of current later. We propose design guidelines which could improve these catalysts in future investigations.

2. *Find and identify the most active site in these electrocatalysts (HOPG, MnO_2NS/HOPG, CFePc/HOPG and MnO_2NS/CFePc/HOPG) which align with and can explain the experimental results.*
   The predominantly active sites in MnO_2NS/HOPG are the edge sites of the MnO_2NS, while some activity is detected on the terraces of the MnO_2NS. The DFT calculations reveal high thermodynamic barriers at HOPG and the terraces of the MnO_2NS, while the edge sites do not feature a barrier in the beginning of the calculated OER pathway. Similar results are obtained for the interface between MnO_2NS and CFePc/HOPG, but the calculations also prove in accordance with the experimental results that the iron centers dominate the production of the current at high overpotentials.

3. *Explain how the OER competes with other electrochemical oxidation reaction such as the NOR.*
   The GC-DFT calculations, which account for effects of the solid-liquid interface and of applied potential, reveal that the OER supports and supress the NOR. The OER intermediates are needed to oxidize the nitrogen and the products of this oxidation, but this process competes with the further OER steps. Potential pulsing

and manipulation of the electrolyte can be valuable strategies to supress the OER towards the NOR and to drive the NOR on a TiO_2(110) electrode which could be considered in future investigations.

Research Questions:

1. *Why are manganese oxide nanosheets on HOPG (MnO_2NS/HOPG) more active than pristine HOPG?*
   The DFT calculations reveal both a lack of a thermodynamic barrier at the edge sites of the MnO_2NS and too high barriers at the terraces of MnO_2NS and HOPG. The formation of the first intermediate $*O_{Mn}OH$ at the edge site at the interface region do not have any additional thermodynamic barrier which must be overcome, while the first step of the OER at the other locations feature a significant barrier.

2. *Why is HOPG functionalized with carbonized iron phthalocyanine (CFePc) even more active than MnO_2NS/HOPG?*
   The electrochemical measurements show that CFePc/HOPG is more active than MnO_2NS/HOPG. The n-EC-STM images prove that the activity arises from local features in the electrocatalyst, represented by peaks in these images. The DFT calculations unveil a low overpotential at the iron centers which confirm that this electrocatalyst is more active than MnO_2NS/HOPG.

3. *What is the role of MnO_2NS in this class of materials? How do they contribute to the enhanced activity as seen in the experiments?*
   In case of MnO_2NS/HOPG, the presence of MnO_2NS tremendously enhance the OER activity due to the edge sites provided by the MnO_2NS and the lack of a thermodynamic barrier at the beginning of the proposed OER pathway. The MnO_2NS get activated further by an electron transfer from the substrate to the nanosheet. However, the nanosheets improve the performance in the low overpotential region when they are deposited onto CFePc/HOPG and increase the amount of obtained current there. At higher potential than the onset of CFePc, the CFePc dominates the obtained current.

4. *What are the reasonable mechanisms which can explain and map the energetic landscape and therefore the activity?*
   Different mechanisms take place at the different locations which are investigated. The conventional electrochemical mechanism is proposed for the OER at HOPG and CFePc, starting with the formation of *OH intermediate and going towards the formation of gaseous dioxygen. The mechanisms of the MnO_2NS are different. Herein, the first step involves lattice oxygen which leads to the formation of the $*O_{Mn}OH$ intermediate which is deprotonates to dioxygen. The catalyst is then recovered by the further steps of the OER which are also the most challenging steps of the water oxidation there.

5. *Which factors determine whether the OER outperforms other electrochemical oxidations reactions such as the NOR?*
   These factors are determined by the constitution of the solid-liquid interface and the coverage of the corresponding OER intermediates. The electrochemical potential destabilizes the *O intermediate which can combine with nitrogen and the other

NOR intermediates and get oxidized towards nitrate. However, nitrogen is a hydrophobic moiety which poorly dissolves in aqueous electrolytes, and it is therefore questionable if a sufficient amount of nitrogen is present at the interface. Since the concentration of water in an aqueous electrolyte is high, it is likely that it combines with the OER intermediates on the surface in an electrochemical step. However, by manipulating the set potential appropriately and the composition of the electrolyte, the NOR could be favoured towards the OER.

As a result, this work could reveal the underlying principles of oxidation reactions on abundant materials. The DFT calculations identify the crucial mechanistic parameters which determine the enhanced OER activity in composite materials. Future studies can use the concepts which are found there. The synthetic strategy of the MnO_2NS should be geared towards small particles to obtain a significant amount of edge sites. Furthermore, this nanosheet could be doped to stabilize the edge sites and to lower the overpotential to recover the catalyst there. On top, the substrate could be doped with other abundant metals and their precursors.

To control the competition between the OER and other oxidation reaction, further studies on the solid-liquid interface are crucial. Besides experimental insights, dynamic simulation coupled with GC-DFT methodologies could assist to elucidate important parameters at this location of electrocatalyst. Knowledge of the composition and the local pH there will be beneficial to design efficient electrocatalysts which are needed for a sustainable future.

References

(1) Calvin, K.; Dasgupta, D.; Krinner, G.; Mukherji, A.; Thorne, P. W.; Trisos, C.; Romero, J.; Aldunce, P.; Barrett, K.; Blanco, G.; Cheung, W. W. L.; Connors, S.; Denton, F.; Diongue-Niang, A.; Dodman, D.; Garschagen, M.; Geden, O.; Hayward, B.; Jones, C.; Jotzo, F.; Krug, T.; Lasco, R.; Lee, Y.-Y.; Masson-Delmotte, V.; Meinshausen, M.; Mintenbeck, K.; Mokssit, A.; Otto, F. E. L.; Pathak, M.; Pirani, A.; Poloczanska, E.; Pörtner, H.-O.; Revi, A.; Roberts, D. C.; Roy, J.; Ruane, A. C.; Skea, J.; Shukla, P. R.; Slade, R.; Slangen, A.; Sokona, Y.; Sörensson, A. A.; Tignor, M.; van Vuuren, D.; Wei, Y.-M.; Winkler, H.; Zhai, P.; Zommers, Z.; Hourcade, J.-C.; Johnson, F. X.; Pachauri, S.; Simpson, N. P.; Singh, C.; Thomas, A.; Totin, E.; Alegría, A.; Armour, K.; Bednar-Friedl, B.; Blok, K.; Cissé, G.; Dentener, F.; Eriksen, S.; Fischer, E.; Garner, G.; Guivarch, C.; Haasnoot, M.; Hansen, G.; Hauser, M.; Hawkins, E.; Hermans, T.; Kopp, R.; Leprince-Ringuet, N.; Lewis, J.; Ley, D.; Ludden, C.; Niamir, L.; Nicholls, Z.; Some, S.; Szopa, S.; Trewin, B.; van der Wijst, K.-I.; Winter, G.; Witting, M.; Birt, A.; Ha, M. *IPCC, 2023: Climate Change 2023: Synthesis Report. Contribution of Working Groups I, II and III to the Sixth Assessment Report of the Intergovernmental Panel on Climate Change [Core Writing Team, H. Lee and J. Romero (Eds.)]. IPCC, Geneva, Switzerland.*; Arias, P., Bustamante, M., Elgizouli, I., Flato, G., Howden, M., Méndez-Vallejo, C., Pereira, J. J., Pichs-Madruga, R., Rose, S. K., Saheb, Y., Sánchez Rodríguez, R., Ürge-Vorsatz, D., Xiao, C., Yassaa, N., Romero, J., Kim, J., Haites, E. F., Jung, Y., Stavins, R., Birt, A., Ha, M., Orendain, D. J. A., Ignon, L., Park, S., Park, Y., Reisinger, A., Cammaramo, D., Fischlin, A., Fuglestvedt, J. S., Hansen, G., Ludden, C., Masson-Delmotte, V., Matthews, J. B. R., Mintenbeck, K., Pirani, A., Poloczanska, E., Leprince-Ringuet, N., Péan, C., Eds.; 2023. https://doi.org/10.59327/IPCC/AR6-9789291691647.

(2) Wigley, T. M. L. Global-mean Temperature and Sea Level Consequences of Greenhouse Gas Concentration Stabilization. *Geophys. Res. Lett.* **1995**, *22* (1), 45–48. https://doi.org/10.1029/94GL01011.

(3) NOAA National Centers for Environmental Information- Annual 2023 Global Climate Report. **2024**.

(4) Global Temperature | Vital Signs – Climate Change: Vital Signs of the Planet https://climate.nasa.gov/vital-signs/global-temperature/?intent=121 (accessed Apr 25, 2024).

(5) Climate at a Glance | Global Time Series | National Centers for Environmental Information (NCEI) https://www.ncei.noaa.gov/access/monitoring/climate-at-a-glance/global/time-series (accessed Apr 25, 2024).

(6) Masa, J.; Barwe, S.; Andronescu, C.; Schuhmann, W. On the Theory of Electrolytic Dissociation, the Greenhouse Effect, and Activation Energy in (Electro)Catalysis: A Tribute to Svante Augustus Arrhenius. *Chem. - A Eur. J.* **2019**, *25* (1), 158–166. https://doi.org/10.1002/CHEM.201805264.

(7) Biological Consequences Of Global Warming | by Ayesharasool | Medium https://medium.com/@ayesharasool788/biological-consequences-of-global-warming-a22242dcce9b (accessed Apr 25, 2024).

(8) U.S. Billion-Dollar Weather and Climate Disasters, 1980 - Present. *Natl. Centers Environ. Inf.* **2020**. https://doi.org/10.25921/STKW-7W73.

(9) Consequences of climate change - European Commission https://climate.ec.europa.eu/climate-change/consequences-climate-change_en (accessed Mar 22, 2024).

(10) Hinkel, J.; Lincke, D.; Vafeidis, A. T.; Perrette, M.; Nicholls, R. J.; Tol, R. S. J.; Marzeion, B.; Fettweis, X.; Ionescu, C.; Levermann, A. Coastal Flood Damage and Adaptation Costs under 21st Century Sea-Level Rise. *Proc. Natl. Acad. Sci. U. S. A.* **2014**, *111* (9), 3292–3297. https://doi.org/10.1073/PNAS.1222469111.

(11) Ramm, T. D.; Watson, C. S.; White, C. J. Describing Adaptation Tipping Points in Coastal Flood Risk Management. *Comput. Environ. Urban Syst.* **2018**, *69*, 74–86. https://doi.org/10.1016/j.compenvurbsys.2018.01.002.

(12) Bamber, J. L.; Aspinall, W. P. An Expert Judgement Assessment of Future Sea Level Rise from the Ice Sheets. *Nat. Clim. Chang.* **2013**, *3* (4), 424–427. https://doi.org/10.1038/NCLIMATE1778.

(13) McDonnell, S. The Importance of Attention to Customary Tenure Solutions: Slow Onset Risks and the Limits of Vanuatu's Climate Change and Resettlement Policy. *Curr. Opin. Environ. Sustain.* **2021**, *50*, 281–288. https://doi.org/10.1016/j.cosust.2021.06.008.

(14) Record thunderstorm losses and deadly earthquakes: the natural disasters of 2023 | Munich Re https://www.munichre.com/en/company/media-relations/media-information-and-corporate-news/media-information/2024/natural-disaster-figures-2023.html (accessed Apr 25, 2024).

(15) Hao, J.; Zhu, H.; Zhuang, Z.; Zhao, Q.; Yu, R.; Hao, J.; Kang, Q.; Lu, S.; Wang, X.; Wu, J.; Wang, D.; Du, M. Competitive Trapping of Single Atoms onto a Metal Carbide Surface. *ACS Nano* **2023**. https://doi.org/10.1021/ACSNANO.3C00866.

(16) Shih, A. J.; Monteiro, M. C. O.; Dattila, F.; Pavesi, D.; Philips, M.; da Silva, A. H. M.; Vos, R. E.; Ojha, K.; Park, S.; van der Heijden, O.; Marcandalli, G.; Goyal, A.; Villalba, M.; Chen, X.; Gunasooriya, G. T. K. K.; McCrum, I.; Mom, R.; López, N.; Koper, M. T. M. Water Electrolysis. *Nat. Rev. Methods Prim. 2022 21* **2022**, *2* (1), 1–19. https://doi.org/10.1038/s43586-022-00164-0.

(17) She, Z. W.; Kibsgaard, J.; Dickens, C. F.; Chorkendorff, I.; Nørskov, J. K.; Jaramillo, T. F. Combining Theory and Experiment in Electrocatalysis: Insights into Materials Design. *Science* **2017**, *355* (6321). https://doi.org/10.1126/SCIENCE.AAD4998.

(18) Lesson 8: Electrolysis and Electrolytic Cells - Grade12UChemistry https://grade12uchemistry.weebly.com/lesson-8-electrolysis-and-electrolytic-cells.html (accessed Apr 25, 2024).

(19) Atkins, P.; De Paula, J.; Keeler, J. *Atkins' Physical Chemistry*, 12th Editi.; Oxford University Press: Oxford, 2022.

(20) Suen, N. T.; Hung, S. F.; Quan, Q.; Zhang, N.; Xu, Y. J.; Chen, H. M. Electrocatalysis for the Oxygen Evolution Reaction: Recent Development and Future Perspectives. *Chem. Soc. Rev.* **2017**, *46* (2), 337–365. https://doi.org/10.1039/C6CS00328A.

(21) Vazhayil, A.; Vazhayal, L.; Thomas, J.; Ashok C, S.; Thomas, N. A Comprehensive Review on the Recent Developments in Transition Metal-Based Electrocatalysts for Oxygen Evolution Reaction. *Appl. Surf. Sci. Adv.* **2021**, *6*, 100184. https://doi.org/10.1016/j.apsadv.2021.100184.

(22) Chatenet, M.; Pollet, B. G.; Dekel, D. R.; Dionigi, F.; Deseure, J.; Millet, P.; Braatz, R. D.; Bazant, M. Z.; Eikerling, M.; Staffell, I.; Balcombe, P.; Shao-Horn, Y.; Schäfer, H. Water Electrolysis: From Textbook Knowledge to the Latest Scientific Strategies and Industrial Developments. *Chem. Soc. Rev.* **2022**, *51* (11), 4583–4762. https://doi.org/10.1039/d0cs01079k.

(23) Fabbri, E.; Habereder, A.; Waltar, K.; Kötz, R.; Schmidt, T. J. Developments and Perspectives of Oxide-Based Catalysts for the Oxygen Evolution Reaction. *Catal. Sci. Technol.* **2014**, *4* (11), 3800–3821. https://doi.org/10.1039/C4CY00669K.

(24) Fabbri, E.; Schmidt, T. J. Oxygen Evolution Reaction - The Enigma in Water Electrolysis. *ACS Catal.* **2018**, *8* (10), 9765–9774. https://doi.org/10.1021/acscatal.8b02712.

(25) Dau, H.; Limberg, C.; Reier, T.; Risch, M.; Roggan, S.; Strasser, P. The Mechanism of Water Oxidation: From Electrolysis via Homogeneous to Biological Catalysis. *ChemCatChem* **2010**, *2* (7), 724–761. https://doi.org/10.1002/CCTC.201000126.

(26) Plevová, M.; Hnát, J.; Bouzek, K. Electrocatalysts for the Oxygen Evolution Reaction in Alkaline and Neutral Media. A Comparative Review. *J. Power Sources* **2021**, *507*, 230072. https://doi.org/10.1016/J.JPOWSOUR.2021.230072.

(27) Skúlason, E.; Tripkovic, V.; Björketun, M. E.; Gudmundsdóttir, S.; Karlberg, G.; Rossmeisl, J.; Bligaard, T.; Jónsson, H.; Nørskov, J. K. Modeling the Electrochemical Hydrogen Oxidation and Evolution Reactions on the Basis of Density Functional Theory Calculations. *J. Phys. Chem. C* **2010**, *114* (42), 18182–18197. https://doi.org/10.1021/JP1048887.

(28) Rossmeisl, J.; Skúlason, E.; Björketun, M. E.; Tripkovic, V.; Nørskov, J. K. Modeling the Electrified Solid–Liquid Interface. *Chem. Phys. Lett.* **2008**, *466* (1–3), 68–71. https://doi.org/10.1016/j.cplett.2008.10.024.

(29) Calle-Vallejo, F.; Martínez, J. I.; García-Lastra, J. M.; Rossmeisl, J.; Koper, M. T. M. Physical and Chemical Nature of the Scaling Relations between Adsorption Energies of Atoms on Metal Surfaces. *Phys. Rev. Lett.* **2012**, *108* (11). https://doi.org/10.1103/PHYSREVLETT.108.116103.

(30) Skúlason, E.; Karlberg, G. S.; Rossmeisl, J.; Bligaard, T.; Greeley, J.; Jónsson, H.; Nørskov, J. K. Density Functional Theory Calculations for the Hydrogen Evolution Reaction in an Electrochemical Double Layer on the Pt(111) Electrode. *Phys. Chem. Chem. Phys.* **2007**, *9* (25), 3241–3250. https://doi.org/10.1039/B700099E.

(31) Garcés-Pineda, F. A.; Blasco-Ahicart, M.; Nieto-Castro, D.; López, N.; Galán-Mascarós, J. R. Direct Magnetic Enhancement of Electrocatalytic Water Oxidation in Alkaline Media. *Nat. Energy 2019 46* **2019**, *4* (6), 519–525. https://doi.org/10.1038/s41560-019-0404-4.

(32) Tayyebi, E.; Höskuldsson, Á. B.; Wark, A.; Atrak, N.; Comer, B. M.; Medford, A. J.; Skúlason, E. Perspectives on the Competition between the Electrochemical Water and N_2Oxidation on a TiO_2(110) Electrode. *J. Phys. Chem. Lett.* **2022**, *13* (26), 6123–6129. https://doi.org/10.1021/ACS.JPCLETT.2C00769.

(33) Pérez-Ramírez, J.; López, N. Strategies to Break Linear Scaling Relationships. *Nat. Catal. 2019 211* **2019**, *2* (11), 971–976. https://doi.org/10.1038/s41929-019-0376-6.

(34) Li, L.; Wang, P.; Shao, Q.; Huang, X. Recent Progress in Advanced Electrocatalyst Design for Acidic Oxygen Evolution Reaction. *Adv. Mater.* **2021**, *33* (50), 1–24. https://doi.org/10.1002/adma.202004243.

(35) Escalera-López, D.; Czioska, S.; Geppert, J.; Boubnov, A.; Röse, P.; Saraçi, E.; Krewer, U.; Grunwaldt, J. D.; Cherevko, S. Phase- And Surface Composition-Dependent Electrochemical Stability of Ir-Ru Nanoparticles during Oxygen Evolution Reaction. *ACS Catal.* **2021**, *11* (15), 9300–9316. https://doi.org/10.1021/ACSCATAL.1C01682.

(36) Elgrishi, N.; Rountree, K. J.; McCarthy, B. D.; Rountree, E. S.; Eisenhart, T. T.; Dempsey, J. L. A Practical Beginner's Guide to Cyclic Voltammetry. *J. Chem. Educ.* **2018**, *95* (2), 197–206. https://doi.org/10.1021/acs.jchemed.7b00361.

(37) Linear sweep voltammetry - Wikipedia https://en.wikipedia.org/wiki/Linear_sweep_voltammetry (accessed Apr 25, 2024).

(38) Schmidt, T. O.; Wark, A.; Haid, R. W.; Kluge, R. M.; Suzuki, S.; Kamiya, K.; Bandarenka, A. S.; Maruyama, J.; Skúlason, E. Elucidating the Active Sites and Synergies in Water Splitting on Manganese Oxide Nanosheets on Graphite Support. *Adv. Energy Mater.* **2023**, *13* (43). https://doi.org/10.1002/aenm.202302039.

(39) Binning, G.; Rohrer, H.; Gerber, C.; Weibel, E. Surface Studies by Scanning Tunneling Microscopy. *Phys. Rev. Lett.* **1982**, *49* (1), 57–61. https://doi.org/10.1103/PhysRevLett.49.57.

(40) Voigtländer, B. Scanning Probe Microscopy: Atomic Force Microscopy and Scanning Tunneling Microscopy. *Nanosci. Technol.* **2015**, 375.

(41) Huda, M. N. Epitaxial Growth of Lateral Graphene / Hexagonal Boron Nitride Heterostructures, 2016.

(42) Binning, G.; Rohrer, H.; Gerber, C.; Weibel, E. Surface Studies by Scanning Tunneling Microscopy. *Phys. Rev. Lett.* **1982**, *49* (1), 57–61. https://doi.org/10.1103/PHYSREVLETT.49.57.

(43) Lunardon, M.; Kosmala, T.; Durante, C.; Agnoli, S.; Granozzi, G. Atom-by-Atom Identification of Catalytic Active Sites in Operando Conditions by Quantitative Noise Detection. *Joule* **2022**, *6* (3), 617–635. https://doi.org/10.1016/J.JOULE.2022.02.010.

(44) Zheng, W.; Lee, L. Y. S. Observing Electrocatalytic Processes via In Situ Electrochemical Scanning Tunneling Microscopy: Latest Advances. *Chem. - An Asian J.* **2022**, *17* (15). https://doi.org/10.1002/ASIA.202200384.

(45) Pfisterer, J. H. K.; Liang, Y.; Schneider, O.; Bandarenka, A. S. Direct Instrumental Identification of Catalytically Active Surface Sites. *Nature* **2017**, *549* (7670), 74–77. https://doi.org/10.1038/nature23661.

(46) Haid, R. W.; Kluge, R. M.; Schmidt, T. O.; Bandarenka, A. S. In-Situ Detection of Active Sites for Carbon-Based Bifunctional Oxygen Reduction and Evolution Catalysis. *Electrochim. Acta* **2021**, *382*. https://doi.org/10.1016/J.ELECTACTA.2021.138285.

(47) Schmidt, T. O.; Wark, A.; Haid, R. W.; Kluge, R. M.; Suzuki, S.; Kamiya, K.; Bandarenka, A. S.; Maruyama, J.; Skúlason, E. Elucidating the Active Sites and Synergies in Water Splitting on Manganese Oxide Nanosheets on Graphite Support. *Adv. Energy Mater.* **2023**, *13* (43), 2302039. https://doi.org/10.1002/AENM.202302039.

(48) Liang, Y.; McLaughlin, D.; Csoklich, C.; Schneider, O.; Bandarenka, A. S. The Nature of Active Centers Catalyzing Oxygen Electro-Reduction at Platinum Surfaces in Alkaline Media. *Energy Environ. Sci.* **2019**, *12* (1), 351–357. https://doi.org/10.1039/c8ee03228a.

(49) Calle-Vallejo, F.; Pohl, M. D.; Reinisch, D.; Loffreda, D.; Sautet, P.; Bandarenka, A. S. Why Conclusions from Platinum Model Surfaces Do Not Necessarily Lead to Enhanced Nanoparticle Catalysts for the Oxygen Reduction Reaction. *Chem. Sci.* **2017**, *8* (3), 2283–2289. https://doi.org/10.1039/C6SC04788B.

(50) Haid, R. W.; Kluge, R. M.; Schmidt, T. O.; Bandarenka, A. S. In-Situ Detection of Active Sites for Carbon-Based Bifunctional Oxygen Reduction and Evolution Catalysis. *Electrochim. Acta* **2021**, *382*, 138285. https://doi.org/10.1016/J.ELECTACTA.2021.138285.

(51) Schmidt, T. O.; Ngoipala, A.; Arevalo, R. L.; Watzele, S. A.; Lipin, R.; Kluge, R. M.; Hou, S.; Haid, R. W.; Senyshyn, A.; Gubanova, E. L.; Bandarenka, A. S.; Vandichel, M. Elucidation of Structure–Activity Relations in Proton Electroreduction at Pd Surfaces: Theoretical and Experimental Study. *Small* **2022**, *18* (30), 2202410. https://doi.org/10.1002/smll.202202410.

(52) Guidelli, R.; Compton, R. G.; Feliu, J. M.; Gileadi, E.; Lipkowski, J.; Schmickler, W.; Trasatti, S. Definition of the Transfer Coefficient in Electrochemistry (IUPAC Recommendations 2014). *Pure Appl. Chem.* **2014**, *86* (2), 259–262. https://doi.org/10.1515/pac-2014-5025.

(53) Bockris, J. O.; Reddy, A. K. N. Modern Electrochemistry. *Mod. Electrochem.* **1970**. https://doi.org/10.1007/978-1-4615-8600-5.

(54) Man, I. C.; Su, H. Y.; Calle-Vallejo, F.; Hansen, H. A.; Martínez, J. I.; Inoglu, N. G.; Kitchin, J.; Jaramillo, T. F.; Nørskov, J. K.; Rossmeisl, J. Universality in Oxygen Evolution Electrocatalysis on Oxide Surfaces. *ChemCatChem* **2011**, *3* (7), 1159–1165. https://doi.org/10.1002/cctc.201000397.

(55) Govindarajan, N.; García-Lastra, J. M.; Meijer, E. J.; Calle-Vallejo, F. Does the Breaking of Adsorption-Energy Scaling Relations Guarantee Enhanced Electrocatalysis? *Curr. Opin. Electrochem.* **2018**, *8*, 110–117. https://doi.org/10.1016/J.COELEC.2018.03.025.

(56) Exner, K. S. Recent Progress in the Development of Screening Methods to Identify Electrode Materials for the Oxygen Evolution Reaction. *Adv. Funct. Mater.* **2020**, *30* (42). https://doi.org/10.1002/ADFM.202005060.

(57) Exner, K. S. A Universal Descriptor for the Screening of Electrode Materials for Multiple-Electron Processes: Beyond the Thermodynamic Overpotential. *ACS Catal.* **2020**, *10* (21), 12607–12617. https://doi.org/10.1021/ACSCATAL.0C03865.

(58) Craig, M. J.; Coulter, G.; Dolan, E.; Soriano-López, J.; Mates-Torres, E.; Schmitt, W.; García-Melchor, M. Universal Scaling Relations for the Rational Design of Molecular Water Oxidation Catalysts with Near-Zero Overpotential. *Nat. Commun.* **2019**, *10* (1). https://doi.org/10.1038/S41467-019-12994-W.

(59) Li, X.; Cheng, Z.; Wang, X. Understanding the Mechanism of the Oxygen Evolution Reaction with Consideration of Spin. *Electrochem. Energy Rev.* **2021**, *4* (1), 136–145. https://doi.org/10.1007/S41918-020-00084-1.

(60) Craig, M. J.; García-Melchor, M. Reaction Descriptors for the Oxygen Evolution Reaction: Recent Advances, Challenges, and Opportunities. *Curr. Opin. Electrochem.* **2022**, *35*, 101044. https://doi.org/10.1016/J.COELEC.2022.101044.

(61) Dickens, C. F.; Kirk, C.; Nørskov, J. K. Insights into the Electrochemical Oxygen Evolution Reaction with Ab Initio Calculations and Microkinetic Modeling: Beyond the Limiting Potential Volcano. *J. Phys. Chem. C* **2019**, *123* (31), 18960–18977. https://doi.org/10.1021/ACS.JPCC.9B03830.

(62) Huang, X.; Wang, J.; Tao, H. B.; Tian, H.; Xu, H. An Essential Descriptor for the Oxygen Evolution Reaction on Reducible Metal Oxide Surfaces. *Chem. Sci.* **2019**, *10* (11), 3340–3345. https://doi.org/10.1039/C8SC04521F.

(63) Roy, C.; Sebok, B.; Scott, S. B.; Fiordaliso, E. M.; Sørensen, J. E.; Bodin, A.; Trimarco, D. B.; Damsgaard, C. D.; Vesborg, P. C. K.; Hansen, O.; Stephens, I. E. L.; Kibsgaard, J.; Chorkendorff, I. Impact of Nanoparticle Size and Lattice Oxygen on Water Oxidation on $NiFeO_xH_y$. *Nat. Catal.* **2018**, *1* (11), 820–829. https://doi.org/10.1038/S41929-018-0162-X.

(64) Scott, S. B.; Rao, R. R.; Moon, C.; Sørensen, J. E.; Kibsgaard, J.; Shao-Horn, Y.; Chorkendorff, I. The Low Overpotential Regime of Acidic Water Oxidation Part I: The Importance of O_2 Detection. *Energy Environ. Sci.* **2022**. https://doi.org/10.1039/D1EE03914H.

(65) Scott, S. B.; Sørensen, J. E.; Rao, R. R.; Moon, C.; Kibsgaard, J.; Shao-Horn, Y.; Chorkendorff, I. The Low Overpotential Regime of Acidic Water Oxidation Part II: Trends in Metal and Oxygen Stability Numbers. *Energy Environ. Sci.* **2022**. https://doi.org/10.1039/D1EE03915F.

(66) Zheng, Y. R.; Vernieres, J.; Wang, Z.; Zhang, K.; Hochfilzer, D.; Krempl, K.; Liao, T. W.; Presel, F.; Altantzis, T.; Fatermans, J.; Scott, S. B.; Secher, N. M.; Moon, C.; Liu, P.; Bals, S.; Van Aert, S.; Cao, A.; Anand, M.; Nørskov, J. K.; Kibsgaard, J.; Chorkendorff, I. Monitoring Oxygen Production on Mass-Selected Iridium–Tantalum Oxide Electrocatalysts. *Nat. Energy* **2022**, *7* (1), 55–64. https://doi.org/10.1038/S41560-021-00948-W.

(67) Kibsgaard, J.; Chorkendorff, I. Considerations for the Scaling-up of Water Splitting Catalysts. *Nat. Energy* **2019**, *4* (6), 430–433. https://doi.org/10.1038/S41560-019-0407-1.

(68) Dionigi, F.; Zeng, Z.; Sinev, I.; Merzdorf, T.; Deshpande, S.; Lopez, M. B.; Kunze, S.; Zegkinoglou, I.; Sarodnik, H.; Fan, D.; Bergmann, A.; Drnec, J.; Araujo, J. F. de; Gliech, M.; Teschner, D.; Zhu, J.; Li, W. X.; Greeley, J.; Roldan Cuenya, B.; Strasser, P. In-Situ Structure and Catalytic Mechanism of NiFe and CoFe Layered Double Hydroxides during Oxygen Evolution. *Nat. Commun.* **2020**, *11* (1). https://doi.org/10.1038/S41467-020-16237-1.

(69) Zhou, Y.; López, N. The Role of Fe Species on NiOOH in Oxygen Evolution Reactions. *ACS Catal.* **2020**, *10* (11), 6254–6261. https://doi.org/10.1021/ACSCATAL.0C00304/ASSET/IMAGES/LARGE/CS0C00304_0004.JPEG.

(70) Chung, D. Y.; Lopes, P. P.; Farinazzo Bergamo Dias Martins, P.; He, H.; Kawaguchi, T.; Zapol, P.; You, H.; Tripkovic, D.; Strmcnik, D.; Zhu, Y.; Seifert, S.; Lee, S.; Stamenkovic, V. R.; Markovic, N. M. Dynamic Stability of Active Sites in Hydr(Oxy)Oxides for the Oxygen Evolution Reaction. *Nat. Energy* **2020**, *5* (3), 222–230. https://doi.org/10.1038/s41560-020-0576-y.

(71) Tian, L.; Zhai, X.; Wang, X.; Li, J.; Li, Z. Advances in Manganese-Based Oxides for Oxygen Evolution Reaction. *J. Mater. Chem. A* **2020**, *8* (29), 14400–14414. https://doi.org/10.1039/d0ta05116k.

(72) Umena, Y.; Kawakami, K.; Shen, J. R.; Kamiya, N. Crystal Structure of Oxygen-Evolving Photosystem II at a Resolution of 1.9Å. *Nature* **2011**, *473* (7345), 55–60. https://doi.org/10.1038/NATURE09913.

(73) Liu, B.; Sun, Y.; Liu, L.; Xu, S.; Yan, X. Advances in Manganese-Based Oxides Cathodic Electrocatalysts for Li–Air Batteries. *Adv. Funct. Mater.* **2018**, *28* (15), 1–34. https://doi.org/10.1002/adfm.201704973.

(74) Chernev, P.; Fischer, S.; Hoffmann, J.; Oliver, N.; Assunção, R.; Yu, B.; Burnap, R. L.; Zaharieva, I.; Nürnberg, D. J.; Haumann, M.; Dau, H. Light-Driven Formation of Manganese Oxide by Today's Photosystem II Supports Evolutionarily Ancient Manganese-Oxidizing Photosynthesis. *Nat. Commun.* **2020**, *11* (1). https://doi.org/10.1038/S41467-020-19852-0.

(75) Mirzakulova, E.; Khatmullin, R.; Walpita, J.; Corrigan, T.; Vargas-Barbosa, N. M.; Vyas, S.; Oottikkal, S.; Manzer, S. F.; Hadad, C. M.; Glusac, K. D. Electrode-Assisted Catalytic Water Oxidation by a Flavin Derivative. *Nat. Chem. 2012 410* **2012**, *4* (10), 794–801. https://doi.org/10.1038/nchem.1439.

(76) Kaiser, S. K.; Chen, Z.; Faust Akl, D.; Mitchell, S.; Pérez-Ramírez, J. Single-Atom Catalysts across the Periodic Table. *Chem. Rev.* **2020**, *120* (21), 11703–11809. https://doi.org/10.1021/acs.chemrev.0c00576.

(77) Fischer, P. J.; Kühn, F. E. „Brot Aus Luft" Und Andere Chemische Beiträge Zur Welternährung. *Chemie unserer Zeit* **2019**, *53* (2), 112–124. https://doi.org/10.1002/CIUZ.201800848.

(78) Guderian, R. Aquatische Systeme, Volume 1. **2000**, 474.

(79) Medford, A. J.; Hatzell, M. C. Photon-Driven Nitrogen Fixation: Current Progress, Thermodynamic Considerations, and Future Outlook. *ACS Catal.* **2017**, *7* (4), 2624–2643. https://doi.org/10.1021/acscatal.7b00439.

(80) Nitrogen Cycle - Reactions and Enzymes - Nitrogen cycle - Wikipedia https://en.wikipedia.org/wiki/Nitrogen_cycle#/media/File:Nitrogen_Cycle_-_Reactions_and_Enzymes.svg (accessed Apr 26, 2024).

(81) Smil, V. How Many People Can the Earth Feed? *Popul. Dev. Rev.* **1994**, *20* (2), 255–292. https://doi.org/10.2307/2137520.

(82) Tayyebi, E.; Abghoui, Y.; Skúlason, E. Elucidating the Mechanism of Electrochemical N2 Reduction at the Ru(0001) Electrode. *ACS Catal.* **2019**, *9* (12), 11137–11145. https://doi.org/10.1021/ACSCATAL.9B03903.

(83) Skúlason, E.; Bligaard, T.; Gudmundsdóttir, S.; Studt, F.; Rossmeisl, J.; Abild-Pedersen, F.; Vegge, T.; Jónsson, H.; Nørskov, J. K. A Theoretical Evaluation of Possible Transition Metal Electro-Catalysts for N2 Reduction. *Phys. Chem. Chem. Phys.* **2012**, *14* (3), 1235–1245. https://doi.org/10.1039/C1CP22271F.

(84) Hanifpour, F.; Sveinbjörnsson, A.; Canales, C. P.; Skúlason, E.; Flosadóttir, H. D. Preparation of Nafion Membranes for Reproducible Ammonia Quantification in Nitrogen Reduction Reaction Experiments. *Angew. Chemie* **2020**, *132* (51), 23138–23142. https://doi.org/10.1002/ANGE.202007998.

(85) Zhang, K.; Cao, A.; Wandall, L. H.; Vernieres, J.; Kibsgaard, J.; Nørskov, J. K.; Chorkendorff, I. Spin-Mediated Promotion of Co Catalysts for Ammonia Synthesis. *Science* **2024**, *383* (6689), 1357–1363. https://doi.org/10.1126/SCIENCE.ADN0558.

(86) Andersen, S. Z.; Čolić, V.; Yang, S.; Schwalbe, J. A.; Nielander, A. C.; McEnaney, J. M.; Enemark-Rasmussen, K.; Baker, J. G.; Singh, A. R.; Rohr, B. A.; Statt, M. J.; Blair, S. J.; Mezzavilla, S.; Kibsgaard, J.; Vesborg, P. C. K.; Cargnello, M.; Bent, S. F.; Jaramillo, T. F.; Stephens, I. E. L.; Nørskov, J. K.; Chorkendorff, I. A Rigorous Electrochemical Ammonia Synthesis Protocol with Quantitative Isotope Measurements. *Nature* **2019**, *570* (7762), 504–508. https://doi.org/10.1038/S41586-019-1260-X.

(87) Deissler, N. H.; Mygind, J. B. V. V.; Li, K.; Niemann, V.; Benedek, P.; Vinci, V.; Li, S.; Fu, X.; Vesborg, P. C. K.; Jaramillo, T.; Kibsgaard, J.; Drnec, J.; Chorkendorff, I. Operando Investigations of the Solid Electrolyte Interphase in the Lithium Mediated Nitrogen Reduction Reaction. *Energy Environ. Sci.* **2024**. https://doi.org/10.1039/D3EE04235A.

(88) Fu, X.; Niemann, V. A.; Zhou, Y.; Li, S.; Zhang, K.; Pedersen, J. B.; Saccoccio, M.; Andersen, S. Z.; Enemark-Rasmussen, K.; Benedek, P.; Xu, A.; Deissler, N. H.; Mygind, J. B. V.; Nielander, A. C.; Kibsgaard, J.; Vesborg, P. C. K.; Nørskov, J. K.; Jaramillo, T. F.; Chorkendorff, I. Calcium-Mediated Nitrogen Reduction for Electrochemical Ammonia Synthesis. *Nat. Mater. 2023 231* **2023**, *23* (1), 101–107. https://doi.org/10.1038/s41563-023-01702-1.

(89) Steiner, R.; Maurer, C. *Comparative Carbon Footprint of Traditional and Novel Nitrogen Fertilizer Production Methods*; 2017.

(90) Tuck, A. F. Production of Nitrogen Oxides by Lightning Discharges. *Q. J. R. Meteorol. Soc.* **1976**, *102* (434), 749–755. https://doi.org/10.1002/QJ.49710243404.

(91) Birkeland, K. R. On the Oxidation of Atmospheric Nitrogen in Electric Arcs. *Trans. Faraday Soc.* **1906**, *2* (December), 98–116. https://doi.org/10.1039/TF9060200098.

(92) Williams, T. I.; Derry, T. K. (Thomas K. A Short History of Twentieth-Century Technology c. 1900-c. 1950. **1982**, 411.

(93) Li, T.; Han, S.; Cheng, C.; Wang, Y.; Du, X.; Yu, Y.; Zhang, B. Sulfate-Enabled Nitrate Synthesis from Nitrogen Electrooxidation on a Rhodium Electrocatalyst. *Angew. Chemie Int. Ed.* **2022**, *61* (26), e202204541. https://doi.org/10.1002/ANIE.202204541.

(94) Wang, Z.; Liu, J.; Zhao, H.; Xu, W.; Liu, J.; Liu, Z.; Lai, J.; Wang, L. Free Radicals Promote Electrocatalytic Nitrogen Oxidation. *Chem. Sci.* **2023**, *14* (7), 1878–1884. https://doi.org/10.1039/d2sc06599a.

(95) Li, T.; Han, S.; Wang, C.; Huang, Y.; Wang, Y.; Yu, Y.; Zhang, B. Ru-Doped Pd Nanoparticles for Nitrogen Electrooxidation to Nitrate. *ACS Catal.* **2021**, *11* (22), 14032–14037. https://doi.org/10.1021/ACSCATAL.1C04360/ASSET/IMAGES/LARGE/CS1C04360_0004.JPEG.

(96) Guo, Y.; Zhang, S.; Zhang, R.; Wang, D.; Zhu, D.; Wang, X.; Xiao, D.; Li, N.; Zhao, Y.; Huang, Z.; Xu, W.; Chen, S.; Song, L.; Fan, J.; Chen, Q.; Zhi, C. Electrochemical Nitrate Production via Nitrogen Oxidation with Atomically Dispersed Fe on N-Doped Carbon Nanosheets. *ACS Nano* **2022**, *16* (1), 655–663. https://doi.org/10.1021/acsnano.1c08109.

(97) Zhang, L.; Cong, M.; Ding, X.; Jin, Y.; Xu, F.; Wang, Y.; Chen, L.; Zhang, L. A Janus Fe-SnO_2 Catalyst That Enables Bifunctional Electrochemical Nitrogen Fixation. *Angew. Chemie - Int. Ed.* **2020**, *59* (27), 10888–10893. https://doi.org/10.1002/ANIE.202003518.

(98) Wang, Y.; Li, T.; Yu, Y.; Zhang, B. Electrochemical Synthesis of Nitric Acid from Nitrogen Oxidation. *Angew. Chemie - Int. Ed.* **2022**, *61* (12). https://doi.org/10.1002/ANIE.202115409.

(99) Dai, C.; Sun, Y.; Chen, G.; Fisher, A. C.; Xu, Z. J. Electrochemical Oxidation of Nitrogen towards Direct Nitrate Production on Spinel Oxides. *Angew. Chemie - Int. Ed.* **2020**, *59* (24), 9418–9422. https://doi.org/10.1002/ANIE.202002923.

(100) Anand, M.; Abraham, C. S.; Nørskov, J. K. Electrochemical Oxidation of Molecular Nitrogen to Nitric Acid-towards a Molecular Level Understanding of the Challenges. *Chem. Sci.* **2021**, *12* (18), 6442–6448. https://doi.org/10.1039/D1SC00752A.

(101) Wan, H.; Bagger, A.; Rossmeisl, J. Limitations of Electrochemical Nitrogen Oxidation toward Nitrate. *J. Phys. Chem. Lett.* **2022**, *13* (38), 8928–8934. https://doi.org/10.1021/ACS.JPCLETT.2C02459.

(102) Long, J.; Luan, D.; Fu, X.; Li, H.; Jing, H.; Xiao, J. Fundamental Insights on the Electrochemical Nitrogen Oxidation over Metal Oxides. *ACS Catal.* **2024**, *14*, 4423–4431. https://doi.org/10.1021/ACSCATAL.3C05307/ASSET/IMAGES/LARGE/CS3C05307_0006.JPEG.

(103) Kuang, M.; Wang, Y.; Fang, W.; Tan, H.; Chen, M.; Yao, J.; Liu, C.; Xu, J.; Zhou, K.; Yan, Q. Efficient Nitrate Synthesis via Ambient Nitrogen Oxidation with Ru-Doped TiO_2 /RuO_2 Electrocatalysts. *Adv. Mater.* **2020**, *32* (26), 2002189. https://doi.org/10.1002/adma.202002189.

(104) Schrödinger, E. An Undulatory Theory of the Mechanics of Atoms and Molecules. *Phys. Rev.* **1926**, *28* (6), 1049. https://doi.org/10.1103/PhysRev.28.1049.

(105) Griffiths, D. J.; Schroeter, D. F. *Introduction to Quantum Mechanics*, 3rd ed.; Cambridge University Press: Cambridge, 2018. https://doi.org/DOI: 10.1017/9781316995433.

(106) Born, M.; Oppenheimer, R. Zur Quantentheorie Der Molekeln. *Ann. Phys.* **1927**, *389* (20), 457–484. https://doi.org/10.1002/andp.19273892002.

(107) Slater, J. C. The Theory of Complex Spectra. *Phys. Rev.* **1929**, *34* (10), 1293. https://doi.org/10.1103/PhysRev.34.1293.

(108) Hartree, D. R. The Wave Mechanics of an Atom with a Non-Coulomb Central Field. Part I. Theory and Methods. *Math. Proc. Cambridge Philos. Soc.* **1928**, *24* (1), 89–110. https://doi.org/DOI: 10.1017/S0305004100011919.

(109) Fock, V. Näherungsmethode Zur Lösung Des Quantenmechanischen Mehrkörperproblems. *Zeitschrift für Phys.* **1930**, *61* (1–2), 126–148. https://doi.org/10.1007/BF01340294/METRICS.

(110) Hohenberg, P.; Kohn, W. Inhomogeneous Electron Gas. *Phys. Rev.* **1964**, *136* (3B). https://doi.org/10.1103/PHYSREV.136.B864.

(111) Kohn, W.; Sham, L. J. Self-Consistent Equations Including Exchange and Correlation Effects. *Phys. Rev.* **1965**, *140* (4A). https://doi.org/10.1103/PHYSREV.140.A1133.

(112) Hohenberg, P.; Kohn, W. Inhomogeneous Electron Gas. *Phys. Rev.* **1964**, *136* (3B), B864. https://doi.org/10.1103/PHYSREV.136.B864/FIGURE/1/THUMB.

(113) Vosko, S. H.; Wilk, L. Influence of an Improved Local-Spin-Density Correlation-Energy Functional on the Cohesive Energy of Alkali Metals. *Phys. Rev. B* **1980**, *22* (8), 3812. https://doi.org/10.1103/PhysRevB.22.3812.

(114) Perdew, J. P.; Burke, K.; Ernzerhof, M. Generalized Gradient Approximation Made Simple. *Phys. Rev. Lett.* **1996**, *77* (18), 3865–3868. https://doi.org/10.1103/PHYSREVLETT.77.3865.

(115) Perdew, J. P.; Burke, K.; Ernzerhof, M. Erratum: Generalized Gradient Approximation Made Simple (Physical Review Letters (1996) 77 (3865)). *Phys. Rev. Lett.* **1997**, *78* (8), 1396. https://doi.org/10.1103/PHYSREVLETT.78.1396.

(116) Sun, J.; Ruzsinszky, A.; Perdew, J. Strongly Constrained and Appropriately Normed Semilocal Density Functional. *Phys. Rev. Lett.* **2015**, *115* (3). https://doi.org/10.1103/PHYSREVLETT.115.036402.

(117) Paier, J.; Marsman, M.; Hummer, K.; Kresse, G.; Gerber, I. C.; Angyán, J. G. Screened Hybrid Density Functionals Applied to Solids. *J. Chem. Phys.* **2006**, *124* (15). https://doi.org/10.1063/1.2187006.

(118) Lechner, C.; Pannier, B.; Baranek, P.; Forero-Martinez, N. C.; Vach, H. First-Principles Study of the Structural, Electronic, Dynamic, and Mechanical Properties of HOPG and Diamond: Influence of Exchange-Correlation Functionals and Dispersion Interactions. *J. Phys. Chem. C* **2016**, *120* (9), 5083–5100. https://doi.org/10.1021/ACS.JPCC.5B10396/ASSET/IMAGES/LARGE/JP-2015-10396X_0011.JPEG.

(119) Marom, N.; Tkatchenko, A.; Rossi, M.; Gobre, V. V.; Hod, O.; Scheffler, M.; Kronik, L. Dispersion Interactions with Density-Functional Theory: Benchmarking Semiempirical and Interatomic Pairwise Corrected Density Functionals. *J. Chem. Theory Comput.* **2011**, *7* (12), 3944–3951. https://doi.org/10.1021/CT2005616.

(120) Grimme, S.; Antony, J.; Ehrlich, S.; Krieg, H. A Consistent and Accurate Ab Initio Parametrization of Density Functional Dispersion Correction (DFT-D) for the 94 Elements H-Pu. *J. Chem. Phys.* **2010**, *132* (15). https://doi.org/10.1063/1.3382344/926936/A-CONSISTENT-AND-ACCURATE-AB-INITIO.

(121) Grimme, S. Semiempirical GGA-Type Density Functional Constructed with a Long-Range Dispersion Correction. *J. Comput. Chem.* **2006**, *27* (15), 1787–1799. https://doi.org/10.1002/JCC.20495.

(122) Tkatchenko, A.; DiStasio, R. A.; Car, R.; Scheffler, M. Accurate and Efficient Method for Many-Body van Der Waals Interactions. *Phys. Rev. Lett.* **2012**, *108* (23), 236402. https://doi.org/10.1103/PhysRevLett.108.236402.

(123) Tkatchenko, A.; Scheffler, M. Accurate Molecular van Der Waals Interactions from Ground-State Electron Density and Free-Atom Reference Data. *Phys. Rev. Lett.* **2009**, *102* (7). https://doi.org/10.1103/PHYSREVLETT.102.073005.

(124) Perdew, J. P. Density Functional Theory and the Band Gap Problem. *Int. J. Quantum Chem.* **1985**, *28* (19 S), 497–523. https://doi.org/10.1002/QUA.560280846.

(125) Cohen, A. J.; Mori-Sánchez, P.; Yang, W. Insights into Current Limitations of Density Functional Theory. *Science (80-.).* **2008**, *321* (5890), 792–794. https://doi.org/10.1126/SCIENCE.1158722.

(126) Perdew, J. P.; Zunger, A. Self-Interaction Correction to Density-Functional Approximations for Many-Electron Systems. *Phys. Rev. B* **1981**, *23* (10), 5048. https://doi.org/10.1103/PhysRevB.23.5048.

(127) Dudarev, S. L.; Botton, G. A.; Savrasov, S. Y.; Humphreys, C. J.; Sutton, A. P. Electron-Energy-Loss Spectra and the Structural Stability of Nickel Oxide: An LSDA+U Study. *Phys. Rev. B* **1998**, *57* (3), 1505. https://doi.org/10.1103/PhysRevB.57.1505.

(128) Hubbard, J. Electron Correlations in Narrow Energy Bands. *Proc. R. Soc. London. Ser. A. Math. Phys. Sci.* **1963**, *276* (1365), 238–257. https://doi.org/10.1098/rspa.1963.0204.

(129) Anisimov, V. I.; Aryasetiawan, F.; Lichtenstein, A. I. First-Principles Calculations of the Electronic Structure and Spectra of Strongly Correlated Systems: The LDA + U Method. *J. Phys. Condens. Matter* **1997**, *9* (4), 767–808. https://doi.org/10.1088/0953-8984/9/4/002.

(130) Wellendorff, J.; Lundgaard, K. T.; Møgelhøj, A.; Petzold, V.; Landis, D. D.; Nørskov, J. K.; Bligaard, T.; Jacobsen, K. W. Density Functionals for Surface Science: Exchange-Correlation Model Development with Bayesian Error Estimation. *Phys. Rev. B - Condens. Matter Mater. Phys.* **2012**, *85* (23). https://doi.org/10.1103/PHYSREVB.85.235149.

(131) Dion, M.; Rydberg, H.; Schröder, E.; Langreth, D. C.; Lundqvist, B. I. Van Der Waals Density Functional for General Geometries. *Phys. Rev. Lett.* **2004**, *92* (24). https://doi.org/10.1103/PHYSREVLETT.92.246401.

(132) Grimme, S.; Antony, J.; Ehrlich, S.; Krieg, H. A Consistent and Accurate Ab Initio Parametrization of Density Functional Dispersion Correction (DFT-D) for the 94 Elements H-Pu. *J. Chem. Phys.* **2010**, *132* (15). https://doi.org/10.1063/1.3382344.

(133) Peng, H.; Perdew, J. P. Synergy of van Der Waals and Self-Interaction Corrections in Transition Metal Monoxides. *Phys. Rev. B* **2017**, *96* (10), 1–2. https://doi.org/10.1103/PhysRevB.96.100101.

(134) Grimme, S.; Ehrlich, S.; Goerigk, L. Effect of the Damping Function in Dispersion Corrected Density Functional Theory. *J. Comput. Chem.* **2011**, *32* (7), 1456–1465. https://doi.org/10.1002/JCC.21759.

(135) Schröder, H.; Hühnert, J.; Schwabe, T. Evaluation of DFT-D3 Dispersion Corrections for Various Structural Benchmark Sets. *J. Chem. Phys.* **2017**, *146* (4). https://doi.org/10.1063/1.4974840.

(136) Ambrosetti, A.; Reilly, A. M.; Distasio, R. A.; Tkatchenko, A. Long-Range Correlation Energy Calculated from Coupled Atomic Response Functions. *J. Chem. Phys.* **2014**, *140* (18). https://doi.org/10.1063/1.4865104.

(137) Sabatini, R.; Gorni, T.; De Gironcoli, S. Nonlocal van Der Waals Density Functional Made Simple and Efficient. *RAPID Commun. Phys. Rev. B* **2013**, *87*, 41108. https://doi.org/10.1103/PhysRevB.87.041108.

(138) Sabatini, R.; Gorni, T.; De Gironcoli, S. Nonlocal van Der Waals Density Functional Made Simple and Efficient. *Phys. Rev. B - Condens. Matter Mater. Phys.* **2013**, *87* (4). https://doi.org/10.1103/PHYSREVB.87.041108.

(139) Bloch, F. Über Die Quantenmechanik Der Elektronen in Kristallgittern. *Zeitschrift für Phys.* **1928**, *52* (7–8), 555–600. https://doi.org/10.1007/BF01339455.

(140) Jensen, F. *Introduction to Computational Chemistry*, Third edit.; John Wiley & Sons, Ltd.: Chichester West Sussex, UK SE - xxii, 638 pages ; 25 cm, 2017. https://doi.org/LK - https://worldcat.org/title/957680749.

(141) Hafner, J. Ab-Initio Simulations of Materials Using VASP: Density-Functional Theory and Beyond. *J. Comput. Chem.* **2008**, *29* (13), 2044–2078. https://doi.org/10.1002/JCC.21057.

(142) Joubert, D. From Ultrasoft Pseudopotentials to the Projector Augmented-Wave Method. *Phys. Rev. B - Condens. Matter Mater. Phys.* **1999**, *59* (3), 1758–1775. https://doi.org/10.1103/PHYSREVB.59.1758.

(143) Blöchl, P. E. Projector Augmented-Wave Method. *Phys. Rev. B* **1994**, *50* (24), 17953–17979. https://doi.org/10.1103/PHYSREVB.50.17953.

(144) Bader, R. F. W.; Essén, H. The Characterization of Atomic Interactions. *J. Chem. Phys.* **1984**, *80* (5), 1943–1960. https://doi.org/10.1063/1.446956.

(145) Nørskov, J. K.; Rossmeisl, J.; Logadottir, A.; Lindqvist, L.; Kitchin, J. R.; Bligaard, T.; Jónsson, H. Origin of the Overpotential for Oxygen Reduction at a Fuel-Cell Cathode. *J. Phys. Chem. B* **2004**, *108* (46), 17886–17892. https://doi.org/10.1021/JP047349J.

(146) Melander, M. M.; Kuisma, M. J.; Christensen, T. E. K.; Honkala, K. Grand-Canonical Approach to Density Functional Theory of Electrocatalytic Systems: Thermodynamics of Solid-Liquid Interfaces at Constant Ion and Electrode Potentials. *J. Chem. Phys.* **2019**, *150* (4), 041706. https://doi.org/10.1063/1.5047829.

(147) Darby, M. T.; Cucinotta, C. S. The Role of Water at Electrified Metal-Water Interfaces Unravelled from First Principles. *Curr. Opin. Electrochem.* **2022**, *36*. https://doi.org/10.1016/j.coelec.2022.101118.

Paper I

Paper II

Paper III